MODELLING OF THE INERTIA WELDING OF INCONEL 718

by

LIBIN YANG

A thesis submitted to
The University of Birmingham
for the degree of
DOCTOR OF PHILOSOPHY

School of Metallurgy and Materials
College of Engineering and Physical Sciences
The Univeristy of Birmingham
January 2010

Abstract

In this study, the inertia welding process was studied by both an FEM model and three analytical models. The thermal analysis shows that there is a steep temperature gradient near the mating surface, which is the cause for the existence of a band of high hydrostatic stress near the weld line. The holding effect of this high static stress is the reason for the presence of the very soft material at the welding interface. The models were used to predict the displacement of the weld line (upset) with a lambda model to describe the constitutive relation of IN718 at high temperature. The results from the different models are in broad agreement. The shear stress induced by friction at the interface is found to enlarge the upset value; its effect must be taken into account if the upset is to be predicted accurately. The extrusion of the burr during the last second of the welding is a direct result of the quick stop of the rotating part due to the balance of the momentum, which is clearly explained by the analytical mechanical model put forward in this work.

Anything good in this dissertation is purely due to the blessings from GOD who created the heaven and the earth.

Anything not good enough is due to the weakness in my flesh.

Praise and glory and wisdom and thanks and honour and power and strength be to our heavenly Father, and to Jesus Christ for ever and ever, Amen!

The fear of the LORD is the beginning of wisdom; all who follow his precepts have good understanding. -Psalms 111:10

Preface

This dissertation is submitted for the degree of Doctor of Philosophy at the University of Birmingham. The research reported herein was carried out under the supervision of Professor R.C.Reed and Professor P.Bowen at the School of Metallurgy and Materials between September 2005 and December 2009.

This dissertation is the result of my own work and includes nothing which is the outcome of work done in collaboration except where specifically indicated in the text. This work is to the best of my knowledge, original, except where acknowledgments and references are made to the previous work. Neither this, nor any substantially similar dissertation has been, or is being submitted for any degree, diploma, or other qualification at this, or any other university. The length of this thesis does not exceed 50,000 words.

Parts of this dissertation have been submitted in:

Libin Yang, J.C.Gebelin, R.C.Reed, Modelling of the inertia welding of the IN718 superalloy. *Materials Science and Technology* (accepted).

Libin Yang June 15, 2010

Acknowledgements

Thanks to God's amazing grace, I became a Christian during my PhD study in Birmingham, UK. That's the most important event during my study and my whole life, for I began to know Jesus Christ, the source of all blessings, wisdom, love, salvation.

I am very grateful to Professor P.Bowen for giving me a chance to study in the Department of Metallurgy and Materials at the University of Birmingham. I am also impressed by his kindness, patience and encouragement to me, which have benefited me a lot. His extension of my financial support for another twelve months is an unforgettable help to ease me from possible financial trouble.

I am also very grateful to Professor R.C.Reed for the beneficial guidance of the directions in this research, whose intuition left me deep impression. I also need to thank him for allowing me to have a seat in PRISM^2, where I got great convenience to use the softwares needed.

I am indebted to Dr. J.C.Gebelin, whose quick and pertinent help makes studying in PRISM^2 a happy experience.

I would also thank Friedrich Daus for the very useful discussions and his warm help. The time when we prayed together in Jesus Christ's name is among the most blessed moments during this PhD study.

I also indebted to Prof.Jeff Brooks in AFRC, University of Strathclyde for his help with the constitutive models used.

I would like to thank Jo Corbett for her always considerate help over this four year study.

The members of PRISM^2, have been a source of knowledge and friendship, namely, Dr. Nils Warnken, Jianglin Huang, Hang Wang, Tao Tao, Edvardo Trejo.

I also need to thank Professor J.Lin and Dr.Yu-Pei Lin, Dr.M.Novovic, Dr.Hangyue Li, Y. Pardhi, C.Po-Sri for their friendship and help in the early period of this research.

I also would like to thank lots of my church members in BCEC (Birmingham Chinese Evangelical Church), for example, Dr.Xiaoming Cai, Dr.Qiang li, Dr.Zhengwen Zhang, etc., for their extensive help in daily life and studies.

Finally, I would like to thank my wife, Yongli Liu, for her constant prayer, love, and support. Many thanks also go to my parents and my parents-in-law for their love and encouragement, to my daughter, Siqi Yang, a gift from God, a constant source of joy and happiness.

Contents

Chapter 1

Introduction

1.1 Challenges from industry

The pressing requirements of better fuel economy and less carbon emissions from customers drive manufacturers to look continuously for better efficiency solutions. In the aviation industry, for example, the latest airliner Boeing 787 dreamliner in development aims for a 20 percent more fuel efficiency and 20 percent fewer emission than previous planes of a similar size. To achieve this goal, the new engines designed for it have to produce about 8 percent of these fuel efficiency gains. These stringent requirements push engine makers to look continuously for high temperature solutions because the efficiency of thermal engines increases if the temperature of working gas can be raised, according to the theory of the Carnot cycle. In the case of gas turbine engines, raising the temperature of the working gas means raising the turbine entry temperature (TET): the temperature of the hot gases entering the turbine arrangement [1]. In fact, for modern turbine engines, for example, the Rolls-Royce Trent 800 and General Electric GE90 which power the Boeing 777 with thrusts of more than 100 000lb, the operating temperatures are already beyond 800°C [1]. While in the electricity generation industry, the latest coal-fired power plant requires boiler tubing that can last up to 200 000 hours at 750°C and 100MPa of pressure [2]. With various strict requirements in resistance to fatigue, creep and corrosion under such high temperature working environments, superalloys are virtually the only choice

for those high temperature applications; their excellent high temperature properties enable them to find applications within key industries that include aerospace propulsion, chemical and metallurgical processing, oil and gas extraction and refining, and electricity generation. Arguably, the highest challenges encountered by these materials have emerged from the requirements for large, efficient land-based power turbines and lightweight, highly durable aeronautical jet engines [3], and the efforts to seek new grades of superalloy and processes never stop due to the ever increasing demands from the world.

1.2 The Superalloys

Superalloys are a class of material without exact boundaries. According to the definition utilized in *The Superalloys*, "A superalloy is an alloy developed for elevated temperature service, usually based on group VIIIA elements, where relatively severe mechanical stressing is encountered, and where high surface stability is frequently required" [4]. This definition seems still acceptable nowadays.

Usually superalloys are divided into three classes according to their chemical composition: nickel-base superalloys, cobalt-base superalloys, and nickel-iron base superalloys. Among them, the nickel-base superalloys are the most widely used for the hottest applications. They are also the most interesting sort of alloys for many metallurgists since their adoptions represent the highest temperature of application amongst those commonly used. In advanced aircraft engines, more than 50 percent of the weight comes from nickel-base superalloys [5]. The cobalt-base superalloys were relegated to a secondary position due to the rapid development of nickel-base superalloys which has greatly exceeded the capabilities of cobalt alloys. Nevertheless, cobalt alloys continue to be used for several reasons. Cobalt alloys in general offer superior hot-corrosion resistance to contaminated gas turbines atmospheres. Cobalt alloys usually show better thermal fatigue resistance and weldability to nickel alloys. The nickel-iron base superalloys are generally classified on the basis of their composition: containing about 25-60% nickel together with the element of

iron ranging from 15-60%. Some researchers take them just as a subdivision of the nickel-base superalloys. This class of superalloys is characterized by high temperature properties, relatively lower cost of production due to the greater usage of iron and better malleability. Inconel 718 (IN718) is a typical example in this class of superalloys. It finds widespread application in industry because of its excellent balance of properties, reasonable price, and its castability, forgeability. It is the material of choice for the great majority of engine parts in applications below 650°C. It in fact accounts for 40-50% of all superalloys produced [6]. Arguably, it is still the most successful superalloy even after nearly 50 years of its introduction [7, 8]. In this introduction, the attention is focused on nickel and nickel-iron base superalloys.

1.2.1 Historical development of nickel-base superalloys

The emergence of nickel-base superalloys can be dated back to the 1920s. Their origin can be traced back to the development of austenitic stainless steel for high temperature usage. In 1929, Bedford and Pilling, and almost at the same time Merica, added small amounts of titanium and aluminium to a nickel-chromium alloy, a new alloy with considerable improvement of creep strength was then got. This can be seen as the start of the era of nickel-based superalloys [9]. They gained rapid development during the following years driven continuously by the needs from jet engines and industrial gas turbines. Until now, the progresses in the field of superalloys are roughly represented by changes in two domains: chemical compositions and processing techniques.

After the effect of the coherent phase γ' was discovered, to improve the creep strength of alloys at high temperatures, more γ' forming elements such as aluminium (Al), titanium (Ti), and tantalum (Ta) were added to increase the proportions of γ' in superalloys. The γ' fraction of some single crystal superalloys can be as high as 70% [10]. Some refractory metal additions, such as molybdenum, tungsten, rhenium are also used in superalloys to provide additional strengthening through solid solution and carbide formation. In polycrystal superalloys, boron and carbon were also added to form borides and carbides for

grain-boundary strengthening. In single-crystal superalloys, these elements were removed since there is no need for grain-boundary strengthening; instead, rhenium (Re) and ruthenium (Ru) gradually take greater roles in the development of several generations of single-crystal superalloys. Generally speaking, based on an austenitic matrix, the composition of superalloys can be very complex. The chemical compositions of some typical cast and wrought superalloys are shown in Table 1.1 and Table 1.2 respectively [1].

The processing techniques for superalloys have also witnessed the great progresses. In the early days, the superalloy parts were made only through the conventional cast / wrought route, which was already popular for other alloy systems. Then investment casting was used to produce parts of complex shapes. In the 1950s, vacuum melting technology including vacuum induction melting (VIM) and vacuum arc remelting (VAR) became commercially available; this was a great breakthrough for producing high strength superalloys since these techniques enable the elimination of detrimental trace elements and the addition of the reactive elements used for precipitation strengthening of alloys. Later, directional solidification (DS) - a new casting technique developed at Pratt and Whitney - was used to make airfoils, which led to the rapid development of directionally solidified (DS) and single crystal (SX) superalloys. Nowadays, single crystal superalloys are used heavily in the high pressure turbine engines for their excellent creep resistant and thermal fatigue resistant properties. Almost during the same period as the emergence of directional solidification, for those superalloys used in polycrystalline form, for example, turbine discs in aeroengines, the idea of oxide dispersion strengthening (ODS) was incorporated in production, which led to the change of the processing route for some high performance superalloys from traditional ingot metallurgy, i.e, the conventional cast and wrought route, to powder metallurgy, which is preferred in production of heavily alloyed grades such as Rene95 and RR1000 [1, 9, 11]. Fig.1.1 gives a historical view of the advancement of alloys and processes for turbine blades over the last 60 years [1]. The data describe the highest temperature for each alloy at which rupture occurs in no less than 1000 h under a stress of 137MPa. From the graph, it is obvious that direction solidification of single crystal has been preferred in this application in recent years.

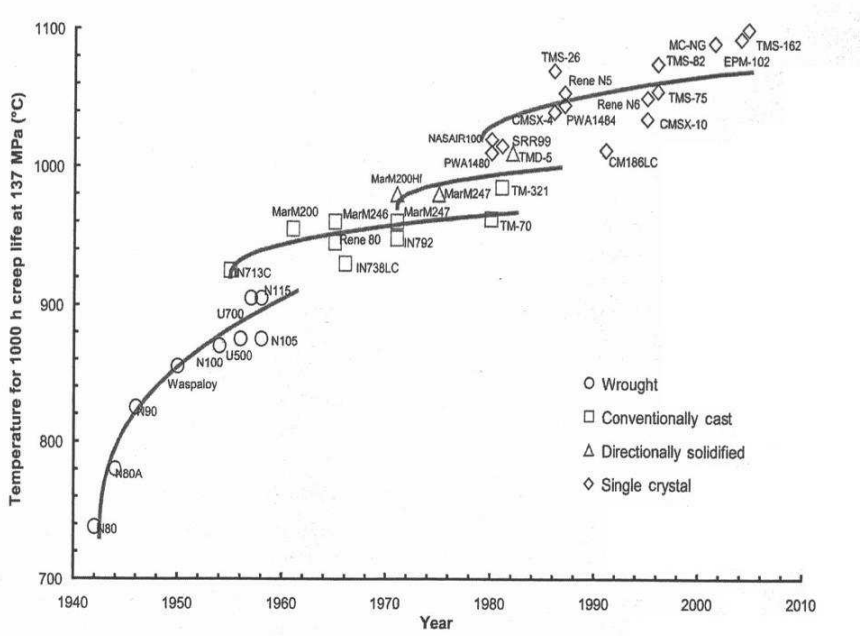

Figure 1.1: Development of the high-temperature capability of the superalloys for turbine blades since their emergence in the 1940s [1].

Another active direction in the processing of superalloys is coating processing. In fact, the means to ensure coatings of proper and stable performance during service is a critical issue in the modern gas turbine field. Without protection by these coatings, the components in the combustor and turbine sections would degrade very quickly due to the extreme operation conditions there. There are several coating techniques available for superalloys: diffusion coating, overlay coating, thermal barrier coating. Fig.1.2 gives a schematic illustration of their service life and temperature enhancement abilities [1].

Table 1.1: Compositions of some cast Ni-base superalloys [1].

Alloy	Cr	Co	Mo	W	Al	Ti	Ta	Nb	Re	Ru	Hf	C	B	Zr	Ni
CMSX-2	8.0	5.0	0.6	8.0	5.6	1.0	6.0	–	–	–	–	–	–	–	Bal
CMSX-4	6.5	9.6	0.6	6.4	5.6	1.0	6.5	–	3.0	–	0.1	–	–	–	Bal
CMSX-10	2.0	3.0	0.4	5.0	5.7	0.2	8.0	–	6.0	–	0.03	–	–	–	Bal
IN100	10.0	15.0	3.0	–	5.5	4.7	–	–	–	–	–	0.18	0.014	0.06	Bal
IN713LC	12.0	–	4.5	–	5.9	0.6	–	2.0	–	–	–	0.05	0.01	0.10	Bal
IN738LC	16.0	8.5	1.75	2.6	3.4	3.4	1.75	0.9	–	–	–	0.11	0.01	0.04	Bal
Mar-M200Hf	8.0	9.0	–	12.0	5.0	1.9	–	1.0	–	–	2.0	0.13	0.015	0.03	Bal
Mar-M246	9.0	10.0	2.5	10.0	5.5	1.5	1.5	–	–	–	1.5	0.15	0.015	0.05	Bal
Mar-M247	8.0	10.0	0.6	10.0	5.5	1.0	3.0	–	–	–	1.5	0.15	0.015	0.03	Bal
Nasair 100	9.0	–	1.0	10.5	5.75	1.2	3.3	–	–	–	–	–	–	–	Bal
PWA1480	10.0	5.0	–	4.0	5.0	1.5	12.0	–	–	–	–	–	–	–	Bal
PWA1484	5.0	10.0	2.0	6.0	5.6	–	9.0	–	3.0	–	0.1	–	–	–	Bal
PWA1497	2.0	16.5	2.0	6.0	5.55	–	8.25	–	5.95	3.0	0.15	0.03	–	–	Bal
Rene 80	14.0	9.0	4.0	4.0	3.0	4.7	–	–	–	–	0.8	0.16	0.015	0.01	Bal
Rene N5	7.0	8.0	2.0	5.0	6.2	–	7.0	–	3.0	–	0.2	–	–	–	Bal
Rene N6	4.2	12.5	1.4	6.0	5.75	–	7.2	–	5.4	–	0.15	0.05	0.004	–	Bal
RR2000	10.0	15.0	3.0	–	5.5	4.0	–	–	–	–	–	–	–	–	Bal
SRR99	8.0	5.0	–	10.0	5.5	2.2	12.0	–	–	–	–	–	–	–	Bal
TMS-75	3.0	12.0	2.0	6.0	6.0	–	6.0	–	5.0	–	0.1	–	–	–	Bal
TMS-138	2.9	5.9	2.9	5.9	5.9	–	5.6	–	4.9	2.0	0.1	–	–	–	Bal
TMS-162	2.9	5.8	3.9	5.8	5.8	–	5.6	–	4.9	6.0	0.09	–	–	–	Bal

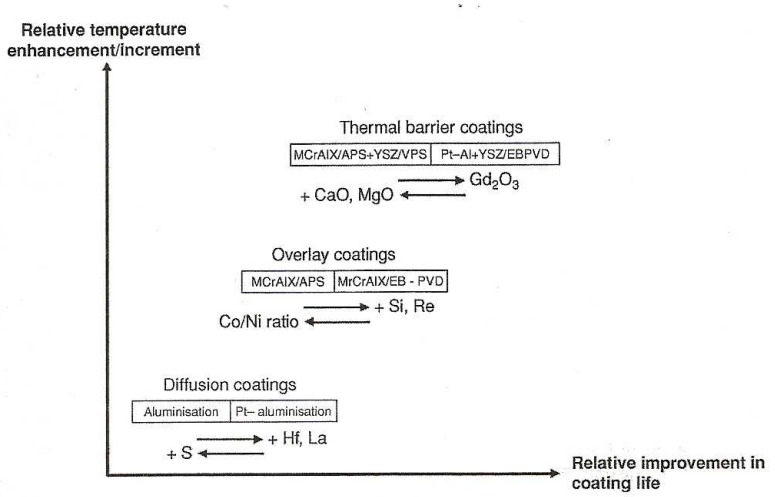

Figure 1.2: Illustration of the three common forms of protective coating used for turbine applications [1].

1.2.2 Microstructure of nickel-base superalloys

The high temperature capabilities of superalloys are closely related to the characteristics of their microstructures. While it may not be possible to explain the properties of the nickel-base superalloys by just one mechanism, precipitate hardening - mainly by γ' or γ'' - plays a major and unique role in strengthening the nickel-base superalloys. The γ matrix of nickel-base superalloys is an austenitic *fcc* phase containing a high fraction of elements such as chromium, molybdenum, tungsten and cobalt. The precipitates, γ' or γ'', are stable inter-metallic compounds formed by an ordering reaction from the γ matrix, which makes them coherent with the γ matrix. This coherency between the matrix and precipitates is generally believed among researchers to be the paramount reason for their prominent strengthening effects in superalloys [12].

Table 1.2: Compositions of some wrought Ni-base superalloys [1].

Alloy	Cr	Co	Mo	W	Nb	Al	Ti	Ta	Fe	Hf	C	B	Zr	Ni
Astroloy	15.0	17.0	5.3	–	–	4.0	3.5	–	–	–	0.06	0.030	–	Bal
C-263	16	15	3	1.25	–	2.50	5.0	–	–	–	0.025	0.018	–	Bal
Hasterlloy X	22.0	1.5	9.0	0.6	–	0.25	–	–	18.5	–	0.10	–	–	Bal
Hasterlloy S	15.5	–	14.5	–	–	0.3	–	–	1.0	–	–	0.009	–	Bal
Inconel 600	15.5	–	–	–	–	–	–	–	8.0	–	0.08	–	–	Bal
Inconel 625	21.5	–	9.0	–	3.6	0.2	0.2	–	2.5	–	0.05	–	–	Bal
Inconel 706	16.0	–	–	–	2.9	0.2	1.8	–	40.0	–	0.03	–	–	Bal
Inconel 718	19.0	–	3.0	–	5.1	0.5	0.9	–	18.5	–	0.04	–	–	Bal
Nimonic 80A	19.5	–	–	–	–	1.4	2.4	–	–	–	0.06	0.003	0.06	Bal
Nimonic 90	19.5	16.5	–	–	–	1.5	2.5	–	–	–	0.07	0.003	0.06	Bal
Nimonic 105	15.0	20.0	5.0	–	–	4.7	1.2	–	–	–	0.13	0.005	0.10	Bal
Pyromet 860	13.0	4.0	6.0	–	0.9	1.0	3.0	–	28.9	–	0.05	0.01	–	Bal
Rene 41	19.0	11.0	1.0	–	–	1.5	3.1	–	–	–	0.09	0.005	–	Bal
Rene 95	14.0	8.0	3.5	3.5	3.5	3.5	2.5	–	–	–	0.15	0.010	0.05	Bal
RR1000	15.0	18.5	5.0	–	1.1	3.0	3.6	2.0	–	0.5	0.027	0.015	0.06	Bal
Udimet500	18.0	18.5	4.0	–	–	2.9	2.9	–	–	–	0.08	0.006	0.05	Bal
Udimet700	15.0	17.0	5.0	–	–	4.0	3.5	–	–	–	0.06	0.030	–	Bal
Udimet720	17.9	14.7	3.0	1.25	–	2.5	5.0	–	–	–	0.035	0.033	0.03	Bal
Udimet720LI	16.0	15.0	3.0	1.25	–	2.5	5.0	–	–	–	0.025	0.018	0.05	Bal
Waspaloy	19.5	13.5	4.3	–	–	1.3	3.0	–	–	–	0.08	0.006	–	Bal

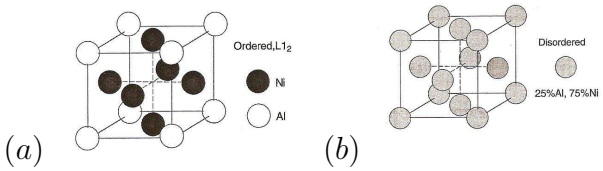

Figure 1.3: Arrangements of Ni and Al atoms in (a) the ordered Ni_3Al phase and (b) after disordering [1].

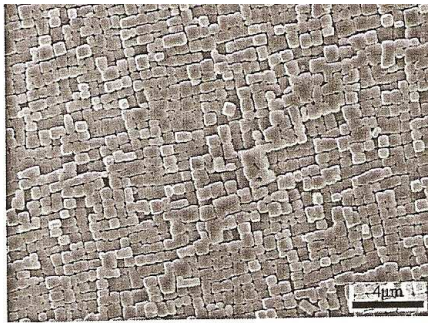

Figure 1.4: A SEM image of γ' precipitates [14].

The composition formulae of γ' phase is $Ni_3(Al,Ti)$. It possesses a $L1_2$ crystal structure, which is similar to the fcc matrix, but has aluminium or titanium substituting for the nickel atoms at the cube corners, as shown in Fig.1.3. The γ' phase usually is in the shape of a sphere or cuboid in scanning electron microscopy (SEM) images. Its amazing rise of strength with temperature over a certain temperature range is the most important reason for superalloys to keep their strength under high temperature environments. Fig.1.5 gives an illustration of the rise of flow stress for γ' phase with the increase of temperature [13].

The chemical composition for γ'' is $Ni_3(Nb,Ta)$. This precipitate is most commonly found in niobium-containing alloys such as Inconel 718, 706, in which the primary strengthening effects is believed provided by this phase instead of γ'. The γ'' precipitates possess a body centered tetragonal (BCT) DO_{22} crystal structure, which is displayed in Fig.1.6. These particles form as fine platelets either coherently or semi-coherently within the γ matrix [15].

Apart from γ' and γ'', the carbides also arouse a lot of interest among metallurgists. The carbides come from the combining of carbon with the alloying elements. The role of carbides in superalloys is complicated. As mentioned previously, carbon is added to the su-

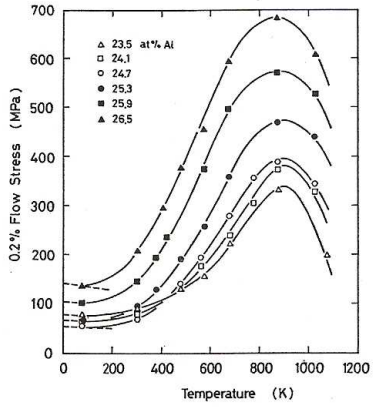

Figure 1.5: Rise in flow stress of γ' with temperature at various Al contents [13].

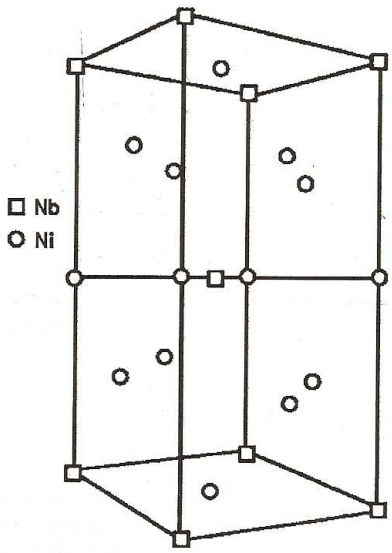

Figure 1.6: The unit cell of the γ'' precipitates [1].

peralloy system to form carbides for grain boundary strengthening since the carbides have tendency to precipitate at grain boundaries during post solution heat treatment. Usually a small amount of carbides such as 0.025wt% is considered beneficial to the alloy properties as their existence can help to achieve a fine grain size of the component due to their pinning effect on grain boundaries. However, if large amounts of carbides are found at grain boundaries, especially when the carbides precipitate as a continuous grain boundary film, the alloy can become brittle and exhibit poor ductility. The common carbides encountered in nickel-base superalloys are MC, $M_{23}C_6$, and M_6C [1, 16].

Usually after long exposure / service time, or in some alloys where the composition may not have been carefully controlled, some undesirable phases may appear. These topologically closed packed (TCP) phases (such as σ and μ) usually form a basket weave structure aligned with the octahedral planes of the γ matrix. Generally these phases are detrimental since they promote crack initiation and growth [5].

In summary, based usually on a classical γ - γ' structure, the phases in nickel-base superalloy can be very complicated. To control their quantities, distribution, morphology in microstructure through optimization of chemical compositions and processing techniques to ensure even better performances of superalloys is still an intriguing topic to metallurgists.

1.2.3 Inconel 718

Inconel 718 (IN718) is a wrought nickel-iron based alloy for moderately high temperature applications developed by H.L.Eiselstein of the International Nickel Company [8]. It has gained widespread application due to its high strength and good malleability. The composition of IN718 can be found in Table 1.2. Its solidus and liquidus temperature are 1260 °C and 1335 °C respectively [17]. The major intermetallic phases known to precipitate in IN718 are the metastable phases γ', γ'', and the equilibrium δ phase. The γ' occupies a volume fraction of about 4-6%. The primary strengthening phase γ'', with the composition of Ni_3Nb, precipitates coherently as ellipsoidal, disk-shaped particles on $\{100\}$ planes of the *fcc* matrix, and has an ordered body-centred tetragonal (DO22) structure. The γ''

has a volume fraction of 15-20% in IN718. The equilibrium δ phase has an orthorhombic structure, and represents the thermodynamically stable form of the metastable γ'', with the same composition Ni_3Nb [5]. Researches have shown that the main strengthening phase in IN718 loses stability after exposure to temperatures in excess of 650°C. The γ'' particles coarsen above 650°C and the strength of the alloy degrades [5]. The precipitation kinetics and morphology of δ phase in IN718 are also of great interest to researchers. The rate of formation of δ phase is usually quite slow below 700°C. A significant acceleration for the formation of δ phase occurs above 700°C and is accompanied by a rapid coarsening of γ'' up to 885°C, above which re-solutioning of the γ'' particle occurs [5].

An illustration of the variation of the fraction of phases with the temperature in Inconel 718 calculated using software package ThermoCalc is shown in Fig.1.7.

1.3 Friction Welding

Many of the components fabricated from the superalloys have traditionally required some form of joining operations since net-shape manufacturing is not always feasible. Usually, some kind of fusion welding methods is used in the welding of superalloys. For example, gas tungsten arc welding (GTAW) and plasma arc welding (PAW) methods are used in joining turbine combustors. Similarly, electron beam welding (EBW) is used widely for the joining of the compressor, which consists of a number of discs and rings welded together to form a drum, onto which the compressors blades are arranged [18, 19]. However, there are problems to apply these technologies to the latest grades of high-strength superalloys, in which the volume fraction of the hardening phase γ' can be as high as 70%, as it is generally accepted in the welding of superalloys that the higher content of γ' an alloy possesses, the more difficult it is to be welded. The common problems encountered in the welding of superalloys with these fusion welding methods are hot cracking and post-weld heat treatment (PWHT) cracking, which is also called strain age cracking or delay cracking [16]. In addition to the problem of cracking in the welding of superalloys, the degradation of mechanical properties of welds is another issue. In fact, it is not uncommon to have

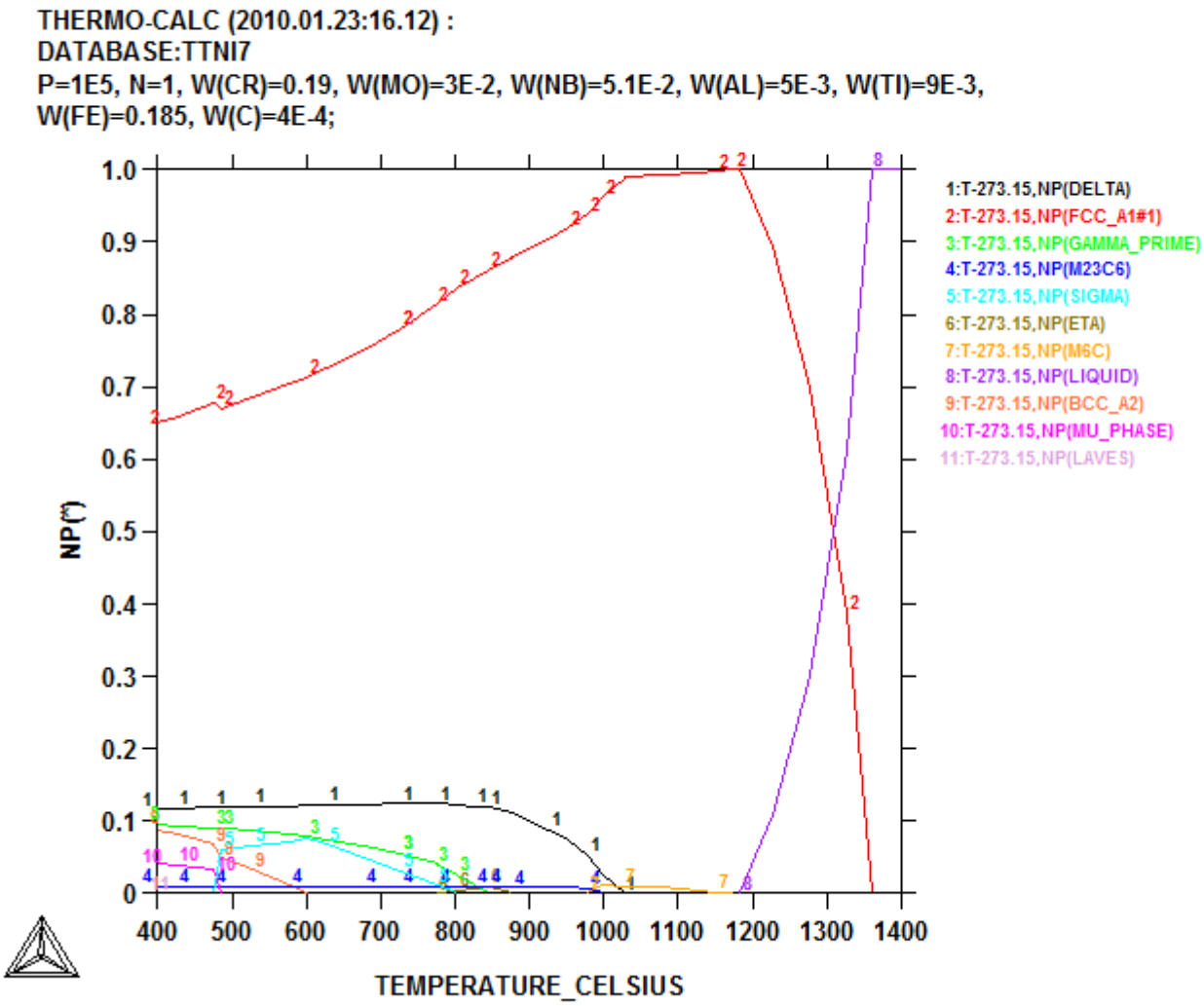

Figure 1.7: The fraction of phases in IN718 with the change of the temperature, Thermo-Calc with database: TTNI7.

superalloy welds designed with the joints region thicker to reduce the stresses at the weld to achieve a practical, usable welded structure [16].

While conventional fusion welding methods are not readily amenable to join the latest grades of high-strength superalloys, friction welding techniques are being developed in such applications. According to the definition given by American Welding Society, "friction welding is a process that produces a weld under compressive force contact of workpieces rotating or moving relative to one another to produce heat and plastically displace material from the faying surfaces" [18]. It is believed that a joint can thus be produced without incurring the gross melting of the material; as a result, the cracking and gross distortion of the welds during solidification are considerably reduced. Further, there are extra advantages of friction welding when compared with fusion welding techniques. According to *Welding Handbook* produced by the American Welding Society, some of them are listed as follows [18]

- No filler metal is needed.
- Flux and shielding gas arc are not required.
- The process is environmentally clean; no arcs, sparks, smokes or fumes are generated.
- Surface cleanliness is not significant, compared with other welding processes, since friction welding tends to disrupt and displace surface films.
- There are narrow heat-affected zones.
- Friction welding is suitable for welding most engineering materials and is well suited for joining many dissimilar metal combinations.
- In most cases, the weld strength is as strong or stronger than the weaker of the two materials being joined.
- Operators are not required to have manual welding skills.
- The process is easily automated for mass production.
- Welds are made rapidly compared to other welding processes.

- Plant requirement (space, power, special foundations, etc) are minimal.

Basically, there are three kinds of friction welding distinguished by the tracks the welding objects run along during the process: rotary, linear, and orbital. Rotary friction welding is the oldest method in which one part is rotated around its axis while the other remains stationary. Then the two parts are brought together under application of pressure. In linear friction welding, which has been used since the 1980s, the components move under friction pressure relative to each other in a reciprocating manner through a small linear displacement (amplitude) in the plane of welding interface. Orbital friction welding, introduced in 1970s, is a combination of linear and rotary friction welding. In this process, the centre of one welding part relative to the other one is moved around a two-dimensional curve, *e.g.* a circle, to provide the rubbing action. The two parts to be welded are rotated around their longitudinal axes in the same sense with the same constant angular speed. The two longitudinal axes are parallel except for a small offset. When motion of the components ceases, the two parts are realigned quickly to their desired orientation and formed together under pressure [20].

Parts to be welded with circular cross section are most frequently encountered in the

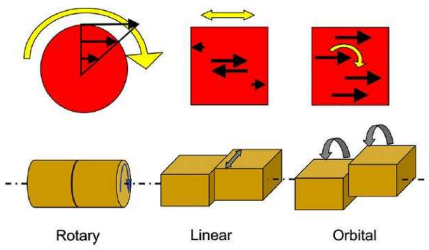

Figure 1.8: Three variants of friction welding. A comparison of heat generation over the interface for three types of friction welding is shown with black arrows [20].

friction welding industry, which indicates that the rotary friction welding is the most pop-

ular one. There are two variants of rotary friction welding. One is direct drive friction welding, or continuous drive friction welding, in which the energy is provided by direct drive at predetermined rotational speed or speeds. The other one is inertia welding, also called stored energy friction welding or flywheel friction welding, in which energy stored in a flywheel is used up in the process by component induced braking [21]. In this study, modelling of rotary friction welding process is considered, with attention being paid to inertia welding. So in the later part of this thesis, the term of friction welding refers only to rotary friction welding if there is no further explanation.

1.3.1 Historical Background of Friction Welding

Friction welding can be taken as a special kind of forging welding process according to the definition of the American Welding Society since it involves large amount of plastic deformation near welding interfaces [22]. The idea of using frictional heat for welding metal was first adopted by J.H.Bevington in the USA in 1891 [23, 24]. However, this idea did not get much acceptance in these early days. More patents were granted for welding thermoplastic pipes later [25, 26, 27]. In 1956, A.I.Chudikov revived the idea and successfully got high-quality butt metal welds through friction welding [28]. Since then, intensive study has been carried out; its application can be found throughout the industry of manufacturing, and lots of patents have been granted for their usage in agricultural machinery, automobile, aeroengine, and electrical engineering [29, 30, 31, 32, 33, 34].

1.3.2 Procedure of Friction Welding

The basic steps of rotary friction welding are illustrated in Fig.1.9. For the direct drive process, one part is kept stationary while the other is rotated at a constant speed. An axial compression force is then applied to make the two parts rub against each other. After a predetermined time span or amount of axial shortening (upset) is reached, the drive is disengaged and a brake is used to stop the rotating part. The axial force is maintained or increased at the same time until the weld has cooled. So the main process variables for

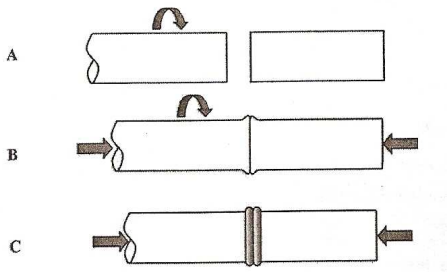

Figure 1.9: Basic steps in rotary friction welding process A: one specimen rotates and the other is stationary; B: two specimens are brought together as an axial force is applied; C: process is complete when rotation of one specimen stops and upsetting ceases [35].

direct drive friction welding are rotation speed, axial force, brake time and welding time. These parameters determine the rate of heat generation in the welding interface and the amount of energy input into the weld.

In the case of inertia welding, one component is first attached to a flywheel and accelerated to a high angular velocity; welding begins when the other stationary part is pushed against it just after the driving power is shut off, so that the speed of the rotating part drops rapidly to a halt. The axial force is also maintained when the weld cools. Similarly, there are three controllable parameters in inertia welding: rotation speed, axial force and flywheel mass (expressed by moment of inertia). The speed of rotation decreases gradually throughout the process, the rate at which the speed decreases depends on the axial pressure, and the inertia of the rotating component [35]. A part produced by inertia weld is displayed in Fig.1.10.

Basically we can divide friction welding procedure into three stages [36]. The first stage is the heating stage, which is dominated by the dry friction generated under the applied load as soon as the two components come into contact under pressure. The temperature in the rubbing surfaces rises rapidly in a short period of time. When the temperature in the mating surfaces reaches a highest point close to the melting temperature, the torque exerted on the components by the friction force in the mating interface drops to a lower, steadier level. This corresponds to a second, steady-state being reached. It is here that the flash forms, with the torque reaching a maximum at the end of this stage. The 3rd stage is

Figure 1.10: A photograph of an inertia welded component.

characterized by the cooling of the weld due to the cessation of the rotation while the axial force is maintained. The variations of process parameters and different stages of the direct drive friction welding and inertia welding process are illustrated in Fig.1.11.

1.3.3 Materials welded

Friction welding is used to join a wide range of similar and dissimilar materials, for example, metals, ceramics, metal matrix composites and plastics. The weldability of materials is illustrated in Fig.1.12 according to the *Welding Handbook* by the American Welding Society [18]. However, this figure should only be used as a reference. Specific weldability depends on a lot of factors.

Principally, joining can be successful if at least one component can undergo large plastic deformation. However, metals good for dry bearing are not suitable for friction welding, for example, cast iron in any form, (the free graphite in it limits frictional heating,) and the same is also true for bronzes and brasses which have a high lead content, due to similar reasons.

There are also some dissimilar metal combinations that displayed marginal weldability. Examples are aluminium alloys joined to steels, or copper and stainless steel to titanium alloys. The possible explanation may be that these combinations may tend to form brittle intermetallic compounds or involve large differences in the hot forging temperatures of the metals to be welded [22].

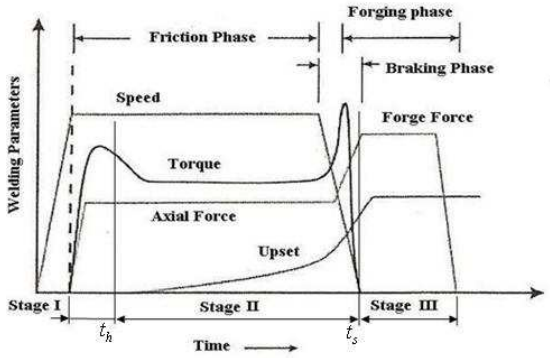

(a)

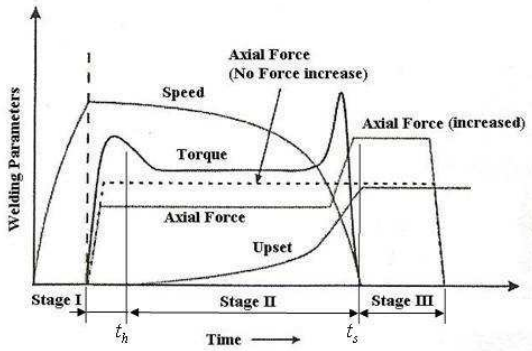

(b)

Figure 1.11: Schematic illustration of variation of friction welding parameters (a) Direct drive friction welding (b) Inertia friction welding [35].

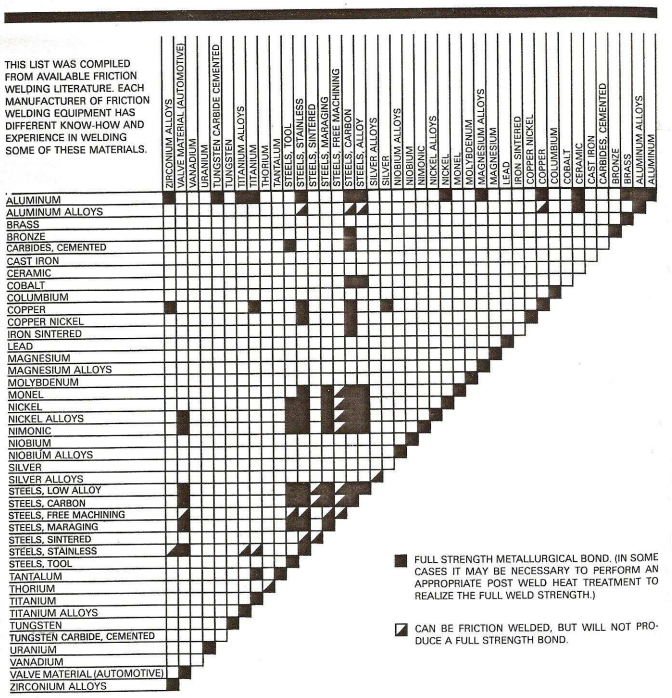

Figure 1.12: Material combinations weldable by friction welding [18].

1.4 Objectives for this work

The quality of the weld produced by friction welding is closely related to the process parameters. To assure the integrity of the welded products, the process parameters need to be optimized. This is usually done through experimental trial and error, which is effective but also expensive. This is especially true in the case of welding superalloys. Further, the empirical method is time consuming and has little flexibility.

Therefore, the aim of this study is to build fundamental models to predict the temperature, heat affected zone dimensions, and axial shortening (upset) in friction welding. The models put forward in this work should add to the understanding of friction welding processes and have the potential for optimising the process parameters for cost effective designs.

Chapter 2

Literature Review

2.1 Fundamentals of friction welding

2.1.1 Frictional behaviour

Friction is the force resisting the relative tangential motion of solid surfaces, fluid layers, or material elements in contact [37]. The increase of temperature arising during friction welding is due to the conversion of the kinetic energy of the moving objects into thermal energy by friction. In spite of the importance of the role of friction in friction welding, there is still little progress in understanding frictional behaviour of materials. The Coulomb model, which states that the friction force is proportional to the load while independent of contact area, is still the most common model used in friction analysis. It is expressed as follows

$$F_f = \mu_0 F_N \tag{2.1}$$

where F_f is the friction force developed, F_N is the normal force between the contact surfaces, and μ_0 is the friction coefficient, which is usually determined empirically. As the determination of the friction coefficient is believed to be a key to successful modelling of friction welding, much effort has been put into this area. Wang simplified the problem by assuming the product of the friction coefficient and pressure $\mu_0 \cdot P$ is constant along the mating surface [38]. Earlier, Vill suggested that the friction coefficient could be taken as a

function of rotation speed and radial position [28]

$$\mu_0(r,t) = \frac{C_0}{\omega(t) \cdot r^2} \tag{2.2}$$

where C_0 is constant coefficient, determined from experimental results. Based on some experiments, Balasubramanian *et al* proposed a formula for friction coefficient taking the influence of temperature T, axial pressure P, and sliding speed V into account [39],

$$\mu_0 = a_0 T^{a_1} P^{a_2} V^{a_3} \tag{2.3}$$

where a_0, a_1, a_2, a_3 are all constant coefficients and need to be determined by regression methods. Another approach to determine the form of friction law was put forward by Moal [40, 41], in whose model the welding process is divided into two stages: in the beginning of the heating stage, the friction stress is assumed to obey the classical Coulomb's friction law,

$$\tau_f = -\mu_0 P \frac{\Delta \bar{V}_S}{\left|\Delta \bar{V}_S\right|} \tag{2.4}$$

where τ_f is the friction stress, μ_0 is the friction coefficient, P is the axial load pressure and ΔV_S the sliding rotating speed. When the temperature in the mating surface rises to a certain point, the friction behaviour was taken to be the same as in a thin Norton-Hoff layer subjected to a shear stress. As the shear stress decreases when temperature increases, the friction law becomes temperature dependent,

$$\tau_f = -\mu_0 K(T) \frac{\Delta \bar{V}_S}{\left|\Delta \bar{V}_S\right|} \tag{2.5}$$

where $K(T)$ is the thermo-dependent material consistency. However, the transition criterion of the friction stage has to be determined experimentally. More recently, based on experimental data, D'Alvise presented a model to describe the friction coefficient in inertia welding [42],

$$\tau_f = \mu_0(\Delta V_S) P^{(1-r)} \sigma_0^r \tag{2.6}$$

where $\mu_0(\Delta V_S)$ is the apparent friction coefficient, which is the function of the sliding rotating velocity, P is the pressure applied, and σ_0 is the yield stress. The term r is the transition parameter, which needs to be decided by inverse analysis of experimental data.

Although lots of expressions for friction coefficient have been postulated - as Rich and Roberts pointed out in 1971 [43] and still agreed upon by Maalekian in 2007 [35] - there is no general applicability for most of these models due to the complexity of this problem. Hence, it is rather difficult to predict the exact value of the friction coefficient, particularly for friction welding processes. The widely accepted knowledge is: when the contact shear stress is smaller than the shear yield stress of the mating materials, the sliding condition is met and the Coulomb friction law can be applied; if the contact shear stress is equal to the shear yield stress, sticking state is reached, and the value of the friction coefficient for friction welding processes drops if the shear yield stress drops because of the rapid temperature rise at the mating interface. However, the transition point is difficult to predict since lots of factors influence the frictional behaviour, such as contact geometry, temperature, applied forces, sliding speeds, and material properties.

2.1.2 Metallurgical characteristics

Metallographic study of weld areas in friction welding has been conducted extensively [36, 44, 45, 46, 47, 48]. During friction welding, the material near the welding interface undergoes drastic temperature changes and consequently some changes in its microstructure. This region is referred to as the heat affected zone (HAZ). Usually the HAZ can be divided into several regions, as shown in Fig.2.1.

The contact zone is the zone which experiences the maximum temperature. The metals in this area rub with each other and fragments of metals transfer from one rubbing surface to the other. The strain rate in this region is mainly controlled by the rotational speed. As the width of this region is in the range of 20-100 μm, the strain rate can be as high as 1000 s^{-1}. Under such extreme conditions, some researchers hold that a thixotropic deformation behaviour is facilitated [36]. The material in this zone has a very fine grain size due to severe plastic deformation and full recrystallisation. Some authors also think there is partial melting of materials in this region [36, 49, 42].

It is not difficult to appreciate that the flow behaviour of the metal in this region can have very important influence on the quality of the friction welds. There is nevertheless

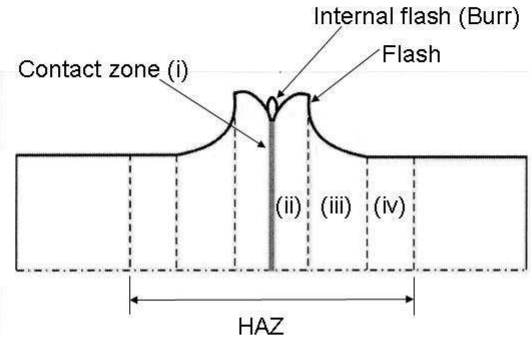

Figure 2.1: Schematic illustration of different regions in HAZ of friction welds, (i) contact zone (ii) fully plasticised zone (iii) partly deformed zone (iv) undeformed zone [35].

little work focussed in this area given the research efforts in friction welding. In this study, a model for it is detailed in the later part of this dissertation.

The fully plasticised zone, shown in region (ii), is the zone where the component undergoes large plastic strain. The temperature in this area is also high enough for recrystallisation since this region is close to the rubbing surfaces. The metals in this zone experience dynamic recrystalisation and hence have fine equi-axed grains. The width of this region is about 0.5-1mm [47, 48].

The partly deformed zone is the region where the amount of strain, shown in region (iii), and temperature are lower than the former fully plasticised one. There may be only dynamic recovery with coarser grain structure here.

The undeformed zone, shown in region (iv), is the zone with no plastic deformation. The materials here may have undergone phase transformations and grain growth, however.

In friction welding, flashes are caused by the severe plastic deformation of metals near the weld line. The shape of flash is usually similar to that shown in Fig.2.1. There is often

some material extruded out along weld line in friction welding, particularly at the end of flash forming stage, this part of metal is stated as internal flash in D'Alvise's PhD thesis [42], which is also mentioned as burr according to British standard [21]. A picture of flashes in inertia welding of superalloys is illustrated in Fig.2.2. To the author's knowledge, there is no clear explanation why this burr happens during friction welding. For instance, in British standard BS ISO 15620, the cause of burr is often claimed unknown. In this dissertation, a model is put forward which aims to shed some light on this subject.

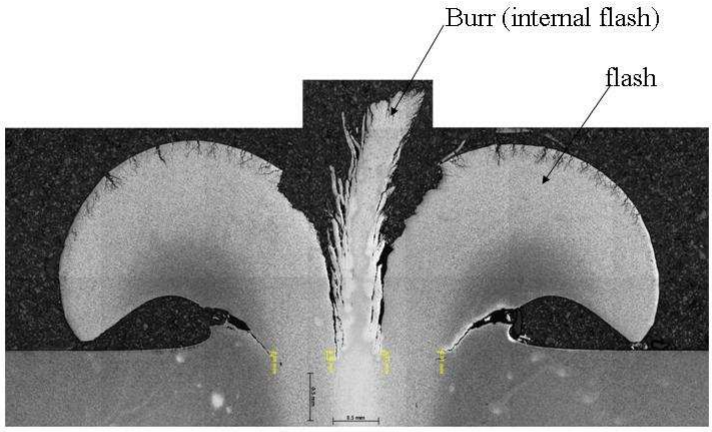

Figure 2.2: An illustration of flashes in inertia friction welding [50].

2.1.3 Temperature distribution

In friction welding, the question of the temperature at the mating surfaces, or whether there is melting at the interface is a controversial one. As it is important to know the thermal behaviour of the HAZ, considerable efforts have been made to analyse the temperature distribution. Thermocouples have been used to estimate the temperature variation during a typical welding cycle. However, the thermocouple readings are usually unreliable due to the damage brought about by the plastic flow of the material near the weld line.

This difficulty in measuring the temperature with thermocouples has provided researchers an incentive to use other methods. Some adopted the non-contact measuring method of optical pyrometry. Others tried to make thermal analysis through indirect methods, *i.e.* metallographic study of the microstructure of the HAZ or theoretical study to predict the temperature at the weld line. Fu *et al*, and Soucail *et al* adopted the infrared detection method to measure temperatures at the weld line [49, 51]. In Fu's paper, the results for the temperature detected are not clearly presented. While in Soucail's experimental results, a temperature of 1280°C is reported when inertia welding a superalloy of Astroloy, the solidus and liquidus of which are 1250°C and 1345°C respectively. This means that there is a partial melting at the mating surface. Milding and Grong also reported there was a liquid layer at the mating surfaces when friction welding Al-Mg-Si alloys to Al-SiC metal matrix composites [36]. However, the prevailing view on this matter is that melting does not occur at the interface during friction welding. The main reason for people who are against the existence of melting is that the soft layer at the mating surfaces would be easily expelled out under the axial pressure before melting starts [38, 43, 44, 52, 35]. This view was often supported by the metallurgical observations of the welding zone since almost no typical microstructure of solidification, *i.e.*, dendrite like structure, was found in metallographic examinations. But this thought meets difficulty in explaining the phenomenon of the extrusion of the burr during friction welding.

2.2 Models for friction welding

In practice, many aspects of the friction welding process are difficult to detect experimentally; this is particularly true of the thermal cycles close to the rubbing surfaces and the associated constitutive behaviour of the material as it softens and deforms plastically. This situation means that analysis of the phenomena occurring by modelling techniques has considerable value. Lots of models have been put forward to describe the procedure, which can be divided into two categories: analytical ones and numerical ones.

2.2.1 Analytical models

Rykalin *et al* were some of the first to consider this problem; they developed a one-dimensional model of friction welding and in particular a closed-form solution for the temperature field [53]. The assumptions made in their paper were semi-infinite solid, zero initial temperature, and constant thermal material properties; the expression derived is an exact analytical solution for the temperature distribution provided that there is no steady-state stage and that heat convection and radiation from the lateral surfaces can be neglected. However, usually there is a steady state during friction welding, and this limits its applicability.

Based on the thermal results got by the finite difference method (FDM), Rich and Roberts studied the forging phase of friction welding utilising upper boundary theory of plastic deformation [43, 54]. This was the first attempt reported to study the material flow in the HAZ analytically. They took the friction welding as a form of pressure welding and held that the actual bonding takes place primarily during the forging phase of direct drive friction welding. The material flow were also simulated with gridded plexiglass specimens experimentally in their work. They stated that the extent of the abutting material expelled into the weld flash is not only closely related to the amount of the upset, but also to the shape of the plastic deformation zone in the HAZ.

Healy *et al* made a dynamical analysis of the steady-state stage of friction welding thin-walled tubes of the mild steel. They presented an interesting model to describe the behaviour of the plasticised layer, also called the boundary layer, near the contact section in friction welding. In this model, some physical mechanisms during steady-state stage were postulated: (1) A layer of plasticised material exists at the abutting interface. (2) Heat is generated by viscous dissipation within this layer, and removed as sensible heat by the extruded material. (3) The high temperature close to the interface causes a decrease in the strength of the solid material, which is insufficient to carry the axial load. Thus a hydrodynamic pressure must exist so that the sum of the pressure plus the compressive strength of the solid material just balances the stress from the axial load. This hydrodynamic pressure then provides the driving force for the extrusion of plasticised material. A

one-dimensional thermal analysis was coupled with mechanical analysis by using a temperature dependent Bingham plastic constitutive equation. A series of interesting formulae, *i.e.* the expressions for the torque, the temperature at the interface, the viscosity and thickness of the plasticised layer, were got after some elementary algebraic manipulation. The model claimed good prediction of the change of the torque during process. However, the analysis presented avoided predicting axial shortening rates under various rotation speeds and compression loads, which is generally believed to be the most important factor to control the weld quality, instead, this information was assumed already available in this model, which means it is hard to apply in practice [55].

Francis and Craine studied the friction stage in continuous drive friction welding of thin-walled steel tubes. The friction stage in their paper is referred as steady-state stage in this study. In their model, the softened material was assumed as a Newtonian fluid of large viscosity. The authors claimed their model can represent many qualitative features of real welds. But their predictions were not verified by experimental data [56].

Middling and Grong studied the HAZ temperature and the strain rate distribution during the continuous drive friction welding of Al-Mg-Si alloys and Al-SiC metal matrix composites. They developed a multistage thermal model for friction welding by the modification of Rykalin's semi-infinite rod solution, in which the process of continuous drive friction welding was divided into three stages; closed-form solutions for each of these three stages were given [36]. As for the models mentioned above, the formulae were deduced from a 1D heat flow model. The predicted temperatures were broadly in agreement with the measured data even though the axial shortening was not taken into account. In their paper, the material flow was also simulated by setting up a series of velocity fields of the HAZ material based on the knowledge from metallographic examinations. They concluded that the strain rate of materials in HAZ is mainly determined by the rotation speed, which may exceed 1000 s^{-1}; outside the fully plasticised region, the material flow is controlled by the axial shortening rate, which means a dramatic drop of strain rate. The authors also modelled the variations of the microstructure and strength of the HAZ on the basis of established principles of thermodynamics, diffusion theory and simple dislocation mechanics [45].

More recently, Dave *et al* built a simple analytical model for the study of inertia welding of pure niobium and 316L stainless steel tubes. By the principle of energy conservation, the temperature profiles were calculated using machine generated data. They also suggested a method to select parameters for inertia welding when the part size is changed, by assuming that the power dissipation characteristic as a function of time is a good means of transferring weld parameters from one part size to another. Some simple hydrodynamic reasoning was also made in their work. Using experimental data, a melt film with a thickness of 464 μm was worked out. The authors then denied the existence of this layer by stating that no evidence of melting was detected from microstructural investigations. However, this view may not be true as is discussed in the later part of this dissertation [52].

2.2.2 Numerical models

In analytical models of friction welding, the thermal solutions are usually one-dimensional. The effects of thermal convection and radiation are usually not taken into consideration due to the difficulty in treating them analytically [57]. In addition, when the thermal properties of the materials are not taken as constants, but rather as variables changing with the temperature, the equation of thermal conduction become non-linear so that it is hard to get an analytical solution. Moreover, it is rather difficult to describe the geometric shape change analytically. Therefore, parallel with the analytical methods many researches have been carried out to analyse friction welding using numerical methods.

The first numerical model was put forward by Cheng [58]. In his pioneering work, he built a one dimensional model by finite difference method (FDM) to simulate the friction welding of an AISI 4140 alloy steel workpiece. This was an amazingly complex one when taking into account the inconvenience of using computers at that time. In this model, a melting layer was assumed to exist at the interface; its movement along the axial direction, *i.e.*, the effect of axial shortening, and the variation of thermal properties with temperatures were all taken into consideration in the thermal analysis. The calculated results were compared with experimental data and with the outcome of the analytical model from the heat balance integral method. Good agreement with measured value was claimed in his paper.

Wang and Nagapan studied the transient temperature distribution in inertia welding of AISI 1020 steel bars with a two-dimensional FDM model. The heat input at the interfaces was based on the characteristics of the rotational speed history and the total welding time obtained from experimental data. There was some discrepancy between the measured value and the predicted one. The authors stated that there are clear differences in temperature fields between the inertia and continuous drive friction welding. For welding the low carbon steel bars, the temperature reaches the peak value in a time as short as 0.06s with very steep temperature gradient for inertia welding, while in continuous drive friction welding, the temperature reaches the peak value at slower speeds, for example in 20 seconds. However, there was no clear explanation given for this difference. They also found that the total welding time plays an important role in determining the temperature distribution, which is consistent with general experience [38].

The friction welding of copper to steel bars were analysed by Sahin *et al* with a 2D FDM model. In the model the friction coefficient and thermal properties were all assumed constant. Their calculation results showed that the peak temperature is reached neither at the periphery nor at the centre of the bar [59].

In recently years, the adoption of the finite element method (FEM) has been increasingly reported in the investigation of friction welding. The first one to use the FEM approach is Sluzalec [60]. A thermo-mechanical FEM model was built to simulate the welding of mild steels; the temperature distributions and the shapes of the flash were predicted and compared with experimental results. There was good agreement between the measured temperatures and the predicted values in the early stage of friction welding. But the thermal results in the steady-state and cooling stages were not reported. The author also mentioned some irregularities of the flashes formed from the extrusion of materials; the failure to predict these flashes was attributed to specimen misalignment and non-uniform material properties. In this paper, the author also suggested that the limiting steady-state temperature in the joint cannot be higher than the temperature at which the yield point of the material is equal to the pressure used in the experiment, which sounds reasonable. However, it is proved wrong in the later part of this dissertation. The same author also made a

comparative thermal analysis study of the analytical and FEM solutions in friction welding. The paper reported good consistency among analytical, numerical and experimental results [61].

Moal and Massoni built a thermo-mechanical model for the simulation of the inertia welding of two similar parts. The material used in experiment was a nickel base superalloy (NK17CDAT); its material behaviour was described by an incompressible viscoplastic Norton-Hoff law in which the coefficients are temperature dependent, but no material data were provided in the paper. The torsional effects in friction welding were taken into account since the three components of the velocity fields were all computed in the model. An updated Lagrangian formulation together with remeshing techniques were used in the FEM model to trace the variation of the deformation zone. The formation of flashes, temperature and strain rate distribution were all illustrated graphically. The predicted axial shortening was found to be overestimated when compared with the measured one, which was attributed to the inaccurate parameters used in rheological and friction models [40].

Balasubramanian *et al* made a thermal analysis of continuous drive friction welding of AISI 1045 steel using the FEM software package ABAQUS [39]. To improve the accuracy of the FEM model, a formula for the friction coefficient taking into consideration the influence of temperature, axial load, and sliding speed were postulated, which was expressed in equation (2.3). A multiple linear regression analysis was used to determined the constants in equation (2.3) based on experimental data. This method of estimating the friction coefficient in friction welding was followed by some other workers in this field. However, for every material, a number of experiments are needed to obtain an equation like this, which means that there is almost no general applicability for this method.

Due to the difficulty in determining the value of friction coefficients, the researchers also proposed an energy balance method to circumvent this tricky problem in the study of the inertia welding of IN718 to IN718 [62]. Based on the principle of energy conservation, the authors assumed the kinetic energy of the flywheel was all converted into the friction heat at the interfaces. This heat source was then used as boundary condition in the FEM model. The temperature predictions were stated to be quantitatively and qualitatively sim-

ilar to the experimental data. A weakness however is that there is no mechanical analysis included in the FEM models.

Lee *et al* developed a special two dimensional (2D) axisymmetric element including the circumferential velocity to account for the strong torsional motion during inertia welding in the software package DEFORM [63]. Both the constant shear and Coulomb friction models can be used to describe the frictional behaviour of materials. Their model was validated with both the experimental data and analytical solutions. The development of this special 2D element in DEFORM provided great convenience for its users in modelling friction welding processes.

Similar to Lee's work, D'Alvise *et al* also wrote a special code in FORGE2 to simulate inertia welding process [41, 42]. They performed a thermo-mechanical analysis in friction welding of dissimilar materials. The method of determination of friction law was adapted from Moal's study [40]. The temperature, strain and residual stress fields were predicted. Some validation of the model in terms of upsets and flash profiles was made in their work.

Fu *et al* developed a thermo-mechanical model of inertia welding of 36CrNiMo4 steel tubes used in oil drillers with the DEFORM software package [51]. Their friction heat input model was the same as Wang and Nagappan's method [38]. An elastoplastic model was used to describe the material's constitutive relationship. The temperature, equivalent and residual stress, strain fields, and the flash shapes were predicted. The temperature fields from the calculations were in good agreement with values measured using an infrared detector. According to the calculations, the radial stress component becomes a tensile stress at the region between the deformed and undeformed zones owing to the formation of the flash. But no experiment was carried out to validate the results of the predicted stress, strain fields.

Wang *et al* made a thermo-mechanical analysis of inertia welding of RR1000 nickel-base superalloy tubes using the DEFORM package [64]. In their model, the need for an accurate frictional coefficient was circumvented by using an energy input method. The value of input energy was derived from measurements of torque, angular speed of the rotating part. The thermal history and residual stress predictions were validated by experimental

results from microstructure examinations and non-destructive residual stress measurement. However, torsional effects were not included in the model, so the results may be quite different from the real situation.

Unusually, Zhang *et al* made a 3D simulation of continuous drive friction welding of cylinders using DEFORM. However, the advantage of using a 3D model is not clear when compared with conventional 2D model [65].

More recently, Bennett and co-workers have made simulations of the inertia welding of dissimilar joints: IN718 to stainless steel AerMet100, with DEFORM [66]. In their model, the effect of the phase transformations occurring in the steel on the residual stress fields were emphasised.

Very occasionally, some authors have tried to simulate the material flow expected in steady-state friction welding with fluid mechanics models. Bendzsak *et al* presented an approximate model for the study of flow regimes within the friction welding of an aluminium alloy. The complex flow pattern was described by a numerical solution of the Navier-Stokes equations. Their results showed that a fraction of material returns to the viscoplastic zones, which has not been reported by other researchers [67]. Stokes and Poslinski analysed the effects of variable viscosity on the melting film during the steady stage of spinning welding of thermoplastics with a hydrodynamic model [68]. The simulations show that the thickness of the molten film and the melting rate are strongly influenced by the variable viscosity, and by the convection of colder material from the solid polymer into the molten film. The viscous heat generation and the pressure-induced flow also affect the behaviour of the molten layer. It seems that this interesting model possesses some potential to be extended to the analysis of friction welding of metals.

In spite of the research efforts listed above, little progress has been made to build completely satisfactory theoretical models. Most of the analytical models focus on the thermal aspects of friction welding, much less attention has been paid to the mechanical analysis. In particular, the prediction of total upset generated, which is in practice one of the most important parameters, has never been attempted by these models. The numerical methods especially FEM models can take more aspects into consideration and give a description of

processes in more detail. But there is still a lack of understanding, for example, the formation of burr, the material flow in contact zone, the torsional effects, *i.e.*, the friction-induced shear stress's influence. Moreover, the relative advantages/disadvantages of a simple analytical approach and one based upon the finite element method are unclear. The work reported here was carried out with these factors in mind.

2.3 Structure of the thesis

This thesis is divided into three parts:

In chapter 3, a thermal analytical model of inertia welding is presented. Some formulations and related assumptions are given and discussed. The thermal features of inertia welding are also presented based on the calculation results.

In chapter 4, mechanical analysis is presented. This chapter is composed of three parts. In the first part, a model based on the idea of finite difference method (FDM)is proposed to study the flow behaviour of material at the friction interfaces. In the second part, a new model from the viewpoint of fluid mechanics is given and discussed, aiming to explain the formation of the burr in process. In the third part, a variational method is employed to get a simple formula to describe the velocity fields in inertia welding. All of these three methods are used to predict the upset occurring during inertia welding.

In chapter 5, a FEM model is presented and some comparisons with analytical models are made. The sensitivity to process parameters is investigated.

Finally, some conclusions together with some suggestions for future work are made to complete this thesis.

Chapter 3

Thermal analysis

For the convenience of analysis, a model of inertia welding process is to be set up. In practice, the geometry of the part to be welded is important. Provided that there is radial symmetry, complicated shapes can be welded, but one common arrangement is that of a circular thin-walled tube – and this will be assumed in the present study. It will be assumed that two tubes of identical geometry are to be welded, of identical material, taken to be the superalloy Inconel 718. To simulate the welding process of this part and to simplify the thermal analysis, the effects of radiation and convection along the outer and inner surface of the tube will not be taken into consideration. This is expected to be approximately true if the welding process is finished in a short time. The length of the part is taken as semi-infinite since it is clamped rigidly at one end. Thus, a semi-infinite one-dimensional heat conduction model is used. To facilitate the mechanical analysis in the later part, a cylindrical coordinate system was set up to analyse the welding process. The coordinate x represents the axial direction, θ represents circular direction and r represents radial direction. The weld-line is located at the origin $x = 0$, at which a boundary condition of fixed temperature or flux was prescribed, as illustrated in Fig.3.1. Only one-half of the weld was modelled.

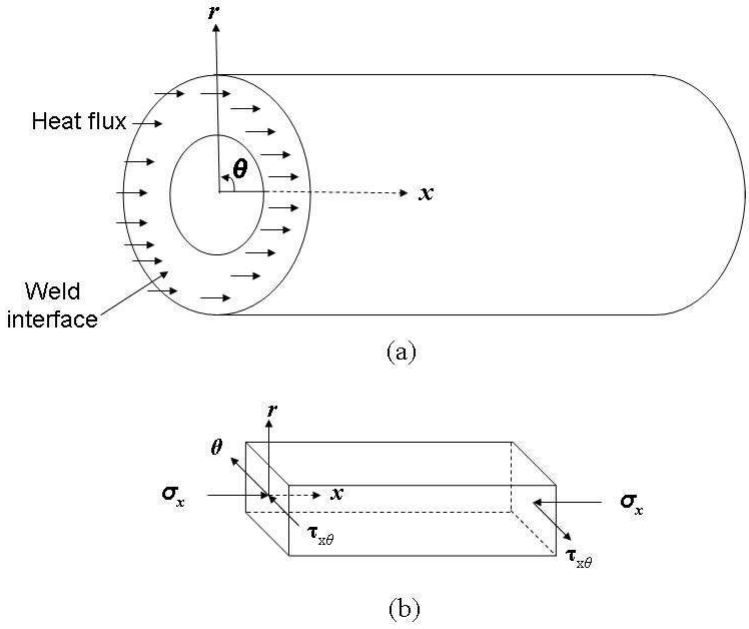

Figure 3.1: Thermo-mechanical model used in the calculations: (a) a round tube with thermal boundary conditions indicated (b) an element within it.

3.1 Equations for modelling of heat transfer

The one-dimensional heat equation to be solved is as follows [57],

$$\frac{\partial T}{\partial t} = \kappa \frac{\partial^2 T}{\partial x^2} \qquad 0 < x < \infty \tag{3.1}$$

where T, x, t are temperature, distance and time respectively. The term $\kappa = K/\rho c$ is the thermal diffusivity, where K, ρ , c are the thermal conductivity, density, heat capacity of the material respectively. The initial condition is taken as

$$T\{x, 0\} = f\{x\}, \qquad 0 \leq x < \infty \tag{3.2}$$

where $f\{x\}$ is the known function representing the initial condition, *i.e.*, the prescription of the temperature at every point in the body at the initial moment ($t = 0$). The boundary conditions used for calculation during the heating process are taken as follows

$$T\{0, t\} = g\{t\} \qquad t > 0 \tag{3.3}$$

for prescribed temperature at the boundary or

$$-K\frac{\partial T}{\partial x}\{0,t\} = q\{t\} \qquad t > 0 \tag{3.4}$$

for prescribed heat flux at the boundary. Here $g\{t\}$, the boundary temperature distribution, is an assumed known function of time, and $q\{t\}$ is the heat flux at the boundary.

Given what is known about the inertia welding process and consistent with the work of others [36], the temperature calculation is carried out in three distinct steps. During the first (heating) stage, the temperature at the weld line rises rapidly; to simplify the calculation, a constant heat flux $q\{t\}$ is used in this period. In the second stage, the surface temperature at the weld line $(x = 0)$ is assumed to be constant, which is a reasonable approximation due to the dynamic heat balance between heat generation and heat conduction at the weld line. Finally, during the cooling stage the heat flux at the surface is set to zero, consistent with a lack of heat generation at the plane of symmetry along the weld line.

The initial temperature for the parts to be welded is assumed a constant T_0. In the heating stage, T_0 is assumed to be 0°C, *i.e.*, f{x}=0. This simplifies the calculation and makes little difference to the results. The initial temperature for the 2nd stage is taken to be that at the end of the heating stage. The formula for the heating stage is [57] [69]

$$T\{x,t\} = T_0 + \frac{q}{K}\left(2\sqrt{\frac{\kappa t}{\pi}}\exp\left\{\frac{-x^2}{4\kappa t}\right\} - x\text{erfc}\left\{\frac{x}{\sqrt{4\kappa t}}\right\}\right) \tag{3.5}$$

where q is the heat flux, K is the thermal conductivity, t, x refer to time and axial coordinate respectively, and κ is the thermal diffusivity. The term erfc$\{x\}$ is the complementary error function, it is defined as

$$\text{erfc}\{x\} = \frac{2}{\sqrt{\pi}}\int_x^\infty \exp\{-\eta^2\}d\eta \tag{3.6}$$

For the second stage, one takes [57]

$$T\{x,t\} = \frac{1}{2\sqrt{\pi\kappa t}}\int_0^\infty f\{\xi\}\left[\exp\left\{\frac{-(x-\xi)^2}{4\kappa t}\right\} - \exp\left\{\frac{-(x+\xi)^2}{4\kappa t}\right\}\right]d\xi + \frac{x}{2\sqrt{\pi\kappa}}\int_0^t \frac{g\{\tau\}}{(t-\tau)^{3/2}}\exp\left\{\frac{-x^2}{4\kappa(t-\tau)}\right\}d\tau \tag{3.7}$$

where $f\{\xi\}$ refers to the initial temperature profile when the 2nd stage starts, $g\{\tau\}$ is the prescribed temperature at the weld line, taken to be constant in this case, and numerically

equal to the melting temperature of the alloy. The formula for cooling stage is taken to be [57]

$$T\{x,t\} = \frac{1}{2\sqrt{\pi\kappa t}} \int_0^\infty f\{\xi\} \left[\exp\left\{ \frac{-(x-\xi)^2}{4\kappa t} \right\} + \exp\left\{ \frac{-(x+\xi)^2}{4\kappa t} \right\} \right] d\xi \qquad (3.8)$$

where $f\{\xi\}$ refers to the initial temperature profile when cooling starts.

The above expressions have been found to allow a reasonable approximation for the thermal cycles due to inertia welding to be made. Temperature-averaged material properties are adopted in calculation, and these are summarised in Table 3.1.

Table 3.1: Parameters and boundary conditions used for the thermal analysis[17].

Parameters	Heating Stage	Steady Stage	Cooling Stage
κ (mm^2/s)	4.09	4.09	4.09
K (W/mm/k)	0.017	0.017	0.017
Prescribed temperature		1260°C	
Prescribed heat flux	5 W/mm^2		0

3.2 Thermal results and discussion

3.2.1 Temperature profiles at different stages

Fig.3.2 illustrates the temperature profile in the workpiece during the heating stage, assuming a heat flux of 5W/mm^2; this is a reasonable figure for this first part of the process. For this flux, one can see that a temperature of 1260°C (the melting temperature of IN718) is reached in about 3.5 seconds. After 5 seconds, it reaches a temperature of 1500°C, which is far beyond the melting point and therefore physically unrealistic since it is widely accepted that no gross melting occurs during the process. Hence, after the melting point is reached (*i.e.* at $t = 3.5$ seconds for a flux of 5W/mm^2) one prescribes instead a fixed temperature, which is taken to be the melting temperature of 1260°C. Fig.3.3 illustrates the temperature distribution during the 2nd stage. One can see that the temperature gradient decreases gradually with an increase in the holding time. When the relative motion at the joint ceases,

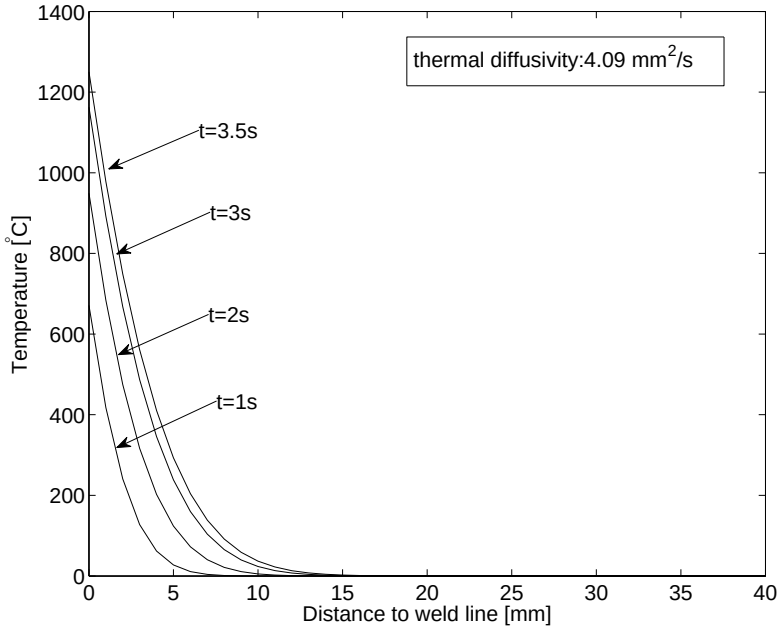

Figure 3.2: Temperature profile during the heating stage (q=5W/mm^2).

heat no is longer generated there and the third cooling stage begins. Fig.3.4 illustrates the temperature distribution made at various times thereafter.

The thermal histories of regions close to the weld-line is of interest, since these will control the microstructure and properties exhibited, see Fig.3.5. In this graph, the heat flux is again taken to be 5W/mm^2 for the heating stage; after 3.5s the welding interface is kept at 1260°C for 30 seconds, and cooling follows. One can see that the region near the welding interface, for example, at the point x=3mm, reaches the highest temperature at the end of the heating stage, *i.e.*, t=33.5s, while for the region further from the weld line, for example at the points x=6mm and x=9mm, the highest temperature appears during the cooling stage. This is because of the heat transferred from the zone near the weld line with the higher temperature. In the Fig.3.5, we can find that the highest temperature of the curve represents the temperature history of the point which is 11mm away from the mating surfaces is 653°C, which is reached at the time of 38.5s, 5 seconds after the start of the cooling stage. The microstructure of IN718 is altered when exposed to a temperature higher than 650°C. Thus if we define that the heat-affected zone for IN718 as the part with its temperature above 650°C during welding, the width of the heat-affected zone is

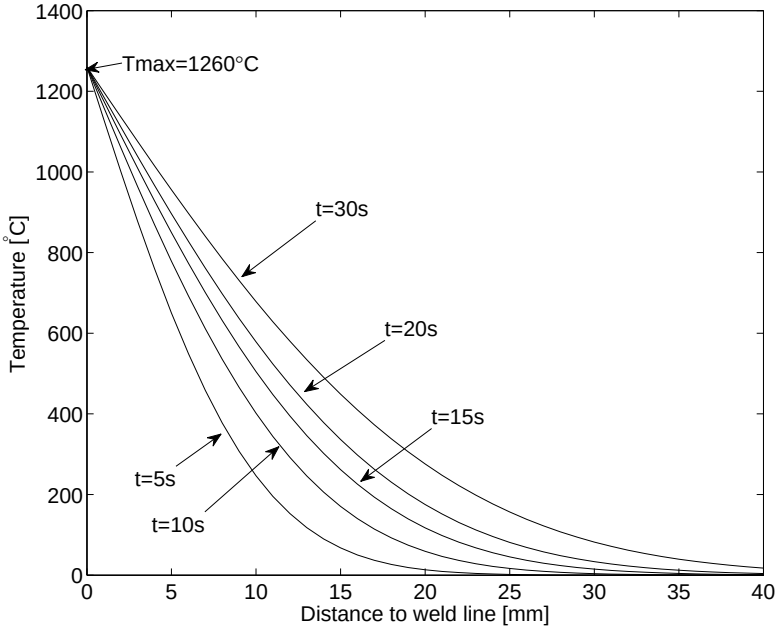

Figure 3.3: Temperature profiles during steady-state stage.

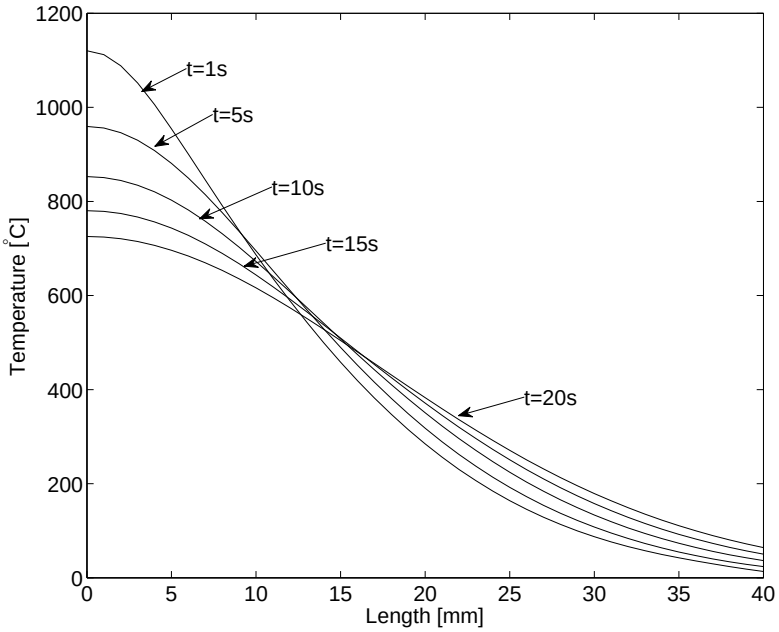

Figure 3.4: Temperature profiles during the cooling stage.

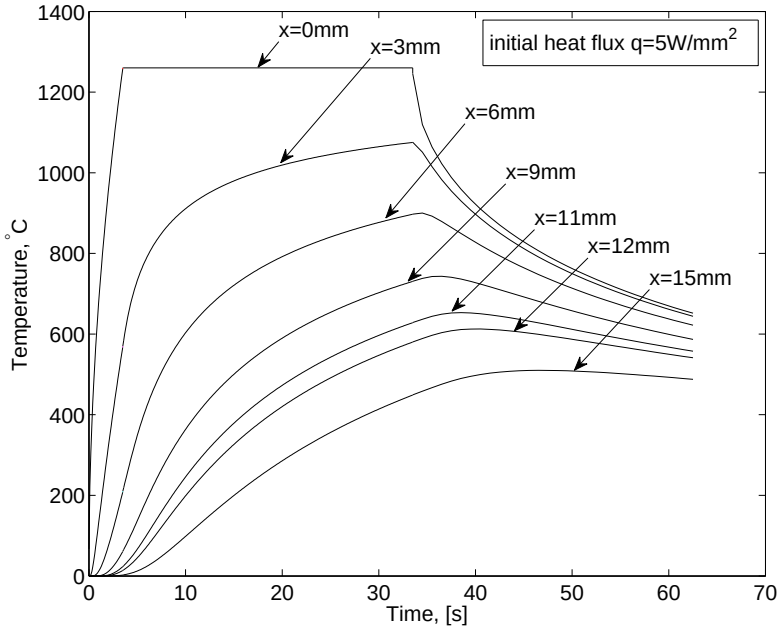

Figure 3.5: Predicted thermal history at different points away from the weld interface.

predicted to be about 11mm for these conditions.

3.2.2 Heat flux study

It is important to consider how the magnitude of the heat flux influences the time taken for the melting temperature to be reached. From equation (3.5), the temperature at the weld line during heating stage is as follows

$$T = \frac{2q}{K}\sqrt{\frac{\kappa t}{\pi}} \tag{3.9}$$

where the symbols have the same meaning as those in equation(3.5). If the highest temperature reached in inertia welding is defined as T_{max}, from equation (3.9), the relationship between heat flux value q and time(t_h) needed for temperature at the welding interface to reach T_{max} is given by

$$t_h = \frac{T_{max}^2 K^2 \pi}{4\kappa q^2} = \frac{C}{q^2} \tag{3.10}$$

where $C = (T_{max}^2 K^2 \pi)/(4\kappa)$ can be taken as a constant. Equation (3.10) indicates that the heating time t_h is inversely proportional to the square of heat flux q. If T_{max} is assumed to be 1260°C, the relationship between t_h and q for IN718 is as given in Fig.3.6.

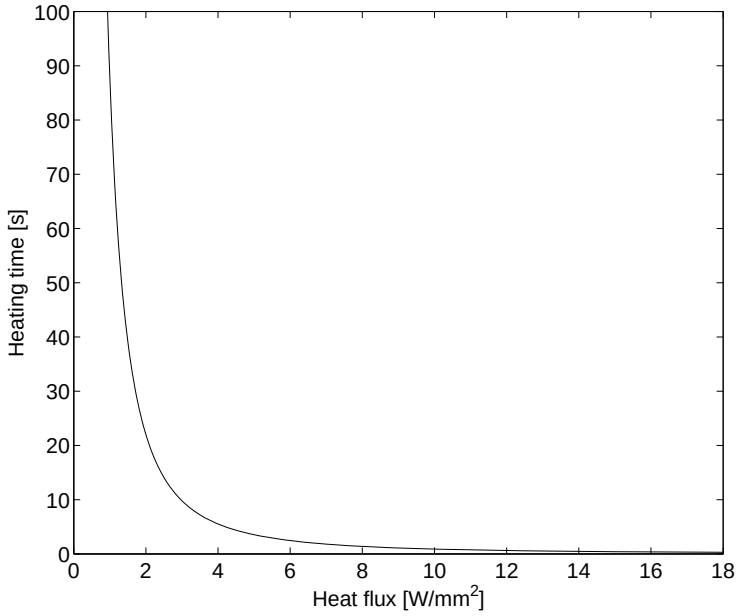

Figure 3.6: Relationship between heating time (t_h) and heat flux q for IN718.

In practice, different heat fluxes can be encountered due to different parameters used, *e.g.*, axial load, rotation speed. Here, the effect of altering the value of the heat flux has been studied with the assumption that the highest temperature reached remains unchanged, at 1260°C. The relationship between the heat flux q and the temperature profile $T\{x,t\}$ is as follows

$$q\{t\} = -K\frac{\partial T\{x,t\}}{\partial x} \tag{3.11}$$

Finally, one can determine the heat flux needed at the interface ($x = 0$) to maintain a value equivalent to the melting temperature during the second stage of the process. The results are shown in Fig.3.7, in which the effective heat fluxes for the complete process are given. In the calculations, the total time span for the first two stages was assumed to be the same, at 30 seconds. It is found that the time for the heating stage varies considerably depending upon the initial value of the heat flux. When the temperature reaches the highest point, the effective heat flux curve drops quickly. As time goes by, the effective heat flux curves for different processes gradually coincide, which means that the temperature profiles are gradually becoming coincident as the time in the steady stage increases.

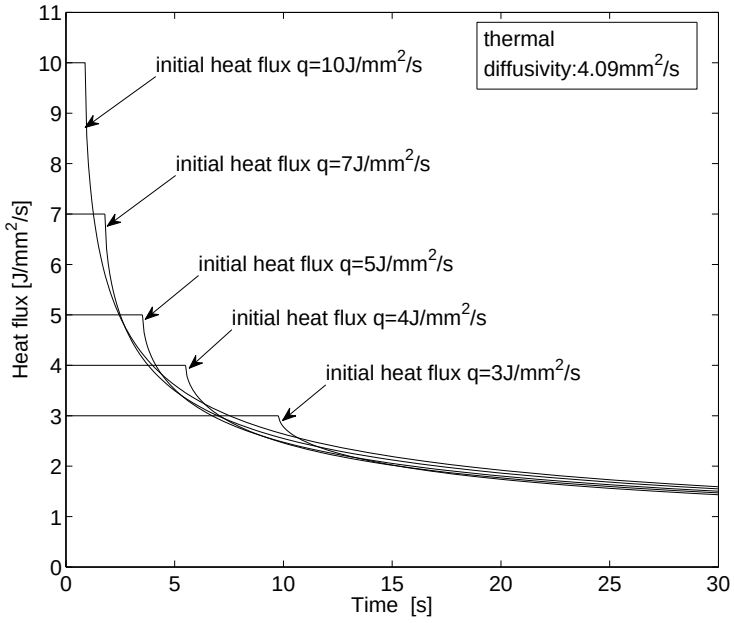

Figure 3.7: The effective heat fluxes for the whole welding process.

3.2.3 Peak temperature distribution

The distribution of peak temperatures is important since this will influence microstructural changes markedly. Various initial heat fluxes were studied. The results confirm that the profiles for peak temperature distribution change little if the holding time for the steady stage is long enough. For example, in Fig.3.8, the total time for the first two stages is 30 seconds, and the curves representing peak temperature distribution along the rod are nearly the same. When the initial heat flux is kept constant, for example 5W/mm^2, and the holding time for steady stage varies, the corresponding peak temperature curves are quite different. In Fig.3.9, the peak temperature distribution curves under different holding times, from 5 seconds to 30 seconds, are presented. The highest temperature at the weld line is assumed to be 1260°C. If we define the heat affected zone (HAZ) as temperature above 650°C for IN718, then the width of the HAZ after holding for 5 seconds is about 5.3mm, while holding for 30 seconds, the width of the HAZ is 11mm. So compared with the initial heat flux, the peak temperature distribution is more sensitive to the holding time during the steady stage.

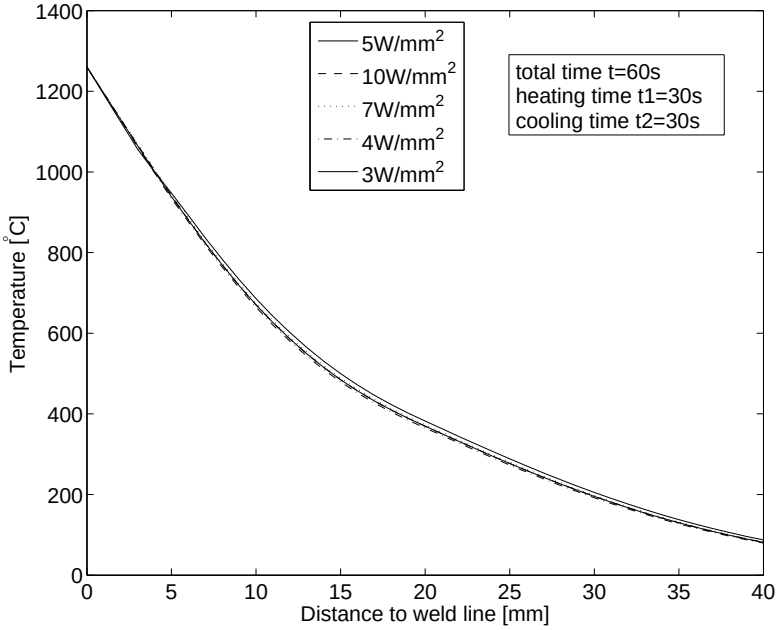

Figure 3.8: The peak temperature curves for various initial heat fluxes.

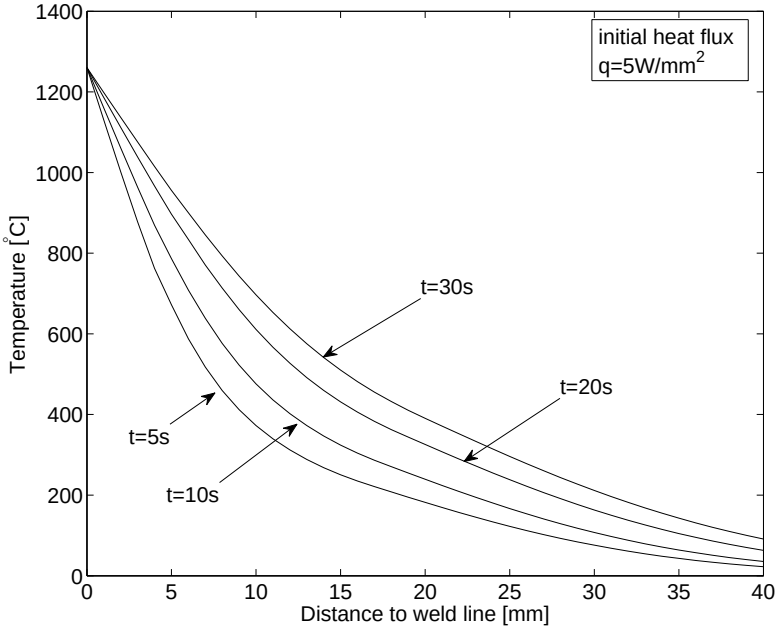

Figure 3.9: The peak temperature curves for various holding times during the steady-stage.

3.2.4 Formulae for analytical solution of heat equation

In Milding and Grong's paper [36], formulae for each of the three stages in friction welding were presented. The formula for 1st stage is actually the same as formula (3.5) from this paper, with the exception that the initial temperature has been assumed to be zero in this study. The formula for the 2nd stage is as follows

$$T\{x,t\} = T_{max}\text{erfc}\left\{\frac{x}{\sqrt{4\kappa t}}\right\} \tag{3.12}$$

and for the 3rd (cooling) stage

$$T\{x,t\} = \frac{2q\sqrt{t_h/t_s}}{K}\left\{\left[\sqrt{\frac{\kappa t}{\pi}}\exp\left\{-\frac{x^2}{4\kappa t}\right\} - \frac{x}{2}\text{erfc}\left\{\frac{x}{\sqrt{4\kappa t}}\right\}\right] - \left[\sqrt{\frac{\kappa(t-t_s)}{\pi}}\exp\left\{-\frac{x^2}{4\kappa(t-t_s)}\right\} - \frac{x}{2}\text{erfc}\left\{\frac{x}{\sqrt{4\kappa(t-t_s)}}\right\}\right]\right\} \tag{3.13}$$

where t_h and t_s denote the time from the start of weld to the end of heating stage and to the end of the steady stage respectively. The accuracy of formula (3.12) appears to be satisfactory, so it has been accepted here. In fact, it is the exact solution if the initial temperature for the 2nd stage is zero. As time proceeds, the influence of the initial temperature distribution becomes weaker and weaker, and consequently formula (3.12) becomes a better estimate. So formula (3.12) may still be used as a good approximation in thermal analysis. However, in this formula, the heat flux at the beginning is infinity, which is obviously not true in practice. To improve the accuracy of formula (3.12), it may be re-written as follows

$$T\{x,t\} = T_{max}\text{erfc}\left\{\frac{x}{\sqrt{4\kappa(t+t_0)}}\right\} \tag{3.14}$$

where t_0 denotes the time for the heat flux to drop from infinity to the initial heat flux q.

As for the accuracy of formula (3.13), it seems that it is not as satisfactory at the beginning of the cooling stage. In Fig.3.10, the solid lines represent the model presented in this paper. The dashed lines are results from formula (3.13). All the curves are cooling curves for 1 second after maintaining the steady stage for 20s and 30s respectively. The highest temperature at the steady stage is also assumed to be 1260°C. From the graph, we can see that the shapes of the curves are similar, but there are about 60 degrees gap between corresponding curves for the temperature near weld line. Since both methods predict a rapid

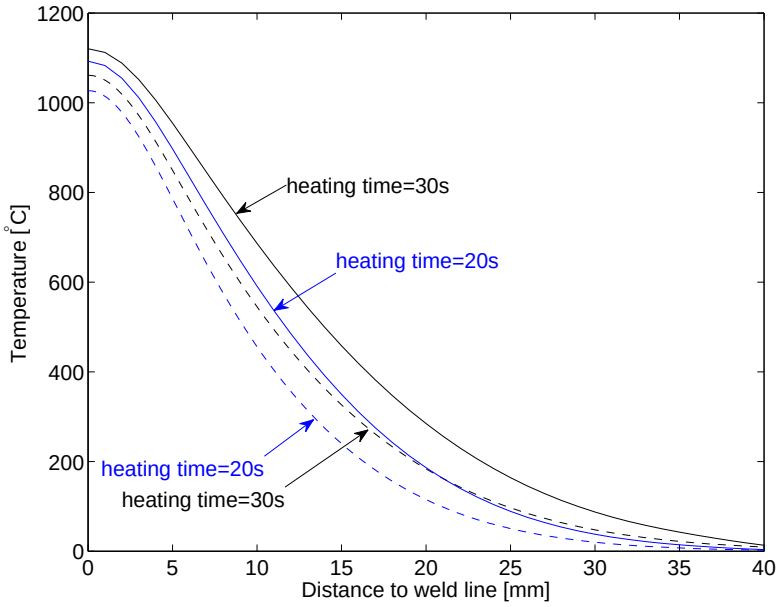

Figure 3.10: Comparison between Mildings formula and numerical method, solid and dashed lines represent results from this paper and Milding's [36], respectively.

drop of temperature in the welding interface, there is very little plastic strain because of the significant increase of yielding strength of welding material. So formula (3.13) can still be used in predicting upset value.

3.2.5 Discussion

In this simulation, the initial heat flux for friction welding is assumed to be 5W/mm^2. As a result, the weld line reaches the peak temperature in 3.5 seconds. This appears reasonable since it is generally believed that the highest temperature of the mating interfaces is reached during inertia welding in a short time. Wang and Nagappan claimed that the temperature of the weld line reaches its peak value in 0.2s during inertia welding [38]. Soucail *et al* also stated that a temperature of 1280°C is reached in less than 1 second during inertia welding of astroloy [49]. Wang *et al* studied the influence of three groups of parameters in inertia welding of RR1000. Their results showed that the highest temperature is reached in 2.2s, 3.8s, 4.8s separately, depending on the setup of the welding conditions [64]. Even though there is some difference in the reports about the time to reach the peak temperature due

to various experimental conditions, it seems acceptable to set aside several seconds for the heating stage. So the heat flux assumed in this study may be a good approximation to the real situation.

Another assumption in the thermal analysis is to set 1260°C as the highest temperature in inertia welding of IN718. This is because the author believes that the highest temperature experienced during friction welding is very close to the melting temperature of welding material even though the existence of the molten material is contentious. There are also some uncertainty about the solidus point for IN718. Usually the recommended value for it is 1260°C [17, 70]. However, some authors have reported lower values. Antonsson and Fredriksson stated the solidus of IN718 varies from 1230°C to 1250°C after performing differential thermal analysis (DTA) experiments [71]. Lewandowski and Overfelt even reported a value as low as 1150°C [72]. The results from the software Thermocalc predict a value of 1210°C. The slight difference in chemical composition and experimental conditions such as heating and cooling rates may account for these discrepancies. Nevertheless, the average of the reported value tends to be lower than 1260°C. If that is true, there is a small fraction of liquid during inertia welding of IN718 under the temperature of 1260°C. This presence of the small fraction of liquid can lead to a good lubrication effect during friction process, which provides a good explanation for the low friction coefficients during the steady state stage of friction. In fact, the friction coefficient can be as low as 0.02 [50], which is equivalent to a metal plate slipping on an icy surface. The friction coefficients applicable to metal-metal contact are usually much higher, so it is very possible to have some liquid acting as lubricant on this occasion during friction welding [73]. So the assumption of a temperature of 1260°C in this study may be very close to the real situation. This value can also get some support from Zhang *et al*'s work [74]. They made an investigation of inertia welding of GH4169, an alloy with very close chemical composition to IN718 [75]. In their paper, a highest temperature of 1250°C was reported.

3.3 Summary

In this chapter, a one dimensional thermal analysis of inertia welding was performed. The whole process was divided into three stages: the heating stage, steady-state stage and cooling stage. The corresponding formulae for their temperature distributions were given separately. Some typical temperature fields in welding were presented. The thermal history study showed that the metal near the border of the HAZ undergoes the highest temperature exposure during the cooling stage due to the heat transferred from the material near the weld line. The holding time during the steady-state stage greatly affects the peak temperature distribution while the initial heat flux has little influence on it. The highest temperature in inertia welding of IN718 was assumed to be 1260°C, which should be a good representation of real cases in practice.

Chapter 4

Mechanical Analysis

4.1 A typical model of inertia welding for analysis

In this study, one aim for the mechanical model is to predict the value of axial shortening analytically. Thus a proper coordinate system has to be set up for the analysis. Since the object chosen for analysis is a circular thin-walled tube, a cylindrical coordinate system illustrated in Fig.3.1 is a natural choice. Thus the compression stress along the axial direction from the load is labelled as σ_x, the shear stress induced from friction is labelled as $\sigma_{x\theta}$, or $\tau_{x\theta}$ as shown in Fig.3.1. To simplify the analysis, the axial shortening during the heating stage is neglected. This should still be acceptable because the upset for the heating stage is very small compared with that for the steady state stage due to the short heating time in the heating stage.

It is necessary to identify the key process variables (KPVs) which can be measured; these can be regarded as inputs to the process model. In the inertia welding process, the axial load P_L, the initial angular rotating speed ω and the moment of inertia of the flywheel/rotating part I may be regarded as the KPVs. Typically, the variation of ω with time t during the process, the deceleration curve, is recorded during welding; this allows the friction-induced torque T to be determined by first estimating the instantaneous value of the angular deceleration $a\{t\}$ according to

$$a\{t\} = \frac{\partial \omega\{t\}}{\partial t} \tag{4.1}$$

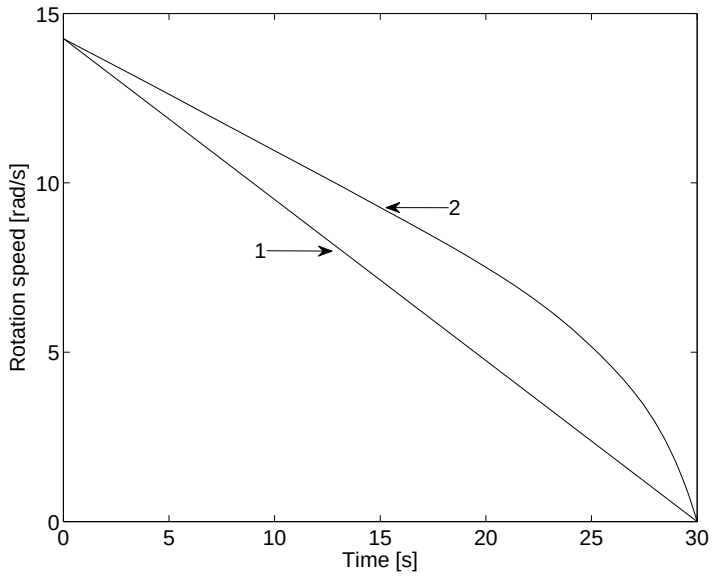

Figure 4.1: Typical variation of angular speed with time during inertia welding process.

and multiplying by the moment of inertia, denoted I, such that

$$T\{t\} = I \times a\{t\} \tag{4.2}$$

Note that the instantaneous value of the angular deceleration can be estimated by an appropriate finite difference expression, provided that the functional form of $\omega\{t\}$ is known. Then, the friction-induced shear stress τ can be estimated by balancing it against the measured torque, according to

$$\tau\{t\} = \frac{T\{t\}}{r_n A} \tag{4.3}$$

where r_n and A refer to the average value of the outer and inner radii, and the mating area of the weld being formed, respectively. Assuming the axial load P_L to be constant during the process, the nominal friction coefficient μ_0 in the welding interface can then be determined from the ratio of $\sigma_{x\theta}$, the shear stress developed from friction, and the axial compression stress P_L/A.

It is helpful to insert approximate values into the expressions, in order to fix ideas. It is usual for an axial stress of several hundred MPa to be applied, with an initial angular speed of a few hundred revolutions/minute, and the initial total kinetic energy of the flywheel to be several million joules. After a study of experimental data [50], these values are taken to

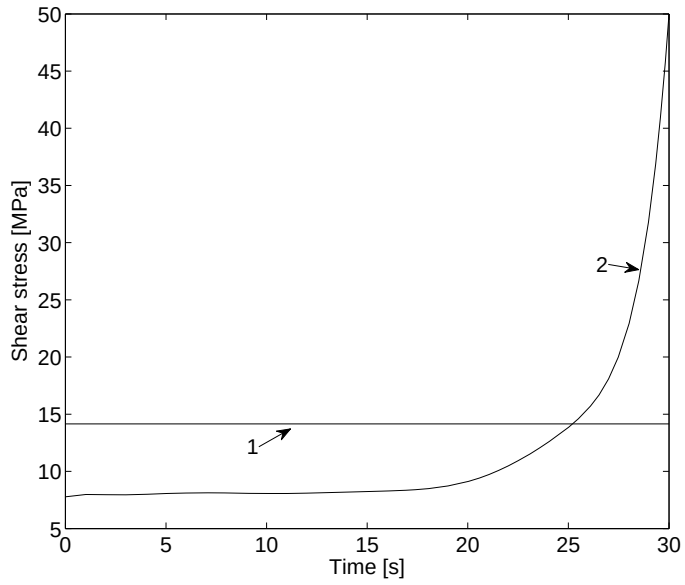

Figure 4.2: Variation of shear stress with time, corresponding to the curves given in Figure4.1.

be 250MPa, 135 RPM and 3×10^6J respectively at the start of the steady state stage, with an average friction stress of 14 MPa acting on a mating area of 10000mm^2, the average radius of the tube is assumed 100mm; moreover, to a first approximation, the angular speed ω is expected to decrease linearly with time, consistent with constant energy dissipation at the mating surfaces, thus the time of welding can be estimated to be around 30 seconds. In practice, the angular speed is found not to decrease linearly with time; instead it decreases rather more slowly initially, with a rather sharp decrease as the weld is finally created, see the curve 2 in Fig.4.1. The corresponding shear stress curves are illustrated in Fig.4.2; estimates of the way in which the interfacial friction coefficient varies with time μ_0 would follow, as before. We can see the shear stress is small during the majority of the forming stage, typically with a value of less than 10MPa, which is consistent with the experimental data [50]. Note the sharp increase in the shear stress and the very end of the rotation, which arises due to the significant rate of change of ω with time at that point. These considerations emphasise the importance of an accurate measurement of $\omega\,\{t\}$ throughout the process.

In this study, a model is proposed which takes account of the influence of the shear stress

$\sigma_{x\theta}$ developed due to frictional effects; as shown in Fig.4.2, this can become significant at the very last stage of welding and therefore needs to be accounted for. To simplify the calculation, the shear stress in each section of the tube perpendicular to the axial direction is assumed to be homogeneous at each moment, due to the balance of the torque. The shear stress is also assumed not to change with the different temperatures assumed in the welding interface. The shear stress used in the calculation is from curve 2 in Fig.4.2.

4.2 Constitutive equation used – lambda model

To calculate the displacement of the weld line, it is necessary to propose a constitutive relationship for the material during hot deformation. In the literature, many constitutive equations are available to describe the hot deformation behaviour of IN718 [76, 77, 78, 79, 80]. In fact, the constitutive equations are not always consistent with each other, probably due to differences in composition, processing method and microstructure. Here, the lambda model proposed by Blackwell, Brooks and Bate is implemented [81], in which a microstructure-related internal variable λ is used together with the Zener-Hollomon parameter. Compared with other models, for example those proposed by Lin [82] and Zhao [78], the lambda model does not have a significant number of parameters and is relatively easy to implement. In fact, the formulae in paper [81] can be summarised succinctly as follows

$$Y = k_1 Z^m (\lambda^n - \exp\{-\beta\epsilon_e\}) \tag{4.4}$$

where Z is the Zener-Hollomon parameter, m, n and β are material constants, Y, ϵ_e are the flow stress and effective strain respectively, and k_1 is a scaling constant. The term λ is the microstructure-related state variable parameter, which is set to an initial value of unity but which is allowed to evolve consistently with

$$\lambda = \lambda_0 Z^{q_0} + (1 - \lambda_0 Z^{q_0}))\exp\{-\alpha\epsilon_e\} \tag{4.5}$$

where λ_0, q_0 and α are all material related constants. The Zener-Hollomon parameter used is defined according to

$$Z = \dot{\epsilon_e}\exp\{Q/RT\} \tag{4.6}$$

Table 4.1: Parameters used in the lambda model [83].

Alloy	k_1	λ_0	n	m	q_0	α	β	Q/R
IN718	5.369×10^{-3}	7.576	2.877	0.2522	-5.4354×10^{-2}	2.487	18.78	59407

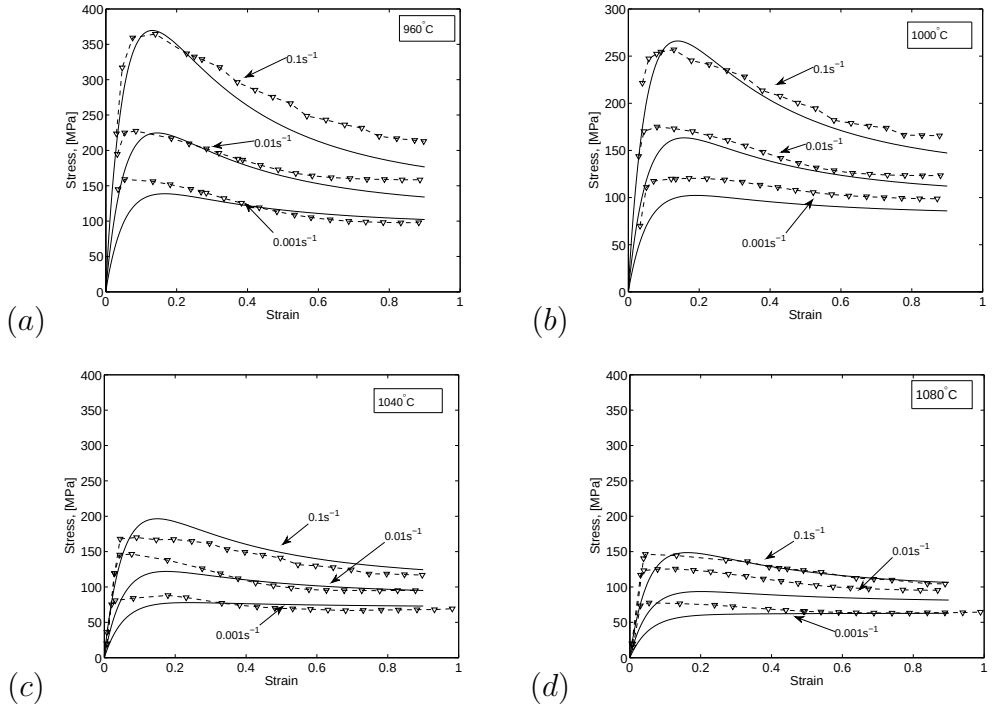

Figure 4.3: The stress-strain curves for IN718, the solid lines represent results predicted by the lambda model, dashed lines represent experimental data [83] at (a) 960°C (b) 1000°C (c) 1040°C (d) 1080°C.

where $\dot{\epsilon_e}$ is the effective strain rate, Q is an activation energy, R is the gas constant.

The parameters used in the lambda model to describe IN718's stress-strain relationship are summarised in Table 4.1. These parameters come from the work done by Prof.Jeff Brooks in University of Strathclyde [83]. Fig.4.3 illustrates some of the stress-strain relationships which then arise. The predicted results are consistent with the experimental datas. The value for λ varies between 0 and 1, within the ranges of the temperature and strain rate used in this simulation. As illustrated in Fig.4.4, it can be shown lambda scales inversely with the flow stress, so that it is an internal variable which is related to the extent to which the microstructure resists hardening during hot deformation [81].

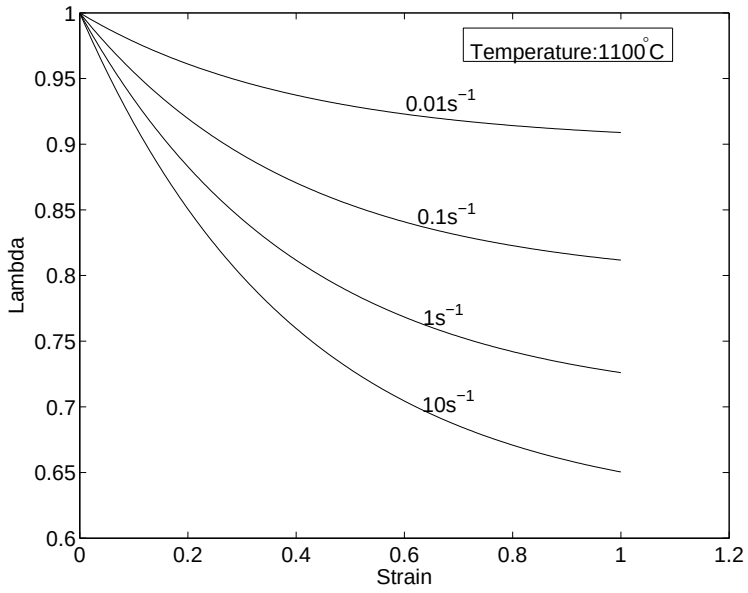

Figure 4.4: Variation of lambda with strain under various strain rate conditions.

4.3 Round tube model

4.3.1 Simple thin-walled tube model

In this study, the mechanical part of the problem is first reduced to that of a tube under combined loading of the axial compressive stress and the shear stress arising from frictional effects. To analyze it, a cylindrical coordinate system is chosen, as illustrated in Fig.3.1. The axial direction is labelled as x and the radial as r; the tangential direction θ. To simplify the analysis, a simple thin-walled tube is modelled. This may be reasonable when the radius of tube is far larger than the wall thickness of the tube. Due to the thin wall thickness, the radial and circular normal stress component σ_r, σ_θ and shear stress component σ_{xr} are all considered small and omitted. Since the parts after welding are still axisymmetrical, the shear stress component $\sigma_{r\theta}$ is also zero. So the stress components remaining for analysis are the compressive stress along the axial direction denoted as σ_x and the shear stress component $\sigma_{x\theta}$ induced by friction. Hence the effective stress σ_e arising during inertia friction welding can be approximated as

$$\sigma_e = \sqrt{{\sigma_x}^2 + 3{\sigma_{x\theta}}^2} \tag{4.7}$$

Due to the deformation occurring at high temperatures, the elastic portion of the strain will be small compared with the plastic strain; therefore it has been omitted from the calculation. Hence, the Levy-Mises flow rule has been adopted as follows [84]

$$\dot{\epsilon_{ij}} = S_{ij}\dot{\eta} \tag{4.8}$$

where $\dot{\epsilon_{ij}}$ is the plastic strain rate tensor and S_{ij} is the deviatoric stress tensor. For this thin-tube model, S_x equals $\frac{2}{3}\sigma_x$ and $\dot{\eta}$ is determined from

$$\dot{\eta} = \frac{3\dot{\epsilon_e}}{2\sigma_e} \tag{4.9}$$

where $\dot{\epsilon_e}$ is the effective plastic strain rate.

As mentioned before, there is a steep temperature gradient near the weld line during inertia welding. The temperature rise of the region in the rod will be very small if its distance to the weld line is big enough. There is no plastic deformation at this region because

of much higher yield stress at the room temperature. Thus, although the length of the rod in the mechanical model is the same as the one in thermal analysis, semi-infinite, so that the temperatures got from thermal analysis can be used directly in mechanical analysis, the length of tube actually used for calculation is set to be finite, l, in the mechanical model. This will have no influence to the final mechanical results if l is big enough. In this study, l is set to be 70mm. In the simulation, the length of the tube along the x direction is partitioned into n subintervals of equal length $\Delta x = l/n$. The Δx is set to be 0.05mm. When the length of each subinterval is small enough, the temperature within each subinterval can be taken as constant over length at each time step, without loss of accuracy. For each subinterval, the compression strain rate along axial direction, *i.e.*, x direction, is calculated according to

$$\dot{\epsilon_x} = \frac{\bar{\sigma}_x \dot{\epsilon_e}}{\sigma_e} \tag{4.10}$$

where $\bar{\sigma}_x$ is the nominal axial compression stress. If the temperature field is available and the effective strain rate $\dot{\epsilon_e}$ is known through the constitutive equation, the compression strain can be integrated along the length of the rod during the whole 2nd stage, and the displacement of the weld line (upset) can then be calculated when coupling with the thermal results.

In the calculation, the temperature fields got from the thermal analysis were used directly in the mechanical analysis. Thus the welding interface temperature is assumed constant during the flash forming stage, which simplifies the analysis. This assumption means that there is a dynamic thermal equilibrium at the weld line; the heat loss, which is caused by the convection, radiation on the surfaces of the tubes, and the heat taken away by the material in the form of flashes, equals the heat generated by the friction. This may roughly be true during the early seconds of the flash forming stage. However, the temperature at the rubbing interfaces may drop quickly during the last seconds of the rotation when the material of flashes flows out quickly, carrying away large amount of heat.

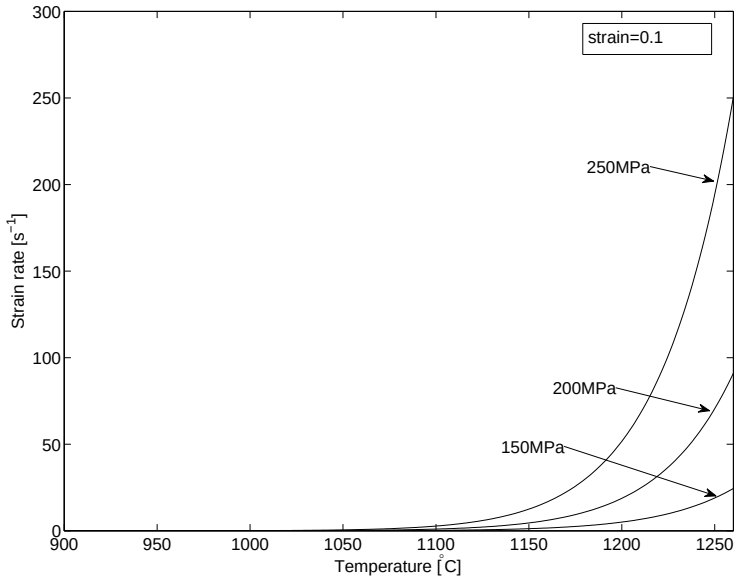

Figure 4.5: Variations of strain rates under different temperatures and pressures.

4.3.2 Modification of simple thin-walled tube model–Round tube model

With the simple thin-wall tube model and constitutive equation presented above, the upsets expected during inertia welding can be estimated. However, the author found that when this is done the predicted values of the upset are very much substantially greater than are realistic. The cause for this can be explained as follows. During welding, the temperature of welding interface is assumed to be high, near the melting point of welding metal. At this temperature, the material is very soft while the compression stress of inertia welding is normally in the range of several hundred MPa, so the welding metal at the weld line will have a very high strain rate under the action of the applied axial pressure. The strain rates of IN718 under different temperature and pressures are shown in Fig.4.5. The initial strain of the material in this graph is set to be 0.1. We can see that the strain rate of IN718 at a temperature of 1260°C under the compression pressure of 250MPa can be as high as 250s^{-1}. That means the soft metal at the welding interface will be expelled out very quickly during welding process, which is not what actually happens in practice. This result seems to be consistent with the view of many researchers that the temperature at the mating surface cannot be too high, and that it cannot reach the melting temperature, otherwise the

metal near mating surfaces will be squeezed out quickly due to the very low flow stress of metal at that temperature. Sluzalec even held that the limiting steady state temperature in the joint cannot be higher than the temperature at which the yield point of the material is equal to the pressure used in the experiment [60]. However, if Sluzalec's claim is correct, the friction stress during steady state stage would never be low enough to be in the range of 10MPa since the friction stress is equal to the shear strength of the metal at the welding interfaces during the steady state stage of friction welding, which should also be in the range of several hundred MPa. To solve this difficulty, the model was modified accordingly. From the results of the thermal analysis, we know that there lies a steep temperature gradient along axial direction near the mating interfaces. The temperature gradient near weld line can be as high as 100-200°C/mm. That means that only one or two millimetres away from the welding line, the temperature drops greatly and the metal there becomes much harder, which impedes the rapid flow of softer metal in the weld line due to the need for strain compatibility. This hydrostatic stress plays a significant role in this. Thus, for the soft material near the weld line, the high compression pressure acted on it by the load is to a large extent balanced by the hydrostatic stress exerted by the much harder material nearby holding it. It is not the nominal compression stress, but the corresponding deviatoric stress components which cause plastic deformation. Thus we see that the stress state in the simple thin-walled tube model is oversimplified. The stress state of metal near the weld line cannot be represented by a single compression stress from the external load. It becomes more complex due to the large plastic deformation there. To get a better description of the mechanical behaviour of the material near weld line, a comprehensive study of stress state near the weld line is required.

Usually the stress state near a weld line is complicated and difficult to analyse. Thankfully, the stress state in this case can be treated analytically. Since the object in the present study is a circular tube, we can assume general velocity fields to describe its plastic defor-

mation under the cylindrical coordinate system shown in Fig.3.1, as follows [85]

$$\begin{cases} u_r = \frac{1}{2}\left(r - \frac{r_n^2}{r}\right)\phi'(x) \\ u_\theta = u_\theta(t) = \omega(t) r \\ u_x = -\phi(x) \end{cases} \tag{4.11}$$

where u_r, u_θ and u_x are the velocity components in the radial (r), circumferential (θ) and axial (x) directions respectively. The neutral radius is r_n, the average of the inner and outer radius. The term $\phi(x)$ is an arbitrary function used to describe the velocity field in the axial direction, $\phi'(x)$ is the first order derivative of $\phi(x)$ with respect to x. It can be demonstrated that the velocity fields assumed satisfy the principle of volume conservation automatically. To simplify the analysis, we assume the origin of the coordinate system moves with the weld line during the process. So we have

$$\phi(0) = 0 \tag{4.12}$$

In the inertia welding of tubes, we can assume that there is no velocity gradient in the circumferential (tangential) direction. Then the components of the strain rate in cylindrical coordinates can be written [86]

$$\dot{\epsilon_{ij}} = \begin{Bmatrix} \dot{\epsilon}_r \\ \dot{\epsilon}_\theta \\ \dot{\epsilon}_x \\ \dot{\epsilon}_{rx} \\ \dot{\epsilon}_{r\theta} \\ \dot{\epsilon}_{x\theta} \end{Bmatrix} = \begin{Bmatrix} \frac{\partial u_r}{\partial r} \\ \frac{1}{r}\frac{\partial u_\theta}{\partial \theta} + \frac{u_r}{r} \\ \frac{\partial u_x}{\partial x} \\ \frac{1}{2}\left(\frac{\partial u_r}{\partial x} + \frac{\partial u_x}{\partial r}\right) \\ \frac{1}{2}\left(\frac{1}{r}\frac{\partial u_r}{\partial \theta} + \frac{\partial u_\theta}{\partial r} - \frac{u_\theta}{r}\right) \\ \frac{1}{2}\left(\frac{\partial u_\theta}{\partial x} + \frac{1}{r}\frac{\partial u_x}{\partial \theta}\right) \end{Bmatrix} = \begin{Bmatrix} \frac{\partial u_r}{\partial r} \\ \frac{u_r}{r} \\ \frac{\partial u_x}{\partial x} \\ \frac{1}{2}\left(\frac{\partial u_r}{\partial x} + \frac{\partial u_x}{\partial r}\right) \\ \frac{1}{2}\left(\frac{\partial u_\theta}{\partial r} - \frac{u_\theta}{r}\right) \\ \frac{1}{2}\frac{\partial u_\theta}{\partial x} \end{Bmatrix} \tag{4.13}$$

If we substitute the expression of u_θ in equation (4.11) into equation (4.13), the shear strain rate $\dot{\epsilon}_{r\theta}$ is zero, hence the corresponding stress component $\sigma_{r\theta}$ should also be zero. This is reasonable since the tubes remain in a round shape throughout the welding process. As the corresponding stress component $\sigma_{x\theta}$ to strain rate $\dot{\epsilon}_{x\theta}$ is the shear stress induced directly from friction, which can be got through the study of the deceleration curves, only four stress components remain.

The IN718 material being analysed is assumed to obey the von Mises yield criterion, so that the effective stress is expressed as

$$\sigma_e = \frac{1}{\sqrt{2}}\sqrt{(\sigma_x - \sigma_r)^2 + (\sigma_x - \sigma_\theta)^2 + (\sigma_r - \sigma_\theta)^2 + 6(\sigma_{x\theta}^2 + \sigma_{xr}^2 + \sigma_{r\theta}^2)} \tag{4.14}$$

where σ_x, σ_r and σ_θ are the normal stresses acting in the axial, radial and tangential directions respectively. It can also be expressed by the corresponding deviatoric stress components, S_x, S_r and S_θ, as

$$\sigma_e = \frac{1}{\sqrt{2}}\sqrt{(S_x - S_r)^2 + (S_x - S_\theta)^2 + (S_r - S_\theta)^2 + 6(\sigma_{x\theta}^2 + \sigma_{xr}^2 + \sigma_{r\theta}^2)} \tag{4.15}$$

Then we have

$$\frac{1}{\sqrt{2}}\sqrt{(S_x - S_r)^2 + (S_x - S_\theta)^2 + (S_r - S_\theta)^2} = Y' \tag{4.16}$$

where S_r, S_θ and S_x represent the deviatoric stress components in the radial, circumferential and axial direction respectively. Y' is the modified flow stress of welded material in uniaxial tension/compression with the effect of shear stress components excluded, as to the relationship with the real flow stress Y, the following observes

$$Y' = \sqrt{Y^2 - 3\sigma_{xr}^2 - 3\sigma_{x\theta}^2} \tag{4.17}$$

When the Levy-Mises flow rule of equation (4.8) is used, the deviatoric stress components corresponding to the approximating velocity field in equation (4.11) can be written as follows [85]

$$\begin{cases} S_r = \frac{1+(\frac{r_n}{r})^2}{2(\frac{9}{4}+\frac{3}{4}(\frac{r_n}{r})^4)^{\frac{1}{2}}}Y' \\ S_\theta = \frac{1-(\frac{r_n}{r})^2}{2(\frac{9}{4}+\frac{3}{4}(\frac{r_n}{r})^4)^{\frac{1}{2}}}Y' \\ S_x = -\frac{1}{(\frac{9}{4}+\frac{3}{4}(\frac{r_n}{r})^4)^{\frac{1}{2}}}Y' \\ \sigma_{xr} = \frac{1}{2}\frac{r-(\frac{r_n^2}{r})}{(\frac{9}{4}+\frac{3}{4}(\frac{r_n}{r})^4)^{\frac{1}{2}}}\frac{\phi''(x)}{\phi'(x)}Y' \end{cases} \tag{4.18}$$

where the σ_{xr} is the shear stress in the rox plane.

As $\phi(x)$ is an arbitrary function, σ_{xr} is still unknown in equation (4.18). To get more information about σ_{xr}, Hill's general method is employed in this study [85, 84, 87].

According to the principle of energy conservation, in the case of inertia welding of round tube, we have

$$2\int_0^H \int \left\{\sigma_r \frac{\partial u_r}{\partial r} + \sigma_\theta \frac{u_r}{r} + \sigma_x \frac{\partial u_x}{\partial x} + \sigma_{xr}(\frac{\partial u_r}{\partial x} + \frac{\partial u_x}{\partial r}) + \sigma_{x\theta}(\frac{\partial u_\theta}{\partial x})\right\} dAdx = 2\int (\sigma_x u_x)_{x=H} dA + \dot{E}_{rot} \tag{4.19}$$

where A represents the section of the area, and H is the height of the deformation zone in the HAZ. The item in the left side of the equation is the energy dissipation rate of stress components. The first item in the right side of the equation is the work rate of the external compression load, the second item is the energy dissipation rate of the rotation energy. Here we assume the kinetic energy of the rotating part is all consumed in the work done by the friction induced shear stress $\sigma_{x\theta}$ to generate heat. So we have

$$2\int_0^H \int \sigma_{x\theta}(\frac{\partial u_\theta}{\partial x}) dAdx = \dot{E}_{rot} \tag{4.20}$$

Then equation (4.19) becomes

$$2\int_0^H \int \left\{\sigma_r \frac{\partial u_r}{\partial r} + \sigma_\theta \frac{u_r}{r} + \sigma_x \frac{\partial u_x}{\partial x} + \sigma_{xr}(\frac{\partial u_r}{\partial x} + \frac{\partial u_x}{\partial r})\right\} dAdx = 2\int (\sigma_x u_x)_{x=H} dA \tag{4.21}$$

Hence the shear stress component $\sigma_{x\theta}$ is not included in the analysis, the velocity component u_θ is taken as a constant to let $\sigma_{x\theta}$ be zero in the following deduction. Substitution of the velocity fields in equation (4.11) into equation (4.19) results in

$$\int_0^H \int \left\{-3S_x\phi'(x) + (S_r - S_\theta)(\frac{r_n}{r})^2\phi'(x) + \sigma_{xr}(r - \frac{r_n^2}{r})\phi''(x)\right\} dAdx - 2\int (\sigma_x u_x)_{x=H} dA = 0 \tag{4.22}$$

This equation can be further written as

$$\int_0^H \int \left\{-3S_x\phi'(x) + (S_r - S_\theta)(\frac{r_n}{r})^2\phi'(x) + \sigma_{xr}(r - \frac{r_n^2}{r})\phi''(x)\right\} dAdx = 2P\phi(H) \tag{4.23}$$

where P is the compression load calculated by

$$P = -\int \sigma_x dA \tag{4.24}$$

Integrating by parts to the 3rd item in the left side of the equation (4.23) and noting that

$$P\phi(H) = P\int_0^H \phi'(x) dx \tag{4.25}$$

and $(\sigma_{xr})_{x=0} = 0$, equation (4.23) becomes

$$\int_0^H \left[\int \left\{ 3S_x - (S_r - S_\theta)(\frac{r_n}{r})^2 + (r - \frac{r_n^2}{r})\frac{\partial \sigma_{xr}}{\partial x} \right\} dA + 2P \right] \phi'(x)dx - \phi'(H) \int \sigma_{xr}(H)(r - \frac{r_n^2}{r})dA = 0 \tag{4.26}$$

Since $\phi'(x)$ is an arbitrary function, we have

$$\int \left\{ 3S_x - (S_r - S_\theta)(\frac{r_n}{r})^2 + (r - \frac{r_n^2}{r})\frac{\partial \sigma_{xr}}{\partial x} \right\} dA + 2P = 0 \tag{4.27}$$

and

$$\sigma_{xr}(H) = 0 \tag{4.28}$$

Equation (4.27) states the relationship of the stress components in the deformation zone from the perspective of the force equilibrium of the external load P. This equation can be used to get the change rate of the shear stress $\frac{\partial \sigma_{xr}}{\partial x}$. As σ_{xr} is zero at the origin $x = 0$, the average value of σ_{xr} at each section can be worked out through numerical method.

The effective stress σ_e can then be expressed as

$$\sigma_e = \frac{1}{\sqrt{2}} \left\{ 2Y'^2 + 6\sigma_{x\theta}^2 + 6\sigma_{xr}^2 \right\}^{\frac{1}{2}} \tag{4.29}$$

where $\sigma_{x\theta}$ is the shear stress produced in the material to balance the torque produced from friction.

Then according to the Levy-Mises flow rule, the compression strain rate is

$$\dot{\epsilon_x} = \frac{3S_x \dot{\epsilon_e}}{2\sigma_e} \tag{4.30}$$

In order to perform the mechanical calculation, the length of the tube is discretised with cylindrical elements which are arranged in a 1D fashion along the axial direction. The length l of the tube which is modelled is $70\,\text{mm}$; it is partitioned into n subintervals of equal length $\Delta x = l/n$. The Δx is set to $0.05\,\text{mm}$. Since the length of each subinterval is small, the temperature within the each subinterval can be taken as constant over the length at each time step, without loss of accuracy. For each subinterval, the compression strain rate along axial direction, *i.e.*, x direction is calculated according to equation (4.30). If the effective strain rate $\dot{\epsilon_e}$ is known, the axial strain can be integrated along the length of the tube, and the displacement of the weld line (upset) calculated.

Parameters and boundary conditions used for the round tube model

In this study, a major goal is to analyse the influence of the shear stress $\sigma_{x\theta}$ developed due to frictional effects; as shown in Fig.4.2, this becomes significant at the very last stage of welding and therefore needs to be accounted for. To simplify the calculation, the shear stress in each subinterval of the analytical model is assumed to be identical at each step, due to the balancing effect of the torque. The shear stress is also assumed not to change with the different temperatures assumed in the welding interface. The shear stress used in calculation is from curve 2 in Fig.4.2, whose value is denoted as τ_0 in Table 4.2. The boundary conditions are then

$$\begin{cases} \sigma_x = \frac{P}{A} & x = l \\ \sigma_{x\theta} = \tau_0 & x = 0 \end{cases} \tag{4.31}$$

where P, A denote the axial load and the mating area respectively.

To study the sensitivity of the upset to the process parameters, different values of parameters such as compression stress and interface temperature were assumed in the calculations. Throughout, the upset arising during the heating stage has not been considered because it has been found to be very small. The time for steady stage is taken to be 30 seconds. The compression stress is varied from $150\,$MPa to $250\,$MPa. The calculation conditions used for the calculations are summarised in Table 4.2.

The stages of the calculation of the upset in this mechanical analysis can be summarised as follows:

- The calculation of the temperature field through the thermal analysis.
- The calculation of deviatoric stress S_r, S_θ, S_x through equation (4.18) under the assumed velocity field.
- The determination of shear stress σ_{xr} through equation (4.27) using numerical integration.
- The calculation of the flow stress through equation (4.29).

Table 4.2: Parameters and boundary conditions used for the round tube model.

Parameters	Heating Stage	Steady Stage	Cooling Stage
Axial load σ_x (MPa)		150, 200, 250	150, 200, 250
Shear stress $\sigma_{x\theta}$ (MPa)		τ_0	0
Interface temperature (°C)		1200, 1260	
Prescribed heat flux (W/mm^2)			0

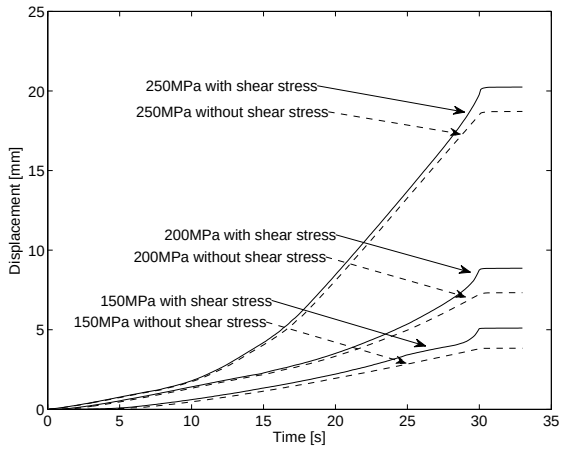

Figure 4.6: Upsets when assuming mating interface temperature 1260°C.

- The determination of the effective strain rate $\dot{\epsilon_e}$ to generate new velocity field by substitution of values for temperature, effective stress and strain into the constitutive equation – the lambda model.
- The determination of the axial strain rate $\dot{\epsilon_x}$ by equation (4.30).
- Calculation of the strain in each sub-element and integration of it along the length of the tube.
- Repetition of the above as necessary, until the simulation is complete.

4.3.3 Results and discussion of round tube model

Fig.4.6 and Fig.4.7 illustrate how the upset is predicted to vary for various levels of the compressive stress. In the calculations, the upset during the heating stage is not considered

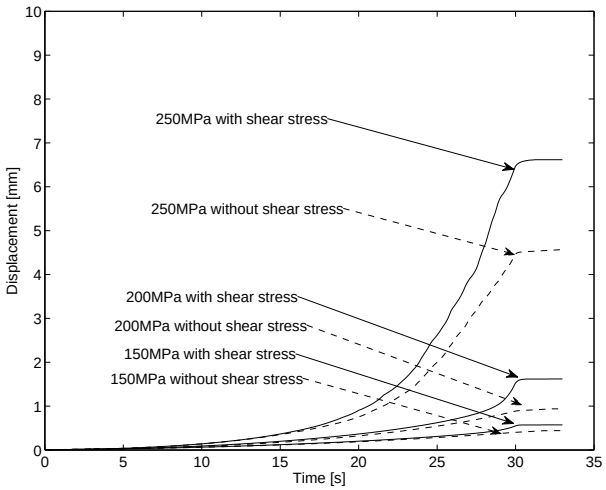

Figure 4.7: Upsets when assuming mating interface temperature 1200°C.

because it is very small due to the short period of this stage. In these graphs, all the curves increase gradually with the increase of time during the steady stage. After 30 seconds, the temperature drops rapidly at the onset of the cooling stage. The upset curves become flat because little plastic deformation happens. With the increase of the compression stress, the upset value becomes bigger. The influence of the shear stress was also studied, as illustrated in Fig.4.6 and Fig.4.7. In these graphs, the shear stress refers to shear stress component $\sigma_{x\theta}$, which is the result of torque produced from the friction in the welding interface. The solid curves represent the upsets got with both the shear stress and the compression stress included in simulation. The dashed lines represent the corresponding curves while the influence of the shear stress is excluded in calculation. The results demonstrate that the combined action of the compression stress and shear stress increases the upset value. The gradient of the curves of the upset has a rapid increase at the end of steady stage, which can be traced to the rapid increase of shear stress at this moment. Comparing the data in Fig.4.6 and Fig.4.7, we can find that the value of upset is sensitive to the interface temperature. In Fig.4.6, when the temperature of welding interface is assumed to be 1260°C, the upset is more than 20mm under the pressure of 250MPa, while in Fig.4.7, the upset value is only about 6.6mm under the pressure of 250MPa when the interface temperature is assumed to be 1200°C.

In the history of friction welding, the question of the welding interface temperature and whether melting occurs on a large scale is a controversial one [35]. Most researchers seem to believe that there is no melting during friction welding [52, 38, 43, 35]. However, it is hard to explain why the friction coefficient in friction welding can be as low as 0.02 during its steady stage, and the friction stress in the steady stage can be lower than 10MPa [50]. This is like a smooth bronze plate slipping on an icy surface. The friction coefficients applicable to metal-metal contact are usually much higher, so it is very possible that some liquid is acting as a lubricant on this occasion [73]. Further, the rapid heating rate during the heating stage of friction welding also suggests that at least some localised melting occurs. Cheng assumed a molten layer in the weld line in his pioneering finite difference method (FDM) model of friction welding. The temperatures computed from Cheng's model agreed well with experimental data [58]. Midling and Grong reported there was a molten layer in friction welding of aluminium alloys to Al-SiC metal matrix composites [36]. Soucail *et al* also reported an incipient melting phenomenon in inertia welding of Astroloy [49]. In their study, a temperature of 1280°C was measured during welding while the solidus and liquidus of the Astroloy are 1250°C and 1345°C respectively, which are very close to those of IN718 [17]. The main reason given by researchers who are against the existence of melting is that the liquid layer would be easily expelled out under axial load, if it is indeed present. What is perhaps not appreciated is the influence of the very steep temperature gradient near the weld line and its complex stress state. Even though there is a very soft, liquid like layer in the weld line, the thickness of it will be small due to the steep temperature gradient. So if a thin soft layer exists near the weld line, it has a tendency to be expelled out radially under the compression pressure; at the same time, it undergoes the impeding effect from the much stronger metal nearby when it is trying to flow out. If the soft layer is thin enough, the action of the compression stress from the axial load will be balanced by the hydrostatic stress exerted upon the soft layer by the material nearby. That means that the soft layer itself does not need to be strong enough to withstand the axial load if the temperature gradient near the weld line is high enough. So from the viewpoint of mechanics, the possibility of having a layer of very soft material lying there needs to

be contemplated. This soft layer is very likely to exist as a semi-solid slurry due to the high temperature there, so it can explain why the friction coefficient is as low as 0.02, since it is the result of the liquid lubrication from this semi-solid layer. The reason why many researchers cannot find evidence of melting is that this semi-solid slurry undergoing high shear rate in friction welding forms a non-dendritic microstructure during solidification, as seen in thixoforming [88].

4.4 Model built for contact zone – thin layer model

4.4.1 Formulae from Navier-Stokes equations

In the above, the round tube model was built based on the principles of mechanics and plasticity theory. In this study, the behaviour of the metal near the mating interfaces was also studied from the viewpoint of fluid mechanics. The thin layer in the weld line, which is mainly the contact zone shown in Fig.2.1, is what we are most interested in and this can be treated as a layer of a viscous fluid. If we want to describe the behaviour of this soft layer, a cylindrical coordinate system shown in Fig.3.1 has to be set up first. Then the Navier-Stokes equation used to describe the movement of the fluids can be written as follows [89, 90, 91],

$$\begin{cases} \rho\left\{\frac{\partial u_r}{\partial t}+u_r\frac{\partial u_r}{\partial r}+\frac{u_\theta}{r}\frac{\partial u_r}{\partial \theta}+u_x\frac{\partial u_r}{\partial x}-\frac{u_\theta^2}{r}\right\}=-\frac{\partial P}{\partial r}+\mu\left\{\frac{1}{r}\frac{\partial}{\partial r}(r\frac{\partial u_r}{\partial r})+\frac{1}{r^2}\frac{\partial^2 u_r}{\partial \theta^2}+\frac{\partial^2 u_r}{\partial x^2}\right. \\ \qquad\qquad \left.-\frac{u_r}{r^2}-\frac{2}{r^2}\frac{\partial u_\theta}{\partial \theta}\right\}+\rho g_r \\ \rho\left\{\frac{\partial u_\theta}{\partial t}+u_r\frac{\partial u_\theta}{\partial r}+\frac{u_\theta}{r}\frac{\partial u_\theta}{\partial \theta}+u_x\frac{\partial u_\theta}{\partial x}+\frac{u_r u_\theta}{r}\right\}=-\frac{\partial P}{r\partial \theta}+\mu\left\{\frac{1}{r}\frac{\partial}{\partial r}(r\frac{\partial u_\theta}{\partial r})+\frac{1}{r^2}\frac{\partial^2 u_\theta}{\partial \theta^2}+\frac{\partial^2 u_\theta}{\partial x^2}\right. \\ \qquad\qquad \left.-\frac{u_\theta}{r^2}+\frac{2}{r^2}\frac{\partial u_r}{\partial \theta}\right\}+\rho g_\theta \\ \rho\left\{\frac{\partial u_x}{\partial t}+u_r\frac{\partial u_x}{\partial r}+\frac{u_\theta}{r}\frac{\partial u_x}{\partial \theta}+u_x\frac{\partial u_x}{\partial x}\right\}=-\frac{\partial P}{\partial x}+\mu\left\{\frac{1}{r}\frac{\partial}{\partial r}(r\frac{\partial u_x}{\partial r})+\frac{1}{r^2}\frac{\partial^2 u_x}{\partial \theta^2}+\frac{\partial^2 u_x}{\partial x^2}\right\}+\rho g_x \end{cases} \tag{4.32}$$

where u_r, u_x and u_θ represent the velocity components in the radial (r), axial (x) and circumferential (θ) directions respectively. μ is the viscosity of the thin layer. ρ is the density. P is the pressure exerted on the layer. g_r, g_x and g_θ denote the external body force components in the radial (r), axial (x) and circumferential (θ) directions respectively.

The Navier-Stokes equation is a direct application of Newton's second law on the movement of the fluid. The three expressions describe the principle of the conservation of momentum in a fluid along the radial (r), axial (x) and circumferential (θ) directions respectively.

At the same time, the velocity fields of the fluid should obey the principle of volume conservation, or continuity equation

$$\frac{1}{r}\frac{\partial}{\partial r}(ru_r) + \frac{1}{r}\frac{\partial u_\theta}{\partial \theta} + \frac{\partial u_x}{\partial x} = 0 \tag{4.33}$$

The Navier-Stokes equations seem formidable and difficult to solve. However, in the case of inertia welding a round tube, these equations can be greatly simplified in analysing the thin layer at the mating interfaces.

Since what we are interested in is the thin layer of metal, the effect of body forces on it usually is very small and can be neglected. That means that the three body force components g_r, g_x and g_θ can be taken as zero. Another assumption is that there is no gradient of velocity and pressure in the circumferential direction as the thin layer is in a circular shape. Thus,

$$\frac{\partial u_r}{\partial \theta} = \frac{\partial u_\theta}{\partial \theta} = \frac{\partial u_x}{\partial \theta} = \frac{\partial P}{\partial \theta} = 0 \tag{4.34}$$

Then the second expression in equation (4.32), which describes the momentum balance in circular direction, can be written as

$$\rho\left\{\frac{\partial u_\theta}{\partial t} + u_r\frac{\partial u_\theta}{\partial r} + u_x\frac{\partial u_\theta}{\partial x} + \frac{u_r u_\theta}{r}\right\} = \mu\left\{\frac{1}{r}\frac{\partial}{\partial r}(r\frac{\partial u_\theta}{\partial r}) + \frac{\partial^2 u_\theta}{\partial x^2} - \frac{u_\theta}{r^2}\right\} \tag{4.35}$$

As the tangential velocity u_θ can be expressed as

$$u_\theta = r\omega \tag{4.36}$$

where r, ω represent radius and rotation speed of the thin layer respectively, one can replace u_θ with $r\omega$ in equation (4.35), so that

$$\rho\left\{\frac{\partial(r\omega)}{\partial t} + u_r\frac{\partial(r\omega)}{\partial r} + u_x\frac{\partial(r\omega)}{\partial x} + \frac{u_r(r\omega)}{r}\right\} = \mu\left\{\frac{1}{r}\frac{\partial}{\partial r}(r\frac{\partial(r\omega)}{\partial r}) + \frac{\partial^2(r\omega)}{\partial x^2} - \frac{(r\omega)}{r^2}\right\} \tag{4.37}$$

We can assume the rotation speed of the thin layer decreases linearly along the direction of its thickness

$$\omega = \omega_0 \frac{x}{h} \tag{4.38}$$

where the ω_0 is the nominal rotating speed of the rotating part, its typical variation is like the curve 2 in Fig.4.1. The symbol x is the local coordinate along axial direction; it is set a value of zero on the thin layer's border to the static part and a value of h at the border to the rotating part, as shown in Fig.4.9. Then we have

$$\frac{\partial^2 \omega}{\partial x^2} = 0 \tag{4.39}$$

Hence the right side of the equation (4.37) equals zero, from the left side we can further get

$$r\frac{\partial \omega}{\partial t} + 2u_r\omega + ru_x\frac{\partial \omega}{\partial x} = 0 \tag{4.40}$$

So we have

$$u_r = -\frac{r}{2\omega}\left\{\frac{\partial \omega}{\partial t} + u_x\frac{\partial \omega}{\partial x}\right\} \tag{4.41}$$

Using equation (4.38), formula (4.41) can be further written as

$$u_r = -\frac{r}{2\omega_0}\frac{\partial \omega_0}{\partial t} - \frac{r}{2x}u_x \tag{4.42}$$

The continuity equation (4.33) can also be written as follows after using expression (4.34)

$$\frac{\partial u_r}{\partial r} + \frac{u_r}{r} + \frac{\partial u_x}{\partial x} = 0 \tag{4.43}$$

Substituting the expression for u_r in equation (4.43) with the expression in equation (4.42), we finally have

$$\dot{\epsilon_x} = \frac{\partial u_x}{\partial x} = \frac{1}{\omega_0}\frac{\partial \omega_0}{\partial t} + \frac{u_x}{x} \tag{4.44}$$

Equation (4.42) and equation (4.44) are the formulae we are interested in.

4.4.2 Discussion and results

Equation (4.42) and equation (4.44) are the results of the direct application of the Navier-Stokes equations on the circular thin viscous layer of the metal near the weld line. They

define the necessary requirement for the velocity fields to satisfy the principle of momentum conservation.

From equation (4.42), we find that the radial flow speed u_r, *i.e.*, the speed of the welding metal flowing in the flash direction, is not only related with the rate of axial shortening (upsetting rate) u_x, but also strongly influenced by the rotation speed ω. If we look at the the first item on the right side of the equation (4.42), which represents the effect of velocity in the circumferential direction, its absolute value is expected to increase very quickly at the last seconds of the steady-state stage, because the value of the rotation speed ω_0 is nearing zero and the rate of the deceleration of the rotation $\frac{\partial \omega_0}{\partial t}$ is found high at this moment from the deceleration curve of the inertia welding. From equation (4.44), the upsetting speed u_x also increases when the rotation is coming to a stop. This increase of u_x leads to a further increase of the radial speed u_r in equation (4.42). So from these two formulae, we can see that there is an unavoidable rapid increase of the radial flow speed of the welding metal due to the cessation of rotation in the friction welding of circular objects. This rapid increase of the radial flow speed u_r leads to the squeezing of the soft material near the weld line at the last seconds of the steady state stage, which is also referred as the extrusion phenomenon in inertia welding. This extrusion behaviour of material is the cause of the burr, or internal flash shown in Fig.2.1. Thus the formation of the burr is a direct result of the balance of the momentum due to the rapid stop of rotation. From equation (4.42) we also find that the radial flow speed u_r increases with an increase in the radius r, which implies that the extrusion of the burr is more likely to happen during the inertia welding of larger parts.

Equation (4.44) shows that the axial strain rate $\dot{\epsilon_x}$ is also influenced by the rotation speed. This formula can be used to estimate the upset of inertia welding. We can take the axial velocity at the border of the thin layer to rotating part as the axial shortening rate of the whole welding part. That means the x in equation (4.44) equals h. Using the deceleration curve shown in Fig.4.1, the whole upset of inertia welding can be worked out through integration over the time. Fig.4.8 illustrates some results of upsets got with different thickness of the contact zone assumed. From the graph we can find that the value of upsets is very sensitive to the thickness of the thin layer h. When the thickness of the contact zone

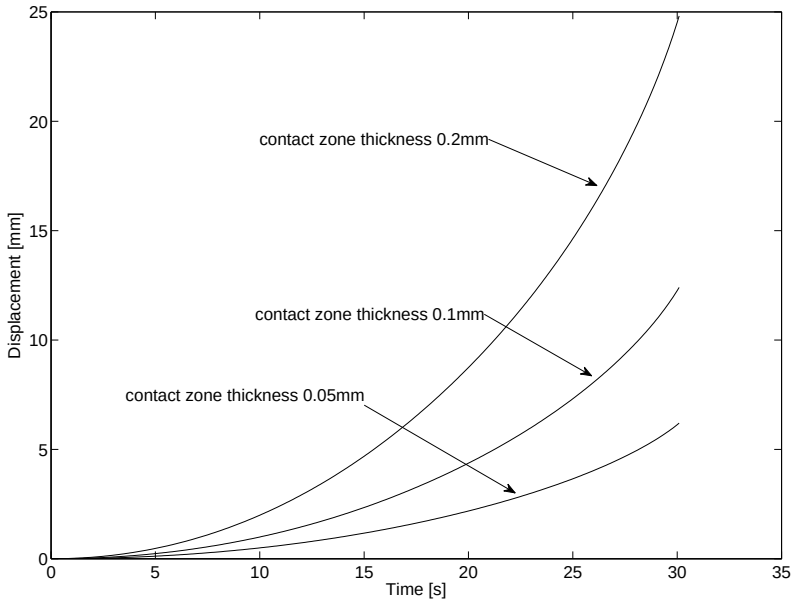

Figure 4.8: Upsets got through formula 4.44.

increases from 0.1mm to 0.2mm, the upset value increases rapidly from 12mm to 24mm.

It should be pointed out that the effects of the compression stress, temperature and the constitutive relationship of the material are not taken into consideration in the formulae got from the Navier-Stokes equations. However, their influence may be embodied in the thickness of the contact zone h, through which further influences the axial shortening rate.

In fact, as illustrated in the Fig.4.9, a relationship between the compression pressure and the width of the soft thin layer can even be achieved through a force balance in the radial direction. The deduction is as follows. We can choose an element in the soft layer of length of dr and height h. The element is subjected to the compression pressure from both sides and the impeding shear stresses σ_{xr} from top and bottom. As the force in the radial direction needs to be balanced, in a cylindrical coordinate system an equation can be written

$$(P + \frac{\partial P}{\partial r}dr)hrd\theta - Phrd\theta = 2\sigma_{xr}rdrd\theta \tag{4.45}$$

where $d\theta$ is the small angle corresponding to the element. Hence

$$\frac{\partial P}{\partial r}h = 2\sigma_{xr} \tag{4.46}$$

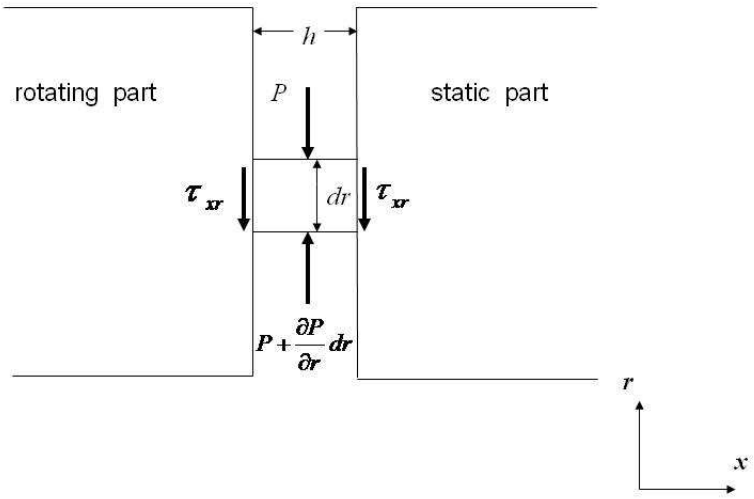

Figure 4.9: Forces acting on an element of the thin soft layer, in the radial direction.

From the equation, we can find that the thickness of the thin layer h is inversely proportional to the axial load if the value of σ_{xr} does not vary a lot. Since the most likely state for this thin soft layer is a semi-solid, mushy zone with a small fraction of liquid in it, a temperature of 1260°C is assumed in the weld line during inertia welding of IN718 in this study. Some researchers believe this is the point that IN718 just start to melt [17, 70]. But according to Lewandowski and Overfelt's work, IN718 is already in semi-solid state. The main structure of the metal is still solid which maintains some strength for the metal; however at the same time, a small fraction of liquid lies in the intergranular zone which eases the deformation greatly [72]. With equation (4.46), a rough estimate of the thickness of the thin layer can be made. We can approximate the stress σ_{xr} as the shear strength of the welding material; a suitable value can be found in the Fig.4.2. As the thin layer is assumed to be a slurry like layer, the compression pressure is further assumed to be built up inwardly from the free surfaces in a short distance *e.g.* 1mm. From Fig.4.2, the shear

stress varies from 6MPa to 12MPa in the former 24 seconds. If the compression stress is the same as before, 250MPa, then the thickness of the thin layer varies from 50-100μm. In the last seconds of steady state welding, the shear stress increases quickly, which implies that this thin layer has a tendency to increase quickly, its thickness can reach 0.4mm if the shear stress reaches a peak value of 50MPa.

4.5 Model built by variational method

4.5.1 Deduction of formula for velocity field at the weld line

In metal deformation, the following variational principle is applicable. It states that among all admissible velocities u_i that satisfy the conditions of compatibility and incompressibility, as well as the velocity boundary conditions, the actual solution gives the following functional a stationary value [84]:

$$\pi = \int_V \sigma_{ij}\dot{\epsilon_{ij}}dV - \int_{S_F} F_i u_i dS \tag{4.47}$$

where σ_{ij}, $\dot{\epsilon}_{ij}$ are the stress and strain rate tensors respectively, and F_i represents the external forces acting over surface S_F. In this part of study, the mechanical part of the problem is reduced to that of a thin-walled tube under combined loading of the axial compressive stress and the shear stress arising from frictional effects. To analyze it, it is necessary to have a cylindrical coordinate system, as illustrated in Fig.3.1. The axial direction is labelled as x and the radial as r; the tangential direction θ is normal to the plane of the diagram.

In inertia welding of tubes, it is assumed that there is no variation of the velocity fields along the circular (tangential) direction. As a round tube is still a round tube after welding, the circular velocity component has little influence on the shape change. To further simplify the analysis, the same assumption used in round tube model is also adopted here, that is, the kinetic energy of the rotating part is all consumed in the work done by the friction induced shear stress $\sigma_{x\theta}$ to generate heat, only the deformation in plane xor is taken into consideration, the strain induced by the shear stress component $\sigma_{x\theta}$ is excluded in the

analysis, which means that the problem is actually taken as an axisymmetrical one. In this case, the velocity component in tangential direction u_θ is taken as a constant C_4 to let $\sigma_{x\theta}$ be zero in the following analysis. Thus the velocity fields u_i can be assumed as follows

$$\begin{cases} u_r = \frac{1}{2}(r - \frac{r_n^2}{r})\acute{\phi}(x) \\ u_\theta = C_4 \\ u_x = -\phi(x) \end{cases} \tag{4.48}$$

where r_n is the neutral radius, which in this study is taken as the average value of inner and outer radius of the tube, $\frac{r_0+r_1}{2}$, where r_0, r_1 denote the inner and outer radius of the tube respectively. The terms u_r, u_θ and u_x are the velocity components in the radial (r), circumferential (θ) and axial (x) directions respectively. Note that the velocity fields in equation (4.48) satisfy volume conservation automatically.

Under this pseudo-axisymmetrical situation, equation (4.47) can be written as

$$\pi = 2\int_0^H \int \left\{ \sigma_r \frac{\partial u_r}{\partial r} + \sigma_\theta \frac{u_r}{r} + \sigma_x \frac{\partial u_x}{\partial x} + \sigma_{xr}(\frac{\partial u_r}{\partial x} + \frac{\partial u_x}{\partial r}) \right\} dAdx - 2\int (\sigma_x u_x)_{x=0} dA \tag{4.49}$$

where A represents the section of the area, and H is the height of the deformation zone. Here, for the convenience of analysis, the origin of the coordinate system is assumed to be settled at the border of the deformation zone and does not move with the flow of material, which is different from the one used in the round tube model. Thus one has

$$\phi(H) = 0 \tag{4.50}$$

Substituting u_i with expressions in equation(4.48), we have

$$\pi = \int_0^H \left[\int \left\{ -3S_x\phi'(x) + (S_r - S_\theta)\frac{r_n^2}{r^2}\phi'(x) + \sigma_{xr}(r - \frac{r_n^2}{r})\phi''(x) \right\} dA \right] dx + 2\bar{\sigma}_x A\phi(0) \tag{4.51}$$

where $\bar{\sigma}_x$ represents average compression stress, or nominal compression stress, which is usually known. $\phi(0)$ is the velocity in the axial direction at the welding interface. To make the analysis simple, the Tresca yield criterion is adopted,

$$S_r - S_x = Y \tag{4.52}$$

where Y is the flow stress of welded material in uniaxial tension or compression, and S_r, S_x represent the deviatoric stress components in the radial and axial direction respectively.

When the Levy-Mises flow rule expressed in equation (4.8) is used, the deviator stress components corresponding to the approximating velocity field in equation (4.48) can be written as follows

$$\begin{cases} S_r = \frac{1+(r_n/r)^2}{3+(r_n/r)^2}Y \\ S_\theta = \frac{1-(r_n/r)^2}{3+(r_n/r)^2}Y \\ S_x = -\frac{2}{3+(r_n/r)^2}Y \\ \sigma_{rx} = \frac{1}{2}\frac{r-(r_n^2/r)}{3+(r_n/r)^2}\frac{\phi''(x)}{\phi'(x)}Y \end{cases} \tag{4.53}$$

where Y is the flow stress of welding material. For a thin-walled tube, which means $r \approx r_n$, equation (4.53) becomes

$$\begin{cases} S_r = \frac{1}{2}Y \\ S_\theta = 0 \\ S_x = -\frac{1}{2}Y \\ \sigma_{rx} = 0 \end{cases} \tag{4.54}$$

Substituting equation (4.54) into equation (4.51), we have

$$\pi \approx \int_0^H \left[\int \{2Y\phi'(x)\}\, dA\right] dx + 2\bar{\sigma}_x A\phi(0) \tag{4.55}$$

Integrating by parts the first item in the right side of equation (4.55), one has,

$$\frac{\pi}{2} \approx \phi(H)Y(H)A - \phi(0)Y(0)A - \int_0^H A\frac{dY}{dx}\phi(x)dx + \bar{\sigma}_x A\phi(0) \tag{4.56}$$

where $Y(0)$, $Y(H)$ represent the flow stress of metal at the weld line and deformation boundary $x = H$, respectively. The term $\frac{dY}{dx}$ represents the rate of change of the flow stress of welding material along the axial direction, which is later denoted as K_Y. In inertia welding, the temperature at the weld line is the highest; the strain rate there is also the highest. At the boundary of the deformation zone, the deformation rate is near zero due to the much higher flow stress of metal caused by the steep temperature gradient. So $\phi(H)$ is near zero, we have

$$\frac{\pi}{2A} = \pi' = [\bar{\sigma}_x - Y(0)]\,\phi(0) - K_Y(\zeta)\int_0^H \phi(x)dx \tag{4.57}$$

where $K_Y(\zeta)$ denotes the rate of change of the flow stress at some point within the deformation zone. From the calculation results shown in the thermal analysis, we know that the temperature gradient gets the highest value at the weld line and the flow stress of metal is highly sensitive to temperature, so K_Y gets highest value at the weld line.

To minimize π', we have

$$K_Y(\zeta) = K_Y(0) \tag{4.58}$$

Then

$$\pi' = [\bar{\sigma}_x - Y(0)]\,\phi(0) - K_Y(0)\int_0^H \phi(x)dx \tag{4.59}$$

We assume a test function

$$\phi(x) = a_0 \exp(-a_1 x) \tag{4.60}$$

where a_0, a_1 are constants. One substitutes equation(4.60) into equation(4.59), and seeks a stationary value. Through

$$\frac{\partial \pi'}{\partial a_0} = 0 \tag{4.61}$$

a_1 can be estimated as

$$a_1 = \frac{\bar{\sigma}_x - Y(0)}{K_Y(0)} \tag{4.62}$$

In inertia welding, deformation is focussed at the zone near weld line, so that the strain rate drops greatly with an increase of the distance to the welding interface. When $x = H$, at the border of the deformation zone, the change of strain rate should be very small. Here we assume, when $x = H$,

$$\frac{d\dot{\epsilon}_x}{dx} = C_2 \tag{4.63}$$

where C_2 is a very small value. So we have

$$a_0 = C_2 \left\{ \frac{K_Y(0)}{\bar{\sigma}_x - Y(0)} \right\}^2 \exp\left\{ \frac{\bar{\sigma}_x - Y(0)}{K_Y(0)} H \right\} \tag{4.64}$$

Finally, the velocity component of deformation zone along axial direction during inertia welding can be described as

$$\phi(x) = C_2 \left\{ \frac{K_Y(0)}{\bar{\sigma}_x - Y(0)} \right\}^2 \exp\left\{ \frac{\bar{\sigma}_x - Y(0)}{K_Y(0)} H \right\} \exp\left\{ -\frac{\bar{\sigma}_x - Y(0)}{K_Y(0)} x \right\} \tag{4.65}$$

With this formula, the upsets of inertia can be estimated. At the welding interface, when $x = 0$, then the velocity in axial direction at the weld line can be expressed as

$$\phi(0) = C_2 \left\{ \frac{K_Y(0)}{\bar{\sigma}_x - Y(0)} \right\}^2 \exp \left\{ \frac{\bar{\sigma}_x - Y(0)}{K_Y(0)} H \right\} \tag{4.66}$$

By integrating this velocity with the time of inertia welding, the upsets can be predicted.

4.5.2 Results and discussion

In applying equation (4.66), we need to know the rate of change of the flow stress at the weld line, which requires the temperature fields and the corresponding constitutive equation of the welding material to be known. In the calculations which follow, the temperature fields in the thermal analysis of chapter 3 was adopted. The lambda model was used to describe the flow stress of the IN718. One expects C_2 to be a small value; here it is tentatively taken as 0.001. The height of the deformation zone is defined as the distance between the weld line to the point where its temperature is above 900°C. The temperature of the weld line is assumed as before 1260°C. The welding time is assumed the same as that used in the former two models, 30 seconds. Some upsets calculated under various compression pressures are shown in Fig.4.10.

From the graph, the upset value increases with time and compression load, which seems plausible. The influence of the different interface temperature can also be represented in this formulation. In Fig.4.11, the solid lines denote the upset values when assuming a temperature of 1260°C at the weld line, while the dashed lines are the upsets at a temperature of 1200°C. The graph shows that the axial shortening rate drops quickly when the temperature drops from 1260°C to 1200°C. Thus equation (4.66) provides a quick and simple way for engineers to estimate the displacement of the weld line during friction welding. To assure the accuracy of the equation (4.66), the precise temperature fields of friction welding and the constitutive equation of the welding materials at high temperature are the basic requirements. All of these demand extensive experimental work in this field. One thing which needs to be pointed out is that equation (4.66) cannot be used to predict the upset in

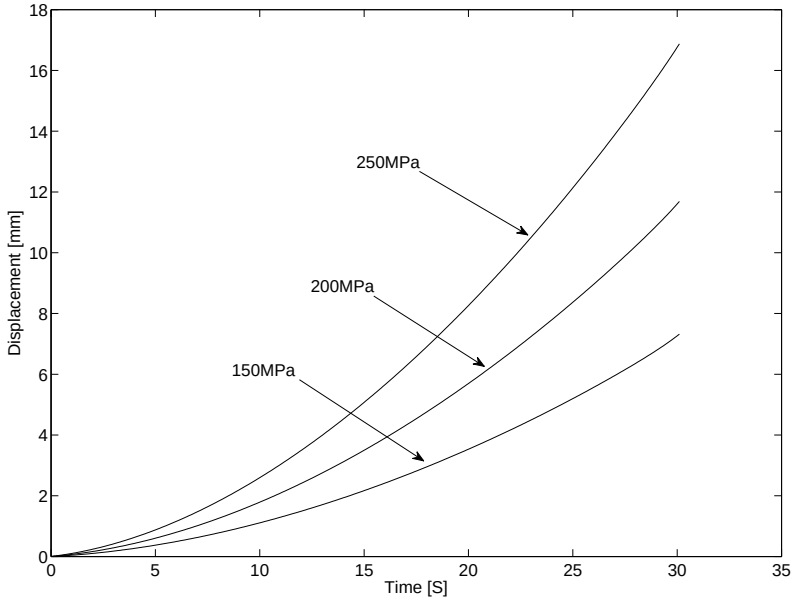

Figure 4.10: Upset curves estimated assuming different compression stresses using the variational method.

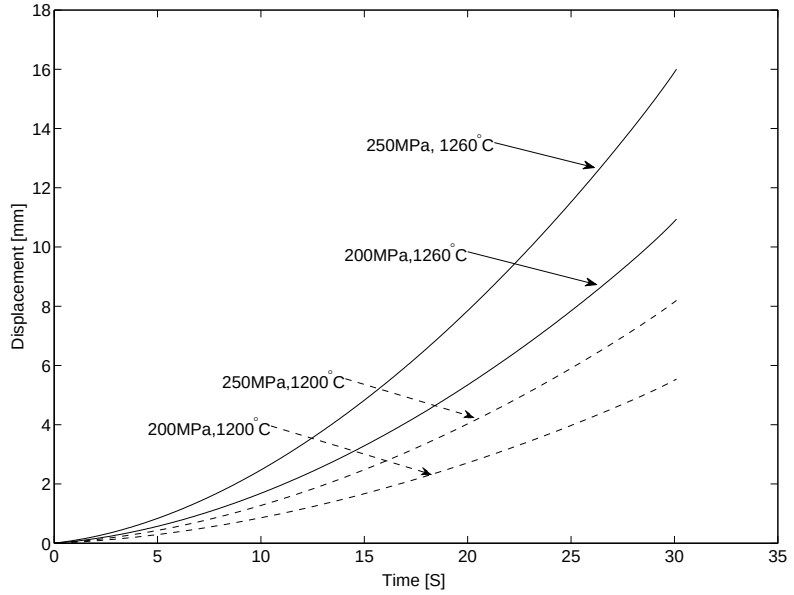

Figure 4.11: Upsets got under different temperature and compression stresses using the variational method.

the cooling stage. The reason is that the change rate of the flow stress $K_Y(\zeta)$ is no longer the largest at the weld line during cooling stage.

4.6 Comparison of the three mechanical models

In this chapter, three different mechanical models were developed to describe the inertia friction welding process. Each of these three models can be used to predict the upset expected. For the first model - the round tube model - the finite difference method is adopted. In this model, the upsets in both the steady state stage and the cooling stage are predicted. The effect of the shear stress induced by the friction at the mating surfaces can also be taken into consideration. For the second model - the thin layer model - it is a direct application of the Navier-Stokes equation for the case of friction welding of round tube. It is an analytical solution with simple formulae, which brings us new understanding from the perspective of balance of momentum. The formation of the burr at the last seconds of the friction welding tubular parts can be rationalised using this model. The shear stress does not appear in the formulae in this model directly; however, its influence is represented in the item $\frac{\partial \omega_0}{\partial t}$ in equation (4.44), which is proportional to the amplitude of the shear stress. The third model is also an analytical one. This concise formulation is arrived at from the variational principle. It provides a convenient method for engineers to estimate the upset value during inertia welding. However, the influence of the shear stress is not represented in this model. The last two analytical solutions cannot be used in cooling stage of welding. In Fig.4.12, some results of these three models are placed together. It is hard for the author to say which model is better as there is no practical data at hand for validation. The stress state of the welding material near weld line is more rigorously considered in the round tube model. The torsional effect, *i.e.* the influence of the shear stress, can be included. This is believed to be the first attempt at this kind of model. However, it is still a numerical one compared with the two other models. The thin layer model, which is derived from the Navier-Stokes equations, can give us more understanding of the welding process. It can give us a clear explanation of the extrusion of the burr and the size effect can also be

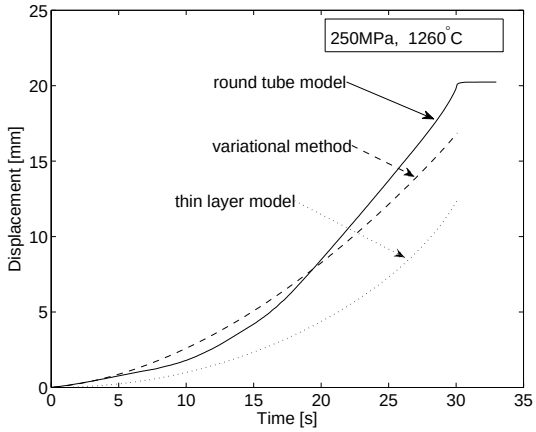

Figure 4.12: Comparison of the upset predicted by the three mechanical models.

included in this model. There is nevertheless some uncertainty about the thickness of the thin layer in the model. Some experimental work is required to calibrate the thickness of the thin layer when used in practice to predict the upsets of the process. The model from the variational method can also provide a simple estimation of the upsets in welding if we have knowledge of the flow stress of the welding material at high temperature. However, the torsional effect cannot be included in the model directly. The determination of the constant C_2 and the height of deformation zone H in equation (4.65) for practical usage also require some experimental work.

4.7 Summary

In this chapter, three different mechanical models for inertia welding were built from different perspectives. From the thin-walled tube model, we find that the shear stress induced from the friction at the mating interfaces does increase the upset value observed in the friction welding process. The rapid increase of the upset at the last seconds of the steady-state stage process is attributed to the rapid increase of the shear stress at that moment. The calculation results from this model also show that the axial shortening rate also rises with an increase in the axial compression load. Another finding is that the upset value is sensitive to the temperature of the weld line assumed, which implies the importance of the accurate

temperature fields for mechanical analysis in friction welding.

The thin layer model indicates that the axial shortening rate is not only influenced by the material flow rate in side directions, but also by the change in the rate of the rotation speed in inertia welding of tubes. This rapid deceleration of the rotation speed at the last seconds of the steady stage implies there are rapid increases of the axial shortening rate and the radial flow speed. The latter one is also described as the extrusion phenomenon in inertia welding. This extrusion phenomenon can be rationalised as a result of the balance of the momentum at the last seconds of the inertia welding. The thin layer model also predicts that there is more tendency for this extrusion phenomenon to happen with inertia welding parts of larger radius.

The model from the variational method can provide engineers with a convenient method to estimate the upset value occurring in friction welding. Similar to the results obtained from the round tube model, this model also indicates the sensitivity of the upsetting rate to the axial load and the temperature at the mating interfaces. But the torsional effect cannot be included into this model directly as yet.

Chapter 5

FEM Model of Inertia Welding

5.1 Introduction to FEM model

5.1.1 $2\frac{1}{2}$D element

The analytical models make some significant assumptions and it is of interest to compare their results with those made using the finite element method. For this purpose, the commercial FEM code DEFORM-2D has been used, in which a pseudo axi-symmetric element is available to simulate inertia welding which allows torsional effects to be treated [63]. The basis for the finite-element method is the variational method. It states that among all admissible velocity u_i that satisfy the boundary conditions, the solution velocity field makes the following functional a minimum value [84]

$$\delta\pi = \int_V \sigma_e \delta\dot{\epsilon_e} dV + K_p \int_V \dot{\epsilon_v} \delta\dot{\epsilon_v} dV - \int_{S_F} F_i \delta u_i dS = 0 \tag{5.1}$$

where $\dot{\epsilon_v}$ is the volumetric strain rate, F_i is the surface traction over its surface S_F, and K_p is a penalty constant. In DEFORM, to describe the torsional effects while keeping the 2D axi-symmetric condition for computational efficiency, it is assumed that there is no velocity gradient in the circumferential direction for the velocity fields involved [63]. The velocity

field is as follows

$$\begin{cases} u_r = u_r(r,x) \\ u_x = u_x(r,x) \\ u_\theta = u_\theta(r,x) \end{cases} \tag{5.2}$$

where u_r, u_x and u_θ are the velocity components in the radial (r), axial (x) and circumferential (θ) directions respectively. The related strain rate tensor is as follows

$$\dot{\epsilon_{ij}} = \begin{Bmatrix} \dot{\epsilon_r} \\ \dot{\epsilon_x} \\ \dot{\epsilon_\theta} \\ \dot{\gamma_{rx}} \\ \dot{\gamma_{r\theta}} \\ \dot{\gamma_{x\theta}} \end{Bmatrix} = \begin{Bmatrix} \frac{\partial u_r}{\partial r} \\ \frac{\partial u_x}{\partial x} \\ \frac{u_r}{r} \\ \frac{\partial u_r}{\partial x} + \frac{\partial u_x}{\partial r} \\ \frac{\partial u_\theta}{\partial r} - \frac{u_\theta}{r} \\ \frac{\partial u_\theta}{\partial x} \end{Bmatrix} \tag{5.3}$$

The corresponding deviatoric stress tensor can be calculated with the Levy-Mises flow rule, as shown in equation(4.8). So compared with conventional axi-symmetric model, apart from σ_{rx}, two more shear stress components, *i.e.*, $\sigma_{r\theta}$, $\sigma_{x\theta}$ can also be worked out by DEFORM-2D's special element for torsion. This element may be called $2\frac{1}{2}$D element.

5.1.2 Friction model

In DEFORM, there are several ways to define the friction behaviour of the material [92]. In this study, the Coulomb friction is used to describe the interface behaviour. In the Coulomb model, the frictional shear stress is defined as

$$\tau_f = \mu_0 P_c \tag{5.4}$$

where τ_f is the frictional shear stress, μ_0 is the friction coefficient, P_c is the normal compression stress. As mentioned before, although there has already been lots of research to determine the friction coefficient in friction interfaces, there is still no clear progress in this field. Some researchers assume the friction coefficient as a function of the interface temperature, axial pressure, and sliding speed [39, 40, 41, 63], but these expressions have almost no general applicability. In the present study, the Coulomb friction coefficient is defined

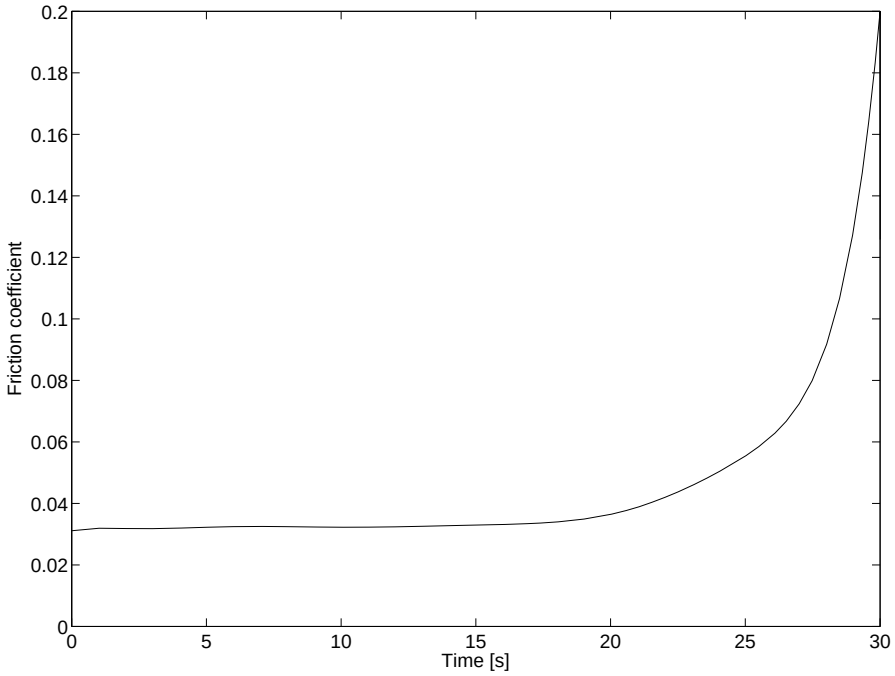

Figure 5.1: Variation of friction coefficient used in FEM simulation under a load of 250MPa.

as a function of time. Its value is set according to the normal loads to make the resulting frictional shear stress the same as the value shown in curve 2 of Fig.4.2. For example, if the axial load is 250MPa, the corresponding curve for the friction coefficient is illustrated in Fig.5.1.

5.1.3 Heat transfer analysis

The variational form of the heat transfer problem can be written as follows [84],

$$\int_v KT_{,i}\delta T_{,i}dV + \int_v \rho c\dot{T}\delta T dV - \int_{S_q} q\delta T dS - \int_v C_3\sigma_{ij}\dot{\epsilon_{ij}}\delta T dV = 0 \qquad (5.5)$$

where K denotes thermal conductivity, q is the heat flux across the boundary surface S_q, and the comma denotes differentiation. The term C_3 is the heat generation efficiency, representing the fraction of mechanical energy transformed into heat; it is usually assumed to be 0.9. ρ, c are the density and heat capacity of the material respectively.

To facilitate the comparison with the analytical solutions, the heat loss due to convec-

tion and radiation is also not considered in the FEM model.

5.1.4 Mesh

DEFORM can automatically remesh the deformation zone when the solver cannot converge on a solution in a time step. This is very useful when coping with the problems of large plastic strain, for instance, the heavy plastic deformation near the weld line. This is the main reason why it has become the most popular FEM tool used in the simulation of inertia welding. In the present study, only one section is chosen to represent each billet since the billet is axisymmetrical. There are 1047 quadrilateral elements for one section of the billet, with the mesh chosen to be much finer close to the weld interface in order to capture the large plastic strain and steep temperature fields occurring there. The size of the smallest element is around 0.4mm, the size of the largest one is around 1mm. In fact, different meshes were tried in the simulation. The finest mesh used adopted about 10000 quadrilateral elements for one billet, in which the size of the smallest element is only 0.03mm. The results of this fine mesh were not substantially different from those of the former coarse one while take much longer time to finish one simulation. Bennett *et al* stated that a mesh size of approximately 0.3mm at the welding interface is fine enough to ensure the accuracy of the simulation in inertia welding [66]. D'Alvise also held that a mesh size of 0.4mm is reasonable[42]. Thus, this coarse mesh shown in Fig.5.2 is used in this study.

5.1.5 FEM simulation procedure

To enable a fair comparison with the analytical solutions, the thermal properties of IN718 employed are exactly those used in the thermal analysis, as listed in Table 3.1. The constitutive relationship of the material in FEM is also the same as the one used in analytical models, the lambda model; it is described from equation (4.4) to equation (4.6) and its parameters are listed in Table 4.1. It was input into the FEM model via a fortran subroutine

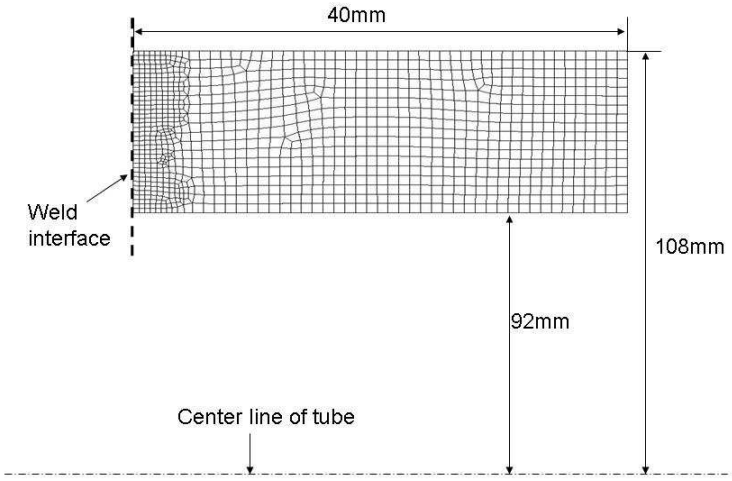

Figure 5.2: Mesh of one billet used in FEM simulation, containing 1047 elements and 1126 nodes.

through the interface in DEFORM. The simulation procedure for inertia welding was also divided into three stages. In the heating stage, heat is generated at the welding interface and represented by a heat flux of 5W/mm^2. In the steady state stage, the temperature of the welding interface is assumed to be fixed at 1260°C; at the same time, the axial load and the frictional shear stress illustrated in curve 2 of Fig.4.2 are applied to the billets. The time of the steady state stage is also assumed to be 30 seconds. In the cooling stage, the heat flux in the welding interface is zero while the axial pressure is maintained for some time. Thus the boundary conditions used in FEM model are the same as those used in the former analytical calculations.

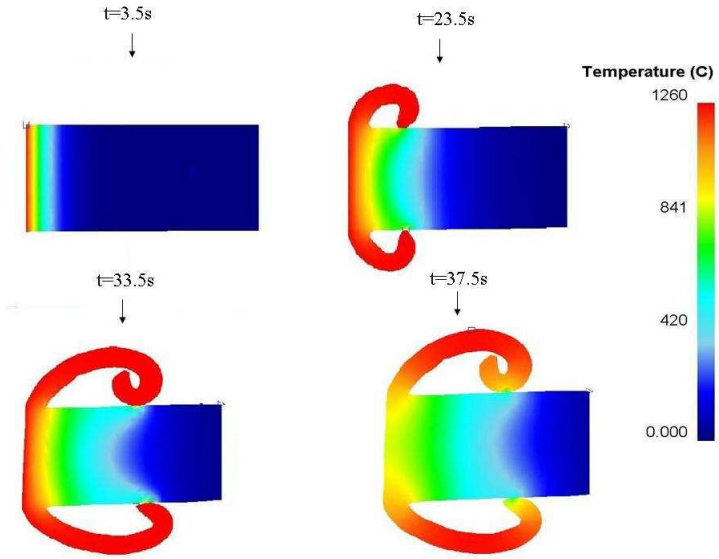

Figure 5.3: The temperature fields from FEM simulation.

5.2 Results and discussion

5.2.1 Thermal results

Temperature fields

The temperature distributions from the FEM model are illustrated in Fig.5.3. In the right side of the graph, there is a colour scale bar. The billet at the upper left denoted with t=3.5s represents the temperature field after 3.5 seconds of heating stage. The upper right one with 23.5s refers to the temperature field 20 seconds after the start of the steady-state stage. The lower left one denotes the temperature at the end of the steady-state stage. The billet at the lower right represents the temperature field 4 seconds after the start of the cooling stage. From the graph, we can see that the temperature drops quickly from the weld line along the axial direction. As the welding time increases, the temperature gradient drops. We can also find that the temperature drops quickly at the early seconds of the cooling stage. Within 4 seconds, the temperature of the weld line is below 900°C. Fig.5.4 is the thermal history of the points with different distance to weld line. The axial load is 250MPa, the interface temperature is assumed to be 1260°C and kept constant for 30 seconds of simulation.

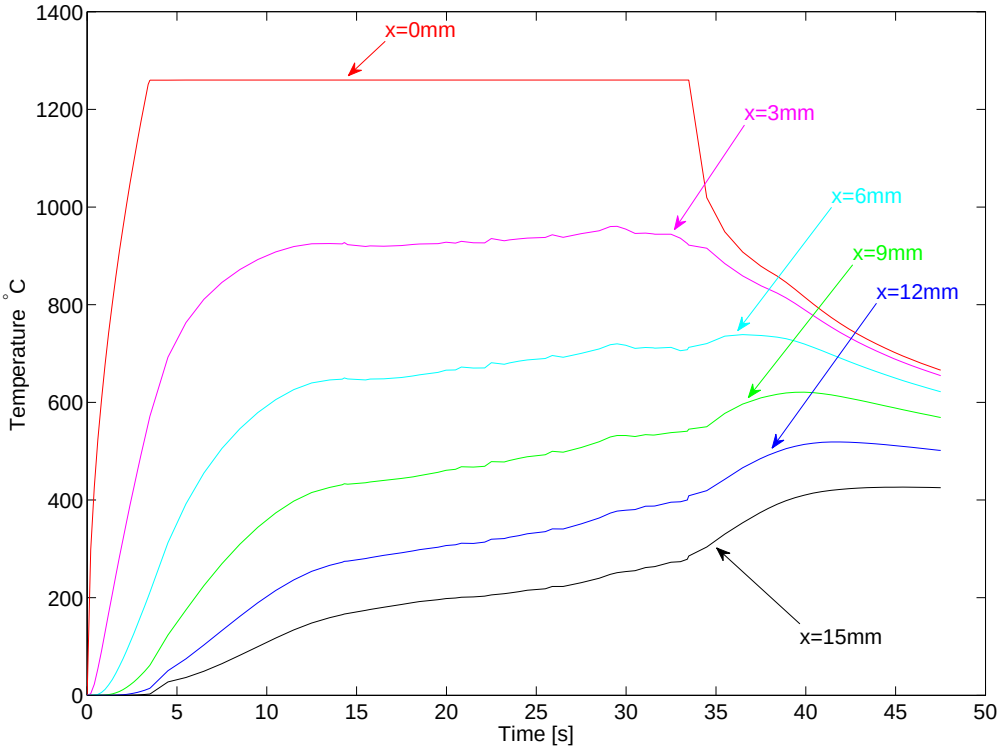

Figure 5.4: The thermal history of the points predicted by the FEM simulation.

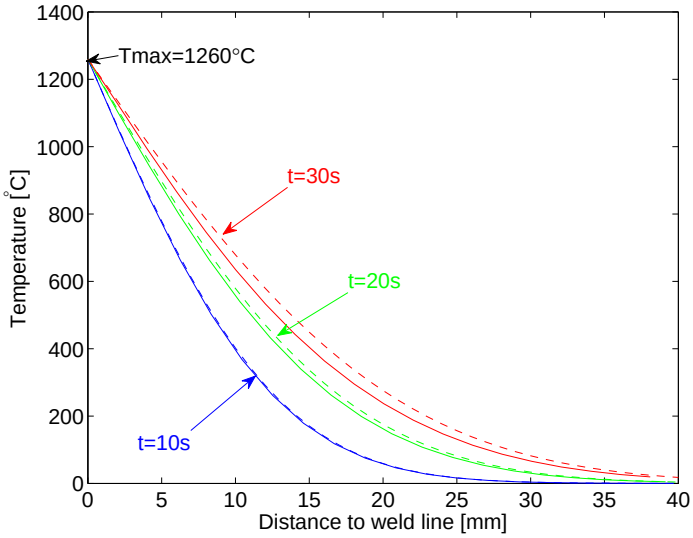

Figure 5.5: Comparison of temperature profiles from analytical model and FEM model; the dashed lines represent analytical results, the solid lines represent FEM results.

Comparison of thermal results from FEM and analytical method

The temperature profiles at different moments of the steady state stage from analytical model and FEM model are illustrated in Fig.5.5. Only half of one billet's section is shown as the rotating and static parts are all tubes with the same size, symmetrical to each other along the weld line. The temperature profiles of FEM model are quoted from the midline of the wall thickness of the tube while the corresponding axial load is assumed 150MPa. From the graph, we find the temperature fields got from both methods are quite similar at the early stages of welding. For example, in Fig.5.5, the two corresponding curves of temperature profiles are almost coincident at the time of 10s. With the welding time increasing, the difference between these two methods also increases. The temperatures predicted from analytical method are higher than those from FEM. The lack of axial shortening consideration in analytical model probably account for this error. This means that the width of the HAZ predicted by FEM model must be smaller than that by analytical method due to the plastic strain brought by the axial load. In fact, the axial shortening rate increases with the load. If the heat affected zone (HAZ) is defined as temperature above 650°C for IN718, the width of the HAZ decreases almost linearly from the 9.5mm to 7.0mm as the axial load

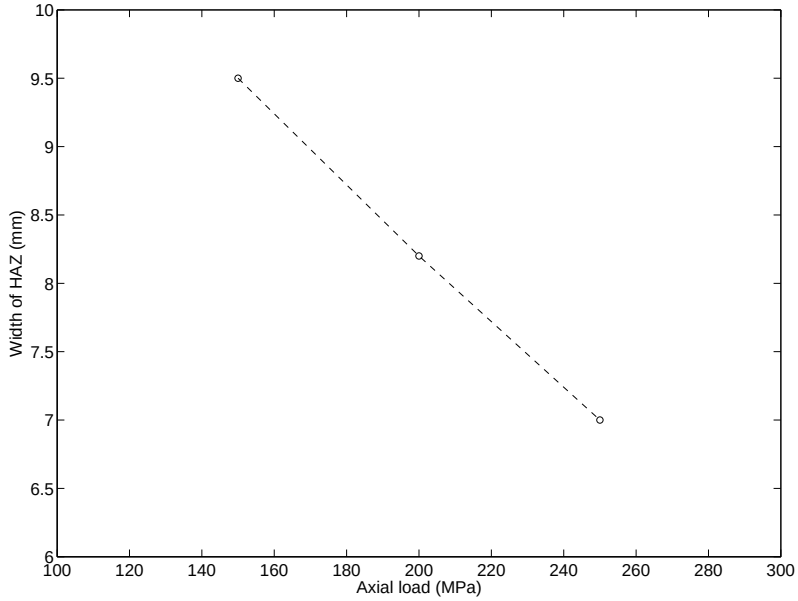

Figure 5.6: Change of the width of the HAZ with the load.

increases from the 150MPa to 250MPa, as shown in Fig.5.6.

5.2.2 Mechanical results

Predicted upsets

The results of the upset estimated from the FEM model are given in Fig.5.7 and Fig.5.8; as for the analytical solution, the impact of temperature on the upset value is considerable. Comparing the data in these two graphs, the value of the upset drops greatly when the temperature decreases from 1260°C to 1200°C. The shear stress's influence is also considerable. In both Fig.5.7 and Fig.5.8, the solid lines represent the upset curves got with the presence of the shear stress, the dashed lines correspond to those without shear stress. The values of upsets of the curves representing the combining action of compression stress and shear stress are always higher than those under the sole action of compression stress.

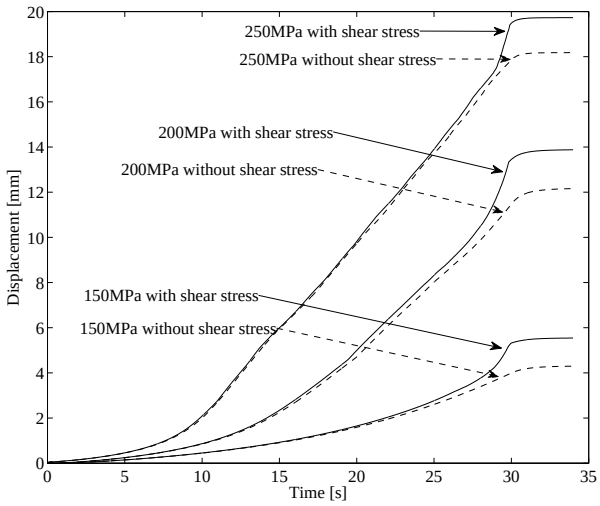

Figure 5.7: Upset profiles from FEM when assuming interface temperature 1260°C.

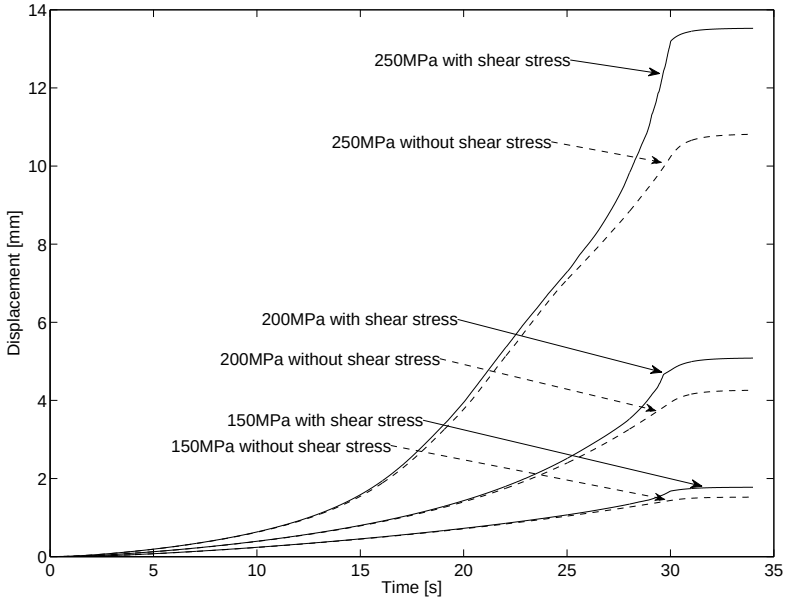

Figure 5.8: Upsets from FEM when assuming interface temperature 1200°C.

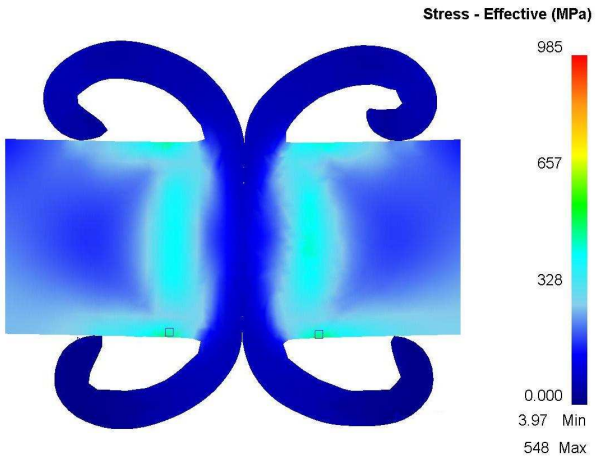

Figure 5.9: Effective stress field in inertia welding.

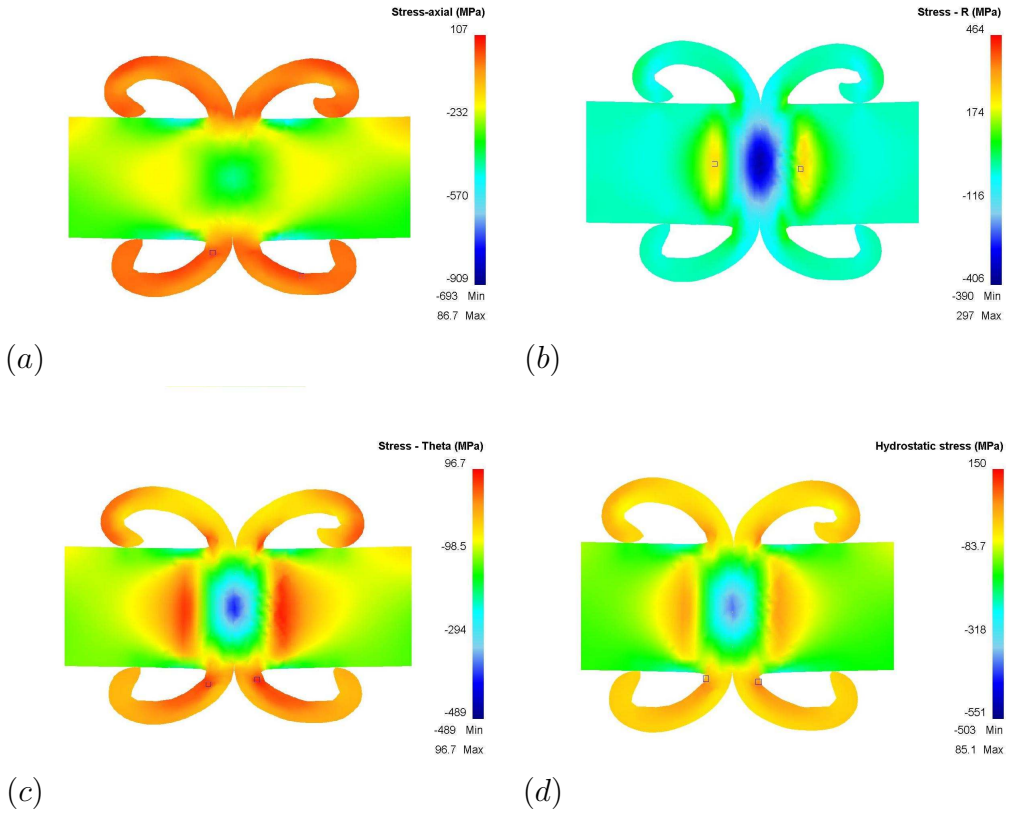

Figure 5.10: Stress distribution in inertia welding (a) normal stress in axial direction (b) normal stress in radial direction (c) normal stress in hoop direction (d) hydrostatic stress distribution.

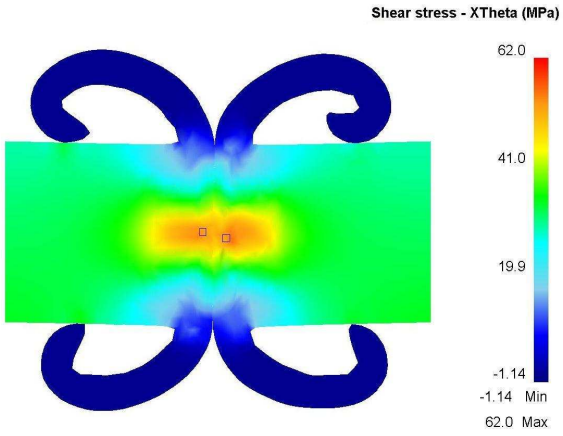

Figure 5.11: Shear stress $\sigma_{x\theta}$ distribution in inertia welding.

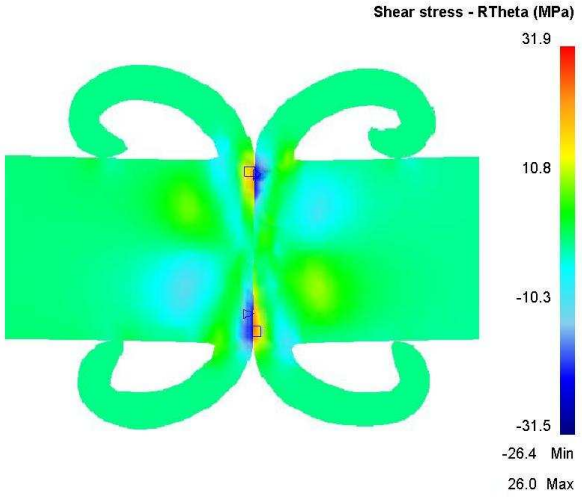

Figure 5.12: Shear stress $\sigma_{r\theta}$ distribution in inertia welding.

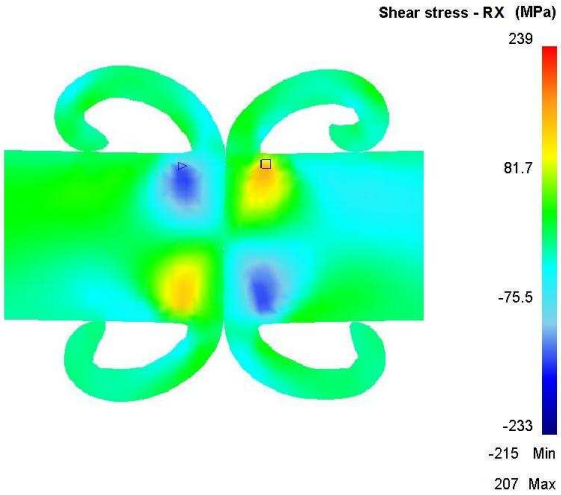

Figure 5.13: Shear stress σ_{rx} distribution in inertia welding.

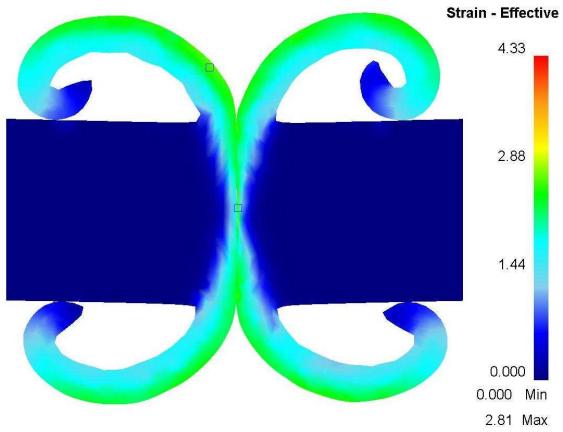

Figure 5.14: Effective strain distribution in inertia welding.

Stress, strain field

The stress fields of the inertia welding are presented from Fig.5.9 to Fig.5.13. These are got at the time of 1 second before the end of the steady state stage. From these graphs, we can find that the stress distribution is roughly mirror symmetrical along the weld line. The effective stress is shown in Fig.5.9. It is interesting to find that the effective stress near weld line is actually very small even though the axial load is kept constant during the process. One reason for this low equivalent stress must be small flow stress of the material at high temperature. Another reason can be found in the graphs of the normal stress components in axial, radial and circular directions in Fig.5.10. These three normal stress components all possess similar negative value near weld line, which means their influence on plastic deformation are to a large extent being cancelled by one another. In another word, there is a compressive hydrostatic stress located near the weld line holding the soft material there. This effect of the hydrostatic stress is consistent with the analysis in the round tube model in the former chapter. The field of this hydrostatic stress is also illustrated in Fig.5.10. The frictional shear stress $\sigma_{x\theta}$ is shown in Fig.5.11. It needs to be pointed out that the shear stress has a homogeneous distribution across nearly all the billet. This homogeneity is broken near the weld line due to the large plastic deformation. The value of shear stress components $\sigma_{r\theta}$, σ_{xr} are illustrated in Fig.5.12 and Fig.5.13 respectively. In analytical model, $\sigma_{r\theta}$ is assumed to be zero, here one can find that there is still some small value of it near the weld line. Its maximum value is only 26MPa. The existence of this $\sigma_{r\theta}$ is due to the formation of flash.

The effective strain is shown in Fig.5.14. This is the strain distribution at the end of the steady-state stage. It is clear that the strain is concentrated within a narrow band with its border no more than 2mm from the weld line. This is because only the material close to the weld line is soft enough for plastic deformation due to the steep temperature gradient near the weld interface.

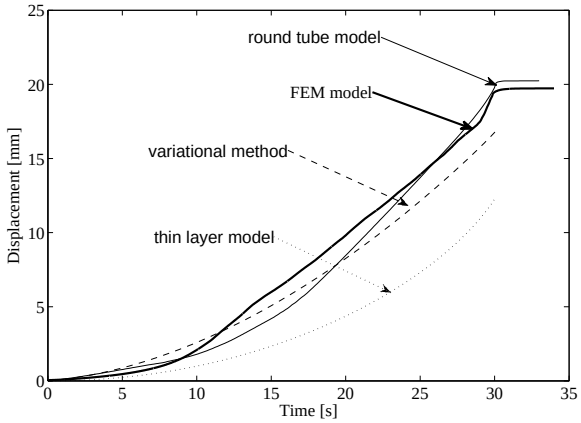

Figure 5.15: Comparison of upset value from FEM and analytical thin layer model.

5.2.3 Discussion

Comparison between FEM model and analytical models

Comparing the analytical results of upsets with those from the FEM model, see Fig.5.15, the black bold line represents value from FEM model, while the other lines refer to the results from the analytical models. One can see that the predictions are broadly consistent, which proves the analytical models used may have certain applicability. This would be more clear if the parameters used in analytical models, for instance, the thickness of the thin layer h in thin layer model, the C_2 and the height of the deformation zone H in the variational method model, can be calibrated by experimental data. This remains for future researches.

Usually the FEM model is the most popular tool used to study the friction welding process. There are several virtues for the FEM model. One is that the stress state analysis of the process is usually more rigorously considered; for example, in DEFORM-2D, the six independent stress components in stress tensor can all be taken into account in inertia welding through DEFORM-2D's $2\frac{1}{2}$ element. Another one is that both the thermal and mechanical analysis are carried out at each time step in DEFORM's calculation, and the results of the thermal and mechanical analysis are updated at each time step. Thus the analysis in FEM is thermo-mechanically coupled, so that the results from mechanical cal-

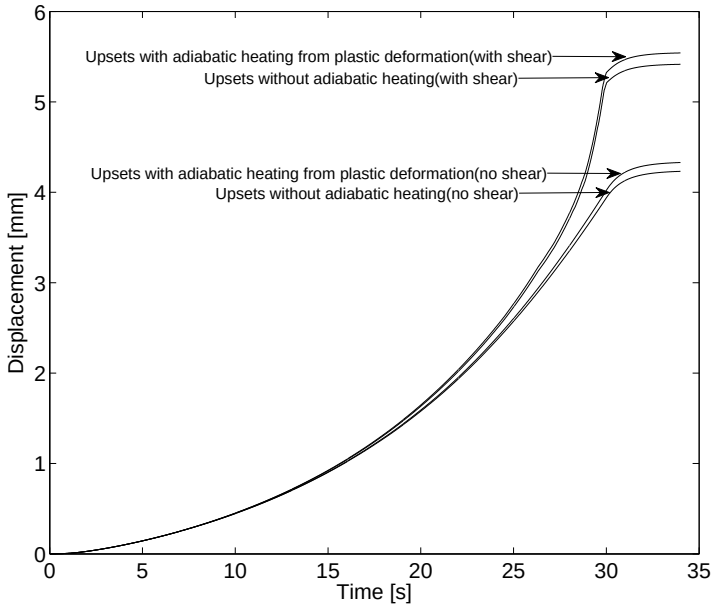

Figure 5.16: Effect of adiabatic heating from plastic deformation in FEM model.

culation can be used directly in temperature prediction. In analytical models, the thermal and mechanical analysis are done separately. The mechanical analysis is based on the temperature distributions from the thermal analysis, but the results of the mechanical analysis are not used in the thermal analysis except the axial shortening rate of the weld line. The FEM is also good at tracing the shape change of the objects, for instance, the formation of the flash can be illustrated clearly. Its influence on welding can be taken into consideration in the FEM model.

Apart from the advantages listed for the FEM model, there are also some limitations for it. The FEM model usually is much more time consuming than analytical models. In this study, it usually takes nearly twenty hours or more to run one simulation of the FEM model, while the analytical models only take several seconds or minutes to get results. So the analytical models, especially the formulae got from the thin layer model and the variational method model, can provide engineers easy and simple tools for the estimation of the axial shortening rate.

In this study, the author tried to simulate the extrusion phenomenon of inertia welding with models in DEFORM. However, it is not successful despite lots of efforts input, for ex-

ample, using much finer mesh near weld line, switch the friction condition from the sliding friction to sticking friction at the last seconds of flash forming. The possible explanation is that the theoretical foundation for the FEM code used in this study, DEFORM-2D, is the theory of plasticity in solid mechanics [84, 92]. It does a good job in simulating the plastic deformation of metal forming processes, but it may not be suitable to model the movement of the fluid-like flows. In inertia welding, the behaviour of the material in the contact zone may be more like the fluid due to high temperature in the interface. Its movement cannot be fully represented by the models in DEFORM. That may be the main reason why the phenomenon of the extrusion of the burr (internal flash) cannot be simulated and predicted in DEFORM. However, as stated before, this extrusion of the burr can be explained well by thin layer model.

Effect of adiabatic heating

A final point is that, apart from the heating from friction, the adiabatic heating from plastic deformation is not considered in the analytical model. To examine the effects of this, in Fig.5.16, two sets of upset data are compared with using the FEM model. One curve is calculated with the adiabatic heating effect on while the corresponding one off. The compression stress is 150MPa, the temperature in the interface is assumed to be 1260°C. We can see that the error from adiabatic heating is no more than 3 percent. If we define the region whose temperature is above 650°C to be the heat affected zone , the width of HAZ for the case with adiabatic heating is around 9.5mm while the width of HAZ for the one with no adiabatic heating is around 9.6mm. The error between these values is only around 2 percent. Thus, it appears that adiabatic heating from plastic deformation has little influence on the calculation process. Thus, this part of the energy is very small compared with the friction heating in the welding interface. Some researchers may hold that the heat generation is mainly due to the mechanical dissipation throughout the plasticised layer, not the sliding friction at the interface [55, 56]. Since the plasticised layer is very thin, most of heat is generated through shear stress working in circular direction, this mechanical dissipation

can still be broadly taken as a kind of friction.

5.3 Summary

In this chapter, an FEM model was developed to study inertia welding of IN718. The simulation by the FEM model shows that the axial shortening leads to the shortening of the heat affected zone. The stress analysis shows that there is a band near the welding interface with high compressive hydrostatic stress. The holding effect of this high hydrostatic stress band is the reason for the presence of the soft material near the weld line. The upset curves are also calculated under various process parameters. These indicate that the upset rises with an increase of the load and interface temperature. The presence of the frictional shear stress also leads to an increase of the upset. These results are consistent with the conclusions from the analytical models. Comparison of the FEM model and the analytical models shows that the FEM model cannot replace the role of the analytical models, which can be good compensation to FEM models. The extrusion of the burr cannot be modelled by the present FEM model, but it is explained well by the thin layer model. The study of the adiabatic heating from the plastic deformation shows that its effect is small compared with the friction heating; the neglect of it in analytical models does not lead to big errors.

Chapter 6

Conclusions and future work

Conclusions

In this study, the process of inertia friction welding was modelled by both a FEM model and analytical models. As the procedure of the inertia welding can be divided into three stages - the heating stage, the steady state stage and the cooling stage - the modelling of the process is divided correspondingly into three steps, the modelling of the heating, steady state and cooling stages. The following conclusions can be drawn from the research presented in this thesis:

- The temperature distributions of the inertia welding got from the analytical model and FEM model are in good agreement with each other. Both indicate that there is a steep temperature gradient near the welding interfaces in the axial direction. The thermal analysis of the FEM model can take the shape change of the object induced by plastic strain into consideration; it shows that the axial shortening of the friction welding leads to the decrease of the width of the heat affected zone.
- The width of the heat-affected zone is sensitive to the time spent at the flash forming stage, *i.e.* the steady state stage. The higher the holding time, the wider the HAZ. So the holding time will influence the joint quality markedly.
- The study of the heat flux indicates that the effective heat flux must decrease with

increasing welding time to maintain a constant temperature at the mating surface.

- Three sets of models were developed using three different methods in mechanical analysis. Among them, the round tube model was built with the adoption of the idea of the finite difference method. The thin layer model was built through the application of the Navier-Stokes equations to the friction welding of circular tubes. The variational model was built through applying the variational method on the principle of minimum work rate. When coupled with temperature fields, the round tube model and the variational model can be used to predict the upset value of the inertia welding with the adoption of a lambda model to describe the constitutive relationship of the IN718 superalloy at high temperature. The thin layer model can also be used to estimate the upset if the deceleration curve of the inertia welding process is available.

- Given the proper parameters for the lambda model of the IN718 superalloy, the analytical models can give reasonable prediction of the upsets in inertia friction welding in much shorter time compared with the FEM model.

- In inertia friction welding, there is a band near the welding interface with high compressive hydrostatic stress due to the steep temperature gradient there. The holding effect of this high hydrostatic stress band is the reason for the presence of the soft material near the weld line. In the case of inertia welding IN718, this soft material in the contact zone is most likely in a semi-solid slurry-like state, whose existence is the reason for the low friction coefficient observed.

- The presence of the shear stress is found to enlarge the upset value of the process; its rapid increase during the last seconds of welding can influence the upset markedly, and this needs to be accounted for if the predictions are to be accurate.

- The upset value of inertia welding is found to be sensitive to the welding interface temperature. A little rise in the interface temperature leads to a large increase in the axial shortening.

- The phenomenon of the extrusion of the burr cannot be modelled by the present

FEM model satisfactorily, but it is explained well by the thin layer model. The rapid increase of the radial flow speed is the result of the quick stop of the rotating speed due to the balance of momentum for the material in the contact zone. The thin layer model also gives us more information about the size effect in inertia welding. It predicts that the phenomenon of the burr is more likely to happen if the radius of the welding part is large.

- The effect of adiabatic heating from plastic deformation is small compared with heating effect from the friction at the mating surfaces; therefore it can be neglected in the analytical models.

- Compared with the conventional FEM model, the analytical models provide easy and quick tools for the analysis of the process. Among them, the thin layer model also adds to our understanding about the behaviour of the contact zone. So these analytical models complement the FEM models.

Future work

One feasible job is to calibrate the parameters in the analytical models put forward in this thesis with the experimental data. This work is not done in the present study due to the lack of time and inconvenience in experimental conditions.

Another possible improvement for FEM model is to try to simulate the extrusion of burr with an improved algorithm. It may be done like this: set the contact zone apart and treat this area with fluid dynamics method. The rest of the part is still treated with conventional plastic mechanics method. In this way, the FEM model may hopefully simulate the extrusion of the burr and give us a more real representation of the welding process.

Another opportunity for improvement is to couple the present models with a microstructure module, which may give us a better understanding of the physical phenomena during the welding process.

Bibliography

[1] R.C.Reed. *The Superalloys: Fundamentals and Applications*. Cambridge University Press, 2006.

[2] G.Smith and L. Sheomaker. Advanced nickel alloys for coal-fired boiler tubing. *Advanced Materials and Processes*, 162:23–26, 2004.

[3] R.E. Schafrik and Scott Walston. Challenges for high temperature materials in the new millennium. In R.C.Reed et al, editor, *Superalloys 2008, TMS, Pennsylvania, USA*, pages 3–9, 2008.

[4] C.T.Sims and W.Hagel, editors. *The Superalloys*. Wiley, New York, 1972.

[5] C.T.Sims, N.S.Stoloff, and W.C.Hagel, editors. *Superalloys II*. John Wiley and Sons Inc., 1987.

[6] C.A.Dandre, C.A.Walsh, R.W.Evans, R.C.Reed, and S.M.Roberts. Microstructural evolution of nickel-base superalloy forgings during ingot-to-billet conversion: process modelling and validation. In T.M.Pollock et al, editor, *Superalloys 2000, TMS, USA*, pages 85–94, 2000.

[7] R.Schafrik and R.Sprague. The saga of gas turbine materials. *Advanced Materials and Processes*, 162:3:33–36, 4:27–30, 5:29–33, 6:41–46, 2004.

[8] Herbert L. Eiselstein. Age-hardenable nickel alloy. U.S. patent 3046108, 1962.

[9] Chester.T.Sims. A history of superalloy metallurgy for superalloy metallurgists. In *Superalloy 1984, USA*, pages 399–419, 1984.

[10] T.Murakumo, T. Kobayashi, Y. Koizumi, and H. Harada. Creep behavior of ni-base single-crystal superalloys with various γ' volume fractions. *Acta Materialia*, 52:3737–3744, 2004.

[11] Matthew J. Donachie and Stephen J. Donachie. *Superalloys: A technical guide*. ASM International, 2002.

[12] D.A.Grose and G.S. Ansell. The influence of coherency strain on the elevated temperature tensile behavior of Ni-15Cr-Al-Ti-Mo alloys. *Metallurgical Transactions A*, 12A:1631–1645, 1981.

[13] O. Noguchi, Y. Oya, and T. Suzuki. The effect of nonstoichiometry on the positive temperature dependence of strength of Ni_3Al and Ni_3Ga. *Metallurgical Transactions A*, 12A:1647 –1653, 1981.

[14] R.P. Guest. *The Dynamic and meta-dynamic recrystallization of the Ni-base superalloy Inconel 718*. PhD thesis, University of Cambridge, 2005.

[15] M. Durand-Charre. *The microstructure of superalloys*. CRC Press, 1997.

[16] Matthew J. Donachie, editor. *Superalloys Source Book*. ASM, 1984.

[17] W. Betteridge and J. Heslop, editors. *The nimonic alloys, and other nickel-base high-temperature alloys*. Edward Arnold., 1974.

[18] R.L. O'Brien, editor. *Welding Handbook, Welding Processes*. American Welding Society, 1991.

[19] Helmut Schultz. *Electron Beam Welding*. Abington Publishing, 1993.

[20] M. Maalekian, E. Kozeschnik, H.P. Brantner, and H. Cerjak. Comparative analysis of heat generation in friction welding of steel bars. *Acta Materialia*, 56(12):2843 –2855, 2008.

[21] Bs en iso 15620:2000. British standard, 2000.

[22] K. K. Wang. Friction welding. *Weld Research Council Bulletin No.204*, pages 1–22, 1975.

[23] J.H.Bevington. Modes of welding the ends of wire, rods, &c. US Patent 463134, 1891.

[24] Welding metals. *Journal of the Franklin Institute*, pages 321 – 328, 1891.

[25] B. Halle. Welding apparatus. U.S. patent 1775311, 1930.

[26] F.H.Mueller. Plastic welding. U.S. patent 2933428, 1960.

[27] A.L.Jendrisak & A. A. Jendrisak. Method and apparatus for joining together hollow plastic ball halves. U.S. patent 2956611, 1960.

[28] V.I. Vill. *Friction Welding of Metals*. American Welding Society, 1962.

[29] M.B.Hollander & M.F. Camps-campins. Friction welding. U.S. patent 3121948, 1964.

[30] T.L.Oberle et al. Method of bonding metal workpiece. U.S. Patent 3273233, 1966.

[31] E.E. Welch. Friction welding process. U.S. patent 3777360, 1973.

[32] T.F.Berry et al. Friction welded metallic turbomachinery blade element. U.S. patent 3982854, 1976.

[33] K. Hashimoto, K.Ushitani, and Y. Serino. Poppet valve. U.S. patent 4073474, 1978.

[34] D.J.Foster and T.P. Roberts. Friction welding. U.S. patent 7021519, 2006.

[35] M. Maalekian. Friction welding - critical assessment of literature. *Science and Technology of Welding and Joining*, 12:738 –759, 2007.

[36] O.T. Midling and O. Grong. A process model for friction welding of Al-Mg-Si alloys and Al-SiC metal matrix composites. i. HAZ temperature and strain rate distribution. *Acta Metallurgica et Materialia*, 42(5):1595 – 1609, 1994.

[37] http://en.wikipedia.org/wiki/friction.

[38] K. K. Wang. and P. Nagappan. Transient temperature distribution in inertia welding of steels. *Welding Research*, 49:419s–426s, 1970.

[39] V.Balasubramanian, Y.Li, T. Stotler, J. Crompton, A.Soboyejo, N. Katsube, and W. Soboyejo. A new friction law for the modelling of continuous drive friction welding: Applications to 1045 steel welds. *Materials and manufacturing processes*, 14:845–860, 1999.

[40] A. Moal and E. Massoni. Finite element simulation of the inertia welding of two similar parts. *Engineering Computations (Swansea, Wales)*, 12(6):497 – 512, 1995.

[41] Laurent D'Alvise, Elisabeth Massoni, and Steinar J. Walloe. Finite element modelling of the inertia friction welding process between dissimilar materials. *Journal of Materials Processing Technology*, 125-126:387 – 391, 2002.

[42] Laurent D'Alvise. *Development of a finite element model for the simulation of the inertia friction welding process between dissimilar materials*. PhD thesis, L' Ecole Nationale Superieure Des Mines De Paris, 2002.

[43] T.Rich and R.Roberts. Thermal analysis for basic friction welding. *Metal Construction and British Welding Journal*, pages 93–98, 1971.

[44] F. D. Duffin and A.S.Bahrani. Frictional behavior of mild steel in friction welding. *Wear*, 26:53–74, 1973.

[45] O.T.Midling and O.Grong. A process model for friction welding of Al-Mg-Si alloys and Al-SiC metal matrix composites. ii. HAZ microstructure and strength evolution. *Acta Metallurgica et Materialia*, 42:1611–1622, 1994.

[46] Sujith Sathian. Metallurgical and mechanical properties of Ni-based superalloy friction welds. Master's thesis, University of Toronto, 1999.

[47] M. Preuss, J.W.L. Pang, P.J. Withers, and G.J. Baxter. Inertia welding nickel-based superalloy. i. metallurgical characterization. *Metallurgical and Materials Transactions A*, 33A:3215 – 25, 2002.

[48] Z.W. Huang, H.Y. Li, M.Preuss, M. Karadge, P. Bowen, S. Bray, and G. Baxter. Inertia friction welding dissimilar nickel-based superalloys alloy 720Li to IN718. *Metallurgical and Materials Transactions A*, 38A:1608–1620, 2007.

[49] M.Soucail, A. Moal, L.Naze, E. Massoni, C.Levaillant, and Y. Bienvenu. Microstructural study and numerical simulation of inertia friction welding of astroloy. In *Superalloy 1992, TMS, Warrendale, PA*, 1992.

[50] Friedrich H. Daus. *Process, microstructure and property relationships in dissimilar nickel base superalloy inertia friction welds*. PhD thesis, University of Birmingham, 2010.

[51] L. Fu, L.Y. Duan, and S.G. Du. Numerical simulation of inertia friction welding process by finite element method. *Welding Journal (Miami, Fla)*, 82(3):65–70, 2003.

[52] V.R. Dave, M.J. Cola, and G.N.A. Hussen. Heat generation in the inertia welding of dissimilar tubes. *Welding Journal (Miami, Fla)*, 80(10):246s–252s, 2001.

[53] N.N. Rykalin, A.I. Pugin, and V.A. Vasil'Eva. Heating and cooling of rods butt welded by friction process. *Welding Production*, pages 42 – 52, Oct, 1959.

[54] T.Rich and R.Roberts. The forge phase of friction welding. *Welding Research Supplement*, pages s137–s145, 1971.

[55] J.J.Healy, D.J.Mcmullan, and A.S.Bahrani. Analysis of frictional phenomena in friction welding of mild steel. *Wear*, 37:265–278, 1976.

[56] A.Francis and R.E.Craine. On a model for frictioning stage in friction welding of thin tubes. *International Journal of Heat Mass Transfer*, 28:1747–1755, 1985.

[57] J.M.Hill and J.N.Dewynne. *Heat Conduction*. Blackwell Scientific Publications, 1987.

[58] C.J.Cheng. Transient temperature distribution during friction welding of two similar materials in tubular form. *Welding Reasearch Supplement*, pages 542–550, 1962.

[59] Ahmet Z. Sahin, Bekir S. Yibas, M.Ahmed, and J.Nickel. Analysis of the friction welding process in relation to the welding of copper and steel bars. *Journal of Materials Processing Technology*, 82:127–136, 1998.

[60] Andrzej Sluzalec. Thermal effects in friction welding. *International Journal of mechanical science*, 32:467–478, 1990.

[61] Adolf Sluzalec and Andrzej Sluzalec. Solutions of thermal problems in friction welding – comparative study. *International Journal of Heat Mass Transfer*, 36:1583–1587, 1993.

[62] V.Balasubramanian, Y.Li, T. Stotler, J. Crompton, N. Katsube, and W. Soboyejo. An energy balance method for the numerical simulation of inertia welding. *Materials and manufacturing processes*, 14:755–773, 1999.

[63] K.Lee, A.Samant, W.T.Wu, and S.Srivatsa. Finite element modelling of the inertia welding process. In *NUMIFORM, Toyohashi, Japan*, 2001.

[64] L.Wang, M.Preuss, P.J.Withers, G.Baxter, and P.Wilson. Energy-input-based finite-element process modeling of inertia welding. *Metallurgical and Materials Transactions B*, 36:513–523, 2005.

[65] Q.Z. Zhang, L.W. Zhang, W.W. Liu, X.G. Zhang, W.H. Zhu, and S. Qu. 3D rigid viscoplastic FE modelling of continuous drive friction welding process. *Science and Technology of Welding and Joining*, 11(6):737 – 743, 2006.

[66] C.J. Bennett, T.H. Hyde, and E.J. Williams. Modelling and simulation of the inertia friction welding of shafts. *Proceedings of the Institution of Mechanical Engineers, Part L: Journal of Materials: Design and Applications*, 221(4):275 – 284, 2007.

[67] G.J.Bendzsak, T.H.North, and Z. Li. Numerical model for steady-state flow in friction welding. *Acta Materialia*, 45:1735–1745, 1997.

[68] V.K.Stokes and A.J. Poslinski. Effects of variable viscosity on the steady melting of thermoplastics during spin welding. *Polymer engineering and science*, 35:441–459, 1995.

[69] H.S.Carslaw and J.C.Jaeger. *Conduction of heat in solids*. Oxford, 1959.

[70] Kenneth C. Mills. *Recommended values of thermophysical properties for selected commercial alloys*. Woodhead Publishing Limited, 2002.

[71] T.Antonsson and H.Fredriksson. The effect of cooling rate on the solidification of Inconel 718. *Metallurgical and Materials Transactions B*, 36:85–96, 2005.

[72] M.S.Lewandowski and R.A. Overfelt. High temperature deformation behavior of solid and semi-solid alloy 718. *Acta Materialia*, 47:4695–4710, 1999.

[73] Peter J. Blau, Scott. D. Henry, Grace M. Davidson, Theodore B. Zorc, and Dawn R. Levicki, editors. *ASM Handbook, Friction, Lubrication and Wear Technology*, volume 18. ASM International, 1992.

[74] L. W. Zhang, J. B. Pei, Q.Z . Zhang, C.D . Liu, W.H.Zhu, Qu S, and J.H. Wang. The coupled FEM analysis of the transient temperature field during inertia friction welding of GH4169 alloy. *Acta Metallurgical Sinica (English letters)*, 20:301–306, 2007.

[75] Mingwei Wang, Liwen Zhang, and Chenhui Li Lisheng Zhang Zunli Zhang Guodong Jiang, and Fanyun Zhang. Numerical simulation of vacuum heat treatment thermal hysteresis time of GH4169 superalloy workpiece. *Transactions of Materials and Heat Treatment –Proceedings of the 14th IFHTSE congress*, 25:772–775, 2004.

[76] J.M. Zhang, Z.Y. Gao, J.Y. Zhuang, and Z.Y. Zhong. Mathematical modeling of the hot-deformation behavior of superalloy IN718. *Metallurgical and Materials Transactions A: Physical Metallurgy and Materials Science*, 30(10):2701 – 2712, 1999.

[77] C.A. Dandre, S.M. Roberts, R.W. Evans, and R.C. Reed. Microstructural evolution of Inconel 718 during ingot breakdown: process modelling and validation. *Materials Science and Technology*, 16(1):14 – 25, 2000.

[78] X. Zhao, R.P. Guest, S. Tin, D. Cole, J.W. Brooks, and M. Peers. Modelling hot deformation of Inconel 718 using state variables. *Materials Science and Technology*, 20(11):1414 – 1420, 2004.

[79] S.C. Medeiros, Y.V.R.K. Prasad, W.G. Frazier, and R. Srinivasan. Microstructural modeling of metadynamic recrystallization in hot working of IN718 superalloy. *Materials Science and Engineering A*, A293(1-2):198 – 207, 2000.

[80] S.V.S. Narayana Murty, B. Nageswara Rao, and B.P. Kashyap. Instability criteria for hot deformation of materials. *International Materials Reviews*, 45(1):15 – 26, 2000.

[81] P.L. Blackwell, J.W. Brooks, and P.S. Bate. Development of microstructure in isothermally forged nimonic alloy AP1. *Materials Science and Technology*, 14:1181 –1188, 1998.

[82] J. Lin and T.A. Dean. Modelling of microstructure evolution in hot forming using unified constitutive equations. *Journal of Materials Processing Technology*, 167(2-3):354 – 62, 2005.

[83] J.W.Brooks. Private communication, 2007.

[84] Shiro Kobayashi, Soo-IK Oh, and Taylan Altan. *Metal forming and the finite-element method*. Oxford University Press, 1989.

[85] G.D.Lahoti and Shiro Kobayashi. On Hill's general method of analysis for metal-working process. *International Journal of Mechanical Science*, 16:521–540, 1974.

[86] J.Chakrabarty. *Theory of plasticity*. McGraw-Hill BOOK Company, Inc, 1987.

[87] R. Hill. *Mathematical theory of plasticity*. 1950.

[88] M. C. Flemings, R. G. Riek, and K. P. Young. Rheocasting. *Materials Science and Engineering*, 25:103–117, 1976.

[89] Oscar Pinkus and Beno Sternlicht. *Theory of Hydrodynamic Lubrication*. McGraw-Hill BOOK Company, Inc, 1961.

[90] Donald F.Young, Bruce R.Munson, and Theodore H. Okiishi. *A brief introduction to fluid mechanics*. John Wiley and Sons Inc., 2001.

[91] http://en.wikipedia.org/wiki/navier-stokes_equations.

[92] Deform-2d ver.9.1 user's manual.

Appendix - Codes and Algorithms used in the study

1.Codes used in analytical models

In this study, the analytical models were built using Matlab.

1.1 **Codes for the thermal analysis**

The codes for the thermal analysis were written using Matlab, together with its Symbolic Math toolbox. The thermal codes are direct application of equation (3.5), equation (3.7), equation (3.8).

1.1.1 Code for heating stage

function [re]=heating_stage(q,t2)

```
% calculating exact analytical solution for semi-infinite media  for
heating stage
% surface x=0 with prescribed heat flux q
% initial temperature T(x,0)=0
% for length of rod in calculation l=70mm
% t2 is the time for heating stage

k=0.017;        % heat conductivity
jj=1;
temp=zeros(size([0:1:70]));
syms x l t x1 ak Tx1 Tx2;
Tx2=int(exp(-x^2)/x^2*q,x,x1/2/sqrt(ak*t),inf);
Tx2=Tx2*x1/k/sqrt(pi);
i=t2;
j=1;
for i1=0.000001:1:70.1
 ttx2=subs(Tx2,{t,x1,ak},{i,i1,4.09});
 Tx=double(ttx2);
 temp(1,j)=Tx;
 j=j+1;
 jj=jj+1;
end
x2=[0:1:70];
figure(1);
plot(x2,temp(1,:),'r');
hold on;
xlabel('Distance to weld line, [mm]');
ylabel('Temperature, C');
end
```

1.1.2 Code for steady-state stage

```
function [re, re1]=steady_state_stage(t1)
% t1 is the time in steady stage
% calculating exact analytical solution for semi-infinite media
% surface x=0 with prescribed temperature g(t),for steady stage in inertia
```

```
% welding
% for length of rod in calculation l=40mm, q=5J/mm2/s,
% T(x,t) is the initial temperature distribution after heating stage
%  T(x,t)=594.124770657040e-012*x^9-121.495659735306e-
% 009*x^8+10.4833679622625e-006*x^7-490.963800838202e-
% 006*x^6+13.1818310646213e-003*x^5-186.479133103865e-
% 003*x^4+614.393762091907e-003*x^3+20.3615684458824*x^2-
% 292.802679578436*x+1.26005870328505e+003

j=1;
temp=zeros(size([0:1:40]));
re=zeros(size([0:0.01:40]));
syms x l t x1 ak Tx1 Tx2;
Tx1=int(((594.124770657040e-012*x^9-121.495659735306e-
009*x^8+10.4833679622625e-006*x^7-490.963800838202e-
006*x^6+13.1818310646213e-003*x^5-186.479133103865e-
003*x^4+614.393762091907e-003*x^3+20.3615684458824*x^2-
292.802679578436*x+1.260e+003)*exp(-x^2/4/ak/t)*sinh(x1*x/2/ak/t)),x,0,l);
Tx1=Tx1*exp(-x1^2/4/ak/t)/sqrt(pi*ak*t);
Tx2=int(exp(-x^2)*1260,x,x1/2/sqrt(ak*t),inf);
Tx2=Tx2*2/sqrt(pi);
for i=0:1:40
 ttx1=subs(Tx1,{t,l,x1,ak},{t1,40,i,4.09});
 ttx2=subs(Tx2,{t,x1,ak},{t1,i,4.09});
 Tx=ttx1+ttx2;
 temp(1,j)=Tx;
 j=j+1;
end
x2=[0:1:40];
figure(3);
plot(x2,temp,'g');
xlabel('length,mm');
ylabel('temperature,C');
hold on;
re1=temp;
end
```

1.1.3 Code for cooling stage

```
function [re]=cooling_stage(t1)
% t1 represents the time during cooling stage
% calculating exact analytical solution for semi-infinite media
% surface x=0 with prescribed heat flux h(t)=0, this is for cooling stage
% of Inertia Friction Welding
% T(x) is the initial temperature distribution for different cases
% for q=5J/mm2/s, after 25s, T(x)=3.01403231095262e-012*x^9-
% 484.781151325320e-012*x^8+23.0857692744672e-009*x^7+209.020654718090e-
% 009*x^6-41.7863260077275e-006*x^5+119.399970470350e-
% 006*x^4+49.3156110448687e-003*x^3+3.24784693156375e-003*x^2-
% 67.2554791524509*x+1.26000072956388e+003

% for q=5J/mm2/s, after 10s, T(x)=-2.963414761999338e-
% 011*x^9+7.240255651838264e-009*x^8-7.209458654945050e-
% 007*x^7+3.672205145720765e-005*x^6-9.388942696699614e-
% 004*x^5+0.007362535897810*x^4+0.122797101627092*x^3+0.137206572214713*x^2
% -1.004714116395103e+002*x+1.260021858614174e+003

% for q=5J/mm2/s, after 20s, T(x)=4.544163916932399e-012*x^9-
% 6.095503891712451e-010*x^8+1.435005872692231e-008*x^7+1.573279272564743e-
% 006*x^6-9.460329754497121e-005*x^5+4.920265106820472e-
```

```
% 004*x^4+0.064664697721109*x^3+0.011677385173924*x^2-
% 74.430604522504083*x+1.260002389661285e+003

% for q=5J/mm2/s, after 30s,  T(x)=1.804200744744038e-012*x^9-
% 3.170264080026365e-010*x^8+1.799818181683347e-008*x^7-8.208257163745362e-
% 008*x^6-2.257394784011205e-005*x^5+1.918102174377527e-
% 005*x^4+0.038812340605604*x^3+7.857006541117234e-004*x^2-
% 61.827063419737343*x+1.260000211099991e+003

re=zeros(size(0:.1:70));
j=1;
temp=zeros(size([0:1:40]));
syms x l t x1 ak Tx1 Tx2;
Tx1=int(((1.804200744744038e-012*x^9-3.170264080026365e-
010*x^8+1.799818181683347e-008*x^7-8.208257163745362e-008*x^6-
2.257394784011205e-005*x^5+1.918102174377527e-
005*x^4+0.038812340605604*x^3+7.857006541117234e-004*x^2-
61.827063419737343*x+1.26000e+003)*exp(-
x^2/4/ak/t)*cosh(x1*x/2/ak/t)),x,0,l);
Tx1=Tx1*exp(-x1^2/4/ak/t)/sqrt(pi*ak*t);
for i=0:1:40
 ttx1=subs(Tx1,{t,l,x1,ak},{t1,40,i,4.09});
 Tx=ttx1;
 temp(1,j)=Tx;
 j=j+1;
end
x2=[0:1:40];
figure(1);
plot(x2,temp,'k');
xlabel('Length,(mm)');
ylabel('Temperature,(C)');
hold on;

% the following is the interpolation of the value

j1=1;
for x3=0:0.1:40

aa=ceil(x3);
 if aa==0
   re(1,j1)=temp(1,j1);
   j1=j1+1;
 else
   re(1,j1)=temp(aa)-(x3-aa+1)*(temp(aa)-temp(aa+1));
   j1=j1+1;
 end
end

end
```

1.1.4 Code for calculating effective heat flux

```
function [y3,x3]=eff_flux()
% the function is used to calculate effective heat flux q(t) at the end
% surface  x=0  when  x=0 is fixed with 1260C
% calculating exact analytical solution for semi-infinite media
% surface x=0 with prescribed temperature g(t)
% for q=10J/mm2/S, T(x,t)=-691.896522377376e-012*x^9+180.097924827808e-
% 009*x^8-19.7220441347718e-006*x^7+1.19487426005707e-003*x^6-
```

```
% 44.1137393294036e-003*x^5+1.02679325480725*x^4-
% 15.0129142665788*x^3+132.372959945488*x^2-
% 635.913555201062*x+1.26481138186087e+003

% for q=7J/mm2/S, T(x,t)= 1.56660403583949e-009*x^9-288.815154848346e-
% 009*x^8+21.8775260624245e-006*x^7-860.215968121760e-
% 006*x^6+17.5742189999777e-003*x^5-122.471812920406e-003*x^4-
% 2.06654909425446*x^3+51.9023080198878*x^2-
% 424.581344104630*x+1.26167649529352e+003

% for q=5J/mm2/S, T(x,t)=594.124770657040e-012*x^9-121.495659735306e-
% 009*x^8+10.4833679622625e-006*x^7-490.963800838202e-
% 006*x^6+13.1818310646213e-003*x^5-186.479133103865e-
% 003*x^4+614.393762091907e-003*x^3+20.3615684458824*x^2-
% 292.802679578436*x+1.26005870328505e+003

% for q=4J/mm2/S, T(x,t)=54.1212248682823e-012*x^9-16.2991082493803e-
% 009*x^8+1.93606149757148e-006*x^7-120.061255261482e-
% 006*x^6+4.16779238076744e-003*x^5-75.1040814728186e-
% 003*x^4+312.224415363552e-003*x^3+13.0023634766915*x^2-
% 234.126828827265*x+1.26022820344711e+003

% for q=3J/mm2/S, T(x,t)=-46.2689087035333e-012*x^9+7.98143046018670e-
% 009*x^8-509.828438825668e-009*x^7+11.8938089476007e-
% 006*x^6+145.374422454856e-006*x^5-11.1159532196804e-
% 003*x^4+24.3645895541190e-003*x^3+7.77508810881434*x^2-
% 176.343482993630*x+1.26000719749399e+003

temp=zeros(size([0:1:40]));
syms x l t x1 ak Tx1 Tx2 Tx  qt qt3;
Tx1=int(((-46.2689087035333e-012*x^9+7.98143046018670e-009*x^8-
509.828438825668e-009*x^7+11.8938089476007e-006*x^6+145.374422454856e-
006*x^5-11.1159532196804e-003*x^4+24.3645895541190e-
003*x^3+7.77508810881434*x^2-176.343482993630*x+1.26000e+003)*exp(-
x^2/4/ak/t)*sinh(x1*x/2/ak/t)),x,0,l);
Tx1=Tx1*exp(-x1^2/4/ak/t)/sqrt(pi*ak*t);
Tx2=int(exp(-x^2)*1260,x,x1/2/sqrt(ak*t),inf);
Tx2=Tx2*2/sqrt(pi);
Tx=Tx1+Tx2;
Tx=subs(Tx,{l,ak},{40,4.09});
Tx=diff(Tx,x1);
qt=-0.017*Tx;
qt=subs(qt,x1,0);
qt3=qt;
save heat_flux_qt  qt3  -append;
j=0.001:0.5:30;
qtt=subs(qt,t,j);
figure(1);
plot(j+9.79,qtt,'k');
xlabel('Time,[S]');
ylabel('Heat flux, J/mm2/S');
hold on;
end
```

1.2 **Codes for the mechanical analysis**

1.2.1 **Stress calculation using Lambda model**

```
   function [re1]=lamabda_model_1(Temp,rate,str)

% Temp, rate, str represent temperature, strain rate and strain
% respectively.
% constitutive equation for lambda model by J.W.Brooks for fine grain IN718
% It is commonly observed, during hot deformation, that the flow stress
% approaches a steady state condition, typically for strains in excess of
% unity, presumably corresponding to an equilibrium structure. It is also
% found that this steady state stress is approached in an exponential
% manner.

%It is assumed that the deformation mechanism can be approximated by a
% single parameter which generalises any gross structural changes, such as
% recrystallisation, recovery or second phase particle dissolution, which
% are taking place. It is further assumed that the steady state
% microstructure is a simple power function of the temperature modified
% strain rate (Zener- Hollomon parameter). Finally the structure and stress
% are both allowed to approach steady state conditions exponentially.

% k        a scaling constant
% lambda0   a scaling constant related to the steady state stress
% n        the structure-stress exponent (commonly unity so that structure
behaves like stress).
% m        the rate sensitivity of stress.
% q        the rate sensitivity of structure
% alpha    an exponential damping constant relating strain and structure.
% beta     an exponential damping constant relating strain and stress.
% qor      activation energy Q over the gas constant R.
% rate     strain rate (per second).
% Temp     temperature in C.
% Z        Zener-Hollomon parameter.
% lamb_ss  Steady state structure (defined as steady state stress/initial
stress)
% str      Total Strain
% sigma    Stress, initially zero
% sigma_i  target stress
% lambda   the microstructural parameter, initially unity.

k=5.369*1e-3;
lambda0=7.576;
n=2.877;
m=0.2522; q=-5.4354*1e-2;  alpha=2.487; beta=18.78;

Ninc=200;

qor=59407;

sigma=zeros(size(0:Ninc));
lambda=zeros(size(0:Ninc));
strain=zeros(size(0:Ninc));
eta=zeros(size(0:Ninc));
sigma(1,1)=0;
lambda(1,1)=1;
de=str/Ninc;  % Strain increment
Z=rate*exp(qor/(Temp+273.16));
```

```
% The temperature compensated strain rate, the Zener-Hollomon parameter

lamb_ss=lambda0*Z^q;

 %Then assuming that the steady state structure depends on Z by a power law

sigma_i(1,1)=k*(lambda(1,1))^n*Z^m;

% The current target stress is then a simple power function of structure

for j=2:Ninc+1
    lambda(1,j)=lamb_ss-(lamb_ss-lambda(1,j-1))*exp(-alpha*de);
    sigma_i(1,j)=k*(lambda(1,j-1))^n*Z^m;
    strain(1,j)=strain(1,j-1)+de;
    sigma(1,j)=sigma_i(1,j)-(sigma_i(1,j-1)-sigma(1,j-1))*exp(-beta*de);
    eta(1,j)=rate/sigma(1,j);
end

re1=sigma(end);

figure(10);
plot(strain,sigma,'k');
hold on;
plot(strain,sigma_i,'g');
hold on;
xlabel('Strain');
ylabel('Stress, [MPa]');
figure(9);
plot(strain,lambda,'r');
hold on;
plot(strain,eta,'k');

hold on;
end
```

1.2.2 **Lambda model coupled in Round tube model**

```
function [re]=lambda_coupled_1(Temp,strain,strate)
% constitutive equation for lambda model by J.W.Brooks for fine grain IN718
% Now the lambda model is coupled with transformed formulation into one
% formula

% k        a scaling constant
% lambda0   a scaling constant related to the steady state stress
% n        the structure-stress exponent (commonly unity so that structure
behaves like stress).
% m        the rate sensitivity of stress.
% q        the rate sensitivity of structure
% alpha    an exponential damping constant relating strain and structure.
% beta     an exponential damping constant relating strain and stress.
% qor      activation energy Q over the gas constant R.
% strate     strain rate (per second).
% Temp     temperature in C.
% Z        Zener-Hollomon parameter.
% lamb_ss  Steady state structure (defined as steady state stress/initial
stress)
% strain      Total Strain
% sigma    Stress, initially zero
% sigma_i  target stress
```

```
% lambda   the microstructural parameter, initially unity.

k=5.369*1e-3;
lambda0=7.576;
n=2.877;
m=0.2522; q=-5.4354*1e-2;  alpha=2.487; beta=18.78;
qor=59407;
Z=strate*exp(qor/(Temp+273.16));          %  Zener-Hollommon parameter

re=k*(lambda0*Z^q+(1-lambda0*Z^q)*exp(-alpha*strain))^n*Z^m-k*Z^m*exp(-
beta*strain);

end
```

1.2.3 Round tube model

The procedure for Round tube model

1) The calculation of the temperature field through the thermal analysis.

2) The calculation of deviatoric stress through equation (4.18) under the assumed velocity field.

3) The determination of shear stress through equation (4.27) using numerical integration.

4) The calculation of the flow stress through equation (4.29).

5) The determination of the effective strain rate to generate new velocity field by substitution of values for temperature, effective stress and strain into the constitutive – the lambda model.

6) The determination of the axial strain rate by equation (4.30).

7) Calculation of the strain in each sub-element and integration of it along the length of the tube.

8) Repetition of the above as necessary, until the simulation is complete.

It should be pointed out that the result of this round tube model is not stable at a temperature near melting point of the material. The reason for this is equation (4.17) is not applicable at such high temperature. How to cope with it becomes a tricky one. The result is considerably affected by the method used. This implies that it may be necessary to introduce some new physical mechanism during simulating friction welding with FDM.

```
function  [re1]=Round_tube()

sig_ef_up=0;   % the effective stress produced by the outer load
sig0=250;  %   compression stress
rn=(r0+r1)/2;  % neutral radius
dt=.1;                          % time step
dx=0.05;
len1=70;
x1=0:dx:len1;                % x coordinate
sz1=size(x1);
Y2=zeros(size(x1));    % actual flow stress of metal in welding    unit:MPa
Y1=zeros(size(x1));    % flow stress with shear stress considered  unit:MPa
acomp=0.0;
```

```
sig_sr=zeros(size(x1));  % deviator stress in radial direction  unit:MPa
sig_sz=zeros(size(x1));  % deviator stress in axial direction   unit:MPa
sig_rz=zeros(size(x1));  % deviator stress in ROZ plane         unit:MPa
dsig_rz=zeros(size(x1)); % changing rate of deviator stress in ROZ plane

sig_ef=zeros(size(x1));  % effective stress                    unit:MPa


dx1=dx*ones(size(x1));   % initial mesh length

d_dx=zeros(size(x1));    % initial mesh length change


dx1_x=zeros(size(x1));        % mesh length change

dx_d_ep=zeros(size(x1));      % initial strain at each step

dx_ep1=ones(size(x1))*.1;    % initial axial strain
ef_ep1=ones(size(x1))*.1;     % initial effective strain
eprate=ones(size(x1))*.01;    % initial effective strain rate
dx_eprate=ones(size(x1))*.01;    % initial strain rate
dr_eprate=zeros(size(x1));
dxr_eprate=zeros(size(x1));
dx_sh_eprate=zeros(size(x1));
c_eprate=zeros(size(x1));



ddx1=zeros(size(x1));          % reduced length for each mesh


ll=zeros(size(0.1:dt:33));

k4=1;

k=0.017;   % thermal conductivity
ak=4.09;   % thermal diffusivity
q=5;       % heat flux q in w/mm2
ts=30;     % time for steady state stage
th=3.5; % time for heating stage

co_z=@(r) (6*pi*r./sqrt(9/4+3/4*(rn./r).^4));
coef_z=quad(co_z,r0,rn);

co_rz=@(r) (2*pi*(r.^2-rn.^2));
coef_rz=quad(co_rz,r0,rn);

co_rtheta=@(r) (2*pi*r.*(rn./r).^4./sqrt(9/4+(3/4*(rn./r).^4)));
coef_rtheta=quad(co_rtheta,r0,rn);

co_Sz=@(r) (2*pi*r./sqrt(9/4+3/4*(rn./r).^4));
coef_Sz=quad(co_Sz,r0,r1);

for t1=0.1:dt:33                % time
k_s=0;
if t1<30.1
```

```
shear=0.000000001418488*t1^9-0.000000166597878*t1^8+0.000008141488049*t1^7-
0.000214438774337*t1^6+0.003297992664045*t1^5-
0.029949419633953*t1^4+0.154527571954597*t1^3-
0.411902557055141*t1^2+0.491240234363143*t1+7.773692560876590;
% shear stress(revised for 30 seconds)
else
    shear=0;
end
 sig_ef_up=(sig0^2+3*shear^2)^.5;   % effective stress  of external loads

if t1<30.1
 temp_x=1260*erfc((x1-x1(1,1))/sqrt(4*4.09*(1.4283+t1)));
 else
temp_x=q*sqrt(th/ts)/k*((2*sqrt(ak*(t1)/pi)*exp(-(x1-
x1(1,1)).^2/4/ak/(t1))-(x1-x1(1,1)).*erfc((x1-x1(1,1))/sqrt(4*ak*(t1))))-
(2*sqrt(ak*(t1-ts)/pi)*exp(-(x1-x1(1,1)).^2/4/ak/(t1-ts))-(x1-
x1(1,1)).*erfc((x1-x1(1,1))/sqrt(4/ak/(t1-ts)))));
end
i_6=find(temp_x<600,1,'first');      % for temperature index >600 C
for i2=1:i_6
 if (abs(t1-0.1)<0.001) && (i2==1)
   eprate(1,i2)=0.001;
 end
 if (abs(t1-0.1)<0.001) && (i2>1)
  eprate(1,i2)=eprate(1,i2-1);
 end
 if t1>30.1
     eprate(1,1:end)=0.0001;
 end

    Y1(1,i2)=lambda_coupled_1(temp_x(1,i2),ef_ep1(1,i2),eprate(1,i2));
     % flow stress of metal calculation
acomp=Y1(1,i2)^2-3*shear^2;

  if acomp<0
      acomp=1;
  elseif acomp>sig_ef_up^2;
      acomp=sig_ef_up^2;
  end

Y1(1,i2)=sqrt(acomp);

dsig_rz(1,i2)=(sig0*pi*(r1^2-r0^2)- coef_z*Y1(1,i2)-
coef_rtheta*Y1(1,i2))/(-coef_rz);
if abs(i2-1)<0.0001
  sig_rz(1,i2)=0 ;
elseif dsig_rz(1,i2)<0

    k_s=k_s+1; % to number the
      if abs(k_s-1)<0.001
        i_8=i2;
        sig_rz(1,i2)=sig_rz(1,i2-1)+ dsig_rz(1,i2)*(x1(1,i2)-x1(1,i2-1));
      end
else
  sig_rz(1,i2)=sig_rz(1,i2-1)+ dsig_rz(1,i2)*(x1(1,i2)-x1(1,i2-1));
end
kkk=Y1(1,i2)^2-3*sig_rz(1,i2)^2;
if kkk<0
   bbb=-kkk;
   lam2=@(rate)lambda_coupled(temp_x(1,i2),bbb,ef_ep1(1,i2),rate);
```

```
   b_rate=fminbnd(lam2,0,10000);
    eprate(1,i2)=eprate(1,i2)+b_rate;


   continue
else
Y2(1,i2)=sqrt(kkk);
end
sig_sr(1,i2)=1/sqrt(3)*Y2(1,i2);


sig_ef(1,i2)=2^(-.5)*(2*Y2(1,i2)^2+6*shear^2+6*sig_rz(1,i2)^2)^(.5);
       if sig_ef(1,i2)> sig_ef_up
            sig_ef(1,i2)=sig_ef_up;
        end
% call lambda model and find solution of strain rate
    lamda=@(rate)
lambda_coupled(temp_x(1,i2),sig_ef(1,i2),ef_ep1(1,i2),rate);
    aaa=fminbnd(lamda,0,10000);
if t1>30.0
    aaa=0.001;
end
    eprate(1,i2)=aaa;

dx_eprate(1,i2)=3*aaa*sig_sr(1,i2)/sig_ef(1,i2)/2;
  % strain rate in Z direction

dr_eprate(1,i2)=3*aaa*sig_sr(1,i2)/sig_ef(1,i2)/2;
  % strain rate in r direction
   dxr_eprate(1,i2)=3*aaa*sig_rz(1,i2)/sig_ef(1,i2)/2;
   dx_sh_eprate(1,i2)=3*aaa*shear/sig_ef(1,i2)/2;
c_eprate(1,i2)=sqrt(2/3)*(2*dx_eprate(1,i2)^2+2*dxr_eprate(1,i2)^2+2*dx_sh_
eprate(1,i2)^2)^(1/2);
comp_rate1=c_eprate(1,i2)-eprate(1,i2);
end
i_7=find(abs(Y1-sig_ef_up)<0.01,1,'first');

dx_eprate(1,(i_7+1):end)=0.00001;
i_9=min(i_7,i_8);

dx_d_ep(1,1:i_9)=dx_eprate(1,1:i_9)*dt;  strain in Z direction at each step

ef_ep1(1,1:i_9)=ef_ep1(1,1:i_9)+eprate(1,1:i_9)*dt;
      %accumulated effective strain
dx_ep1(1,1:i_9)=dx_ep1(1,1:i_9)+dx_d_ep(1,1:i_9);
      %accumulated axial strain
d_dx(1,1:i_9)=dx1(1,1:i_9).*exp(-1*dx_d_ep(1,1:i_9));
       % reduced mesh length
ddx1(1,1:i_9)=dx1(1,1:i_9)-d_dx(1,1:i_9);
     % length reduced at each step for every unit length
dx1(1,1:i_9)=dx1(1,1:i_9)-ddx1(1,1:i_9);
     % updated mesh length



   for ii=i_9:-1:1

    dx1_x(1,ii)=dx1_x(1,ii+1)+ddx1(1,ii);

   end
```

```
  x1=x1+dx1_x;    % calculate imagined x ordinate

  dx1_x=zeros(size(x1));
  ddx1=zeros(size(x1));
  dx_d_ep= zeros(size(x1));
 end

 t2=0.1:dt:33;
figure(2);
  plot(t2,ll*2,'b');
 xlabel('Time [s]');
 ylabel('Displacement [mm]')
 hold on;
end
```

2.Subroutines for FEM model

The subroutines for FEM are written with Fortran 90. The first subroutine is used to calculate flow stress of IN718 with Lambda model, the second one is used to update user variables in FEM code.

2.1 USRMTR.f--- Flow stress calculation

```
C**********************************************************************
    SUBROUTINE USRMTR(NPTRTN,YS,YPS,FIP,TEPS,EFEPS,TEMP)
C**********************************************************************
C    THIS SUBROUTINE CALCULATES THE FLOW STRESS OF PLASTIC MATERIAL
C    INPUT :
C     NPTRTN   =   FLOW STRESS NUMBER
C     TEPS     =   EFFECTIVE STRAIN
C     EFEPS    =   EFFECTIVE STRAIN RATE
C     TEMP     =   TEMPERATURE
C    OUTPUT :
C
C     YS       =   FLOW STRESS
```

```
C     YPS      =   DERIVATIVE OF FLOW STRESS W.R.T TEPS
C     FIP      =   DERIVATIVE OF FLOW STRESS W.R.T. EFEPS
C
C*****************************************************************

      IMPLICIT REAL*8 (A-H,O-Z), INTEGER*4 (I-N)
C
C  USER SUPPLIED SUBROUTINES
C
C
C ****    USER DEFINED VARIABLES ****
C
      CHARACTER*80 IUSRVL
      COMMON /IUSR/ IUSRVL(10)
C
C    TO READ DATA (10 RESERVED LINES)
C       READ(IUSRVL(LINE NUMBER),*) DATA1,DATA2,DATA3...
C
C    TO WRITE DATA (10 RESERVED LINES)
C       WRITE(IUSRVL(LINE NUMBER),*) NEWDATA1, NEWDATA2, NEWDATA3 ...
C
C ****     END    ****
C
C    Version 5.1
C
C    COMMON /ELMCOM/ RZE(2,4),URZE(2,4),STSE(4),EPSE(4),EFEPSE,EFSTSE,

C   +            TEPSE,RDTYE,TEMPE(4),DTMPE(4),USRE1(2),USRE2(2),
C   +            NODEE(4),KELE
```

```
C
C    Version 6.0
C
C    COMMON /ELMCOM/
C
C       RZE    : Four corner coordinates
C       URZE   : Velocity
C       STSE   : Stress
C       EPSE   : Strain rate
C       EFEPSE  : effective strain rate
C       EFSTSE  : Effective stress
C       TEPSE   : Total effective strain
C       RDTYE   : Density
C       TEMPE   : Temperature
C       DTMPE   : Temperature rate
C       DAMAGE  : Damage value
C       USRE1   : Element user state variable 1
C       USRE2   : Element user state variable 2
C       USRNE   : Nodal user state variables 1,2 at 4 nodes
C       NODEE   : Connectivity
C       KELE    : Global element number
C       KELEL   : Local element number
C       KGROUP  : Material group number
C
      COMMON /ELMCOM/ RZE(2,4),URZE(2,4),STSE(4),EPSE(4),EFEPSE,EFSTSE,
     +            TEPSE,RDTYE,TEMPE(4),DTMPE(4),DAMAGE,
     +            USRE1(1500),USRE2(1500),
     +            USRNE(1500,4),NODEE(4),KELE,KELEL,KGROUP
```

```
C
C    COMMON /NODCOM/
C
C       RZN      : Nodal point coordinates
C       URZN     : Nodal point velocities
C       DRZN     : Nodal point displacement
C       TEMPN    : Nodal point temperature
C       USRN1    : User defined state variables (Input : At the beginning of Step N)
C       USRN2    : User defined state variables (Output: At the end of Step N)
C       KNODE    : Node number
C
      COMMON /NODCOM/ RZN(2),URZN(2),DRZN(2),TEMPN,DTMPN,USRN1(1500),
     +              USRN2(1500),KNODE

C
C    CURTIM: CURRENT TIME
C
      COMMON /CLOK/ CURTIM
C
C    DTMAXC: CURRENT TIME STEP SIZE
C
      COMMON /SSTU/ DTMAXC
C
C
C    COMMON /USRCTL/
C
C       KOBJ     : Object number
C       KSTEP    : Step number (N)
C       ISTATUS  : 0 - the beginning of the step
```

```
C                1 - the end of the step
C       KSSTEP    : negative step indication -1 for negative step 1 for else
C
C     WHEN (ISTATUS.EQ. 1)  --> USRE2/USRN2 should be updated here
C     KELE  > 0           --> Element data is active
C     INODE > 0           --> Node Data is active
C
      COMMON /USRCTL/ KOBJ,ISTATUS,KSTEP,KSSTEP
C
C
C     Branching to proper flow stress routine based on the
C     number specified in the pre-processor
C
C
      GO TO (510,520,530,540,550,560,570,580,590,600),NPTRTN
C
  510 CALL UFLOW1(YS,YPS,FIP,TEPS,EFEPS,TEMP)
      RETURN
C
  520 CALL UFLOW2(YS,YPS,FIP,TEPS,EFEPS,TEMP)
      RETURN
C
  530 CALL UFLOW3(YS,YPS,FIP,TEPS,EFEPS,TEMP)
      RETURN
C
  540 CALL UFLOW4(YS,YPS,FIP,TEPS,EFEPS,TEMP)
      RETURN
C
  550 CALL UFLOW5(YS,YPS,FIP,TEPS,EFEPS,TEMP)
```

```
      RETURN
C
  560 CALL UFLOW6(YS,YPS,FIP,TEPS,EFEPS,TEMP)
      RETURN
C
  570 CALL UFLOW7(YS,YPS,FIP,TEPS,EFEPS,TEMP)
      RETURN
C
  580 CALL UFLOW8(YS,YPS,FIP,TEPS,EFEPS,TEMP)
      RETURN
C
  590 CALL UFLOW9(YS,YPS,FIP,TEPS,EFEPS,TEMP)
      RETURN
C
  600 CALL UFLOW10(YS,YPS,FIP,TEPS,EFEPS,TEMP)
      RETURN
C
C  TO BE CONTINUED BY USER
C
      END
C***********************************************************************

      SUBROUTINE UFLOW1(YS,YPS,FIP,TEPS,EFEPS,TEMP)

C***********************************************************************
C
C   Lambda model with just one formula (used together without user variable) for IN718
C
C***********************************************************************
```

```
      IMPLICIT REAL*16 (A-H,O-Z), INTEGER*4 (I-N)
C
C
C ****    USER DEFINED VARIABLES ****

      REAL*8 z,z0,lambda,strain,strain1
      CHARACTER*80 IUSRVL
      COMMON /IUSR/ IUSRVL(10)
      COMMON /SSTU/ DTMAXC
      COMMON /USRCTL/ KOBJ,ISTATUS,KSTEP,KSSTEP
      COMMON /ELMCOM/ RZE(2,4),URZE(2,4),STSE(4),EPSE(4),EFEPSE,EFSTSE,
     +            TEPSE,RDTYE,TEMPE(4),DTMPE(4),DAMAGE,
     +            USRE1(1500),USRE2(1500),
     +            USRNE(1500,4),NODEE(4),KELE,KELEL,KGROUP

C
C    SEE UFLOW1 FOR DETAILED DESCRIPTION
C
C   Incorporate lambda model formulated in one equation

      EFEPSE=EFEPSE+0.0001
      EFEPS=EFEPSE
C      USRE2(1)=USRE1(1) + DTMAXC * EFEPSE
C      strain=USRE2(1)

      fk=5.369*1e-3
      flambda0=7.576
      fn=2.877
```

```
      fm=0.2522
      q=-5.4354*1e-2
      alpha=2.487
      beta=18.78
      qor=59407.0

C     USRE1(1)=USRE1(1) + DTMAXC * EFEPSE
C     strain=USRE2(4)

C
      strain=TEPS

C     write(*,*) "USRE2(1)=",USRE2(1)
C     write(*,*) "USRE1(1)=",USRE1(1)

C     write(*,*) "strain1=",strain1

C     write(*,*) "strain=",strain

      z=EFEPS*exp(qor/(TEMP+273.16))
C       write (*,*) "z=",z
      z0=z**(1.0/15.0)
C       write (*,*)  "z0= ",z0

      lambda=flambda0*((z0**q)**15.0)

      lambda=lambda+(1-flambda0*((z0**q)**15.0))*exp(-alpha*strain)
C       write (*,*)  "lambda= ", lambda
```

```
      YS=fk*((z0**fm)**15.0)*(lambda**fn-exp(-beta*strain))

      IF (YS.GT.1000.0) YS=1000.0
      IF (YS.LT.0.0001) YS=0.0001

      YPS=fk*(z0**fm)**15.0*(fn*lambda**(fn-1.0)*alpha*(flambda0*(z0**
     &q)**15.0-1.0)*exp(-alpha*strain)+beta*exp(-beta*strain))
C     write (*,*)  " YPS=", YPS

      FIP=fk*fn*(flambda0*(z0**q)**15.0+(1.-flambda0*(z0**q)**15.0)*
     &exp(-alpha*strain))**(fn-1.0)*(z0**fm)**15.0*(flambda0*(z0**q)
     &**15.0*q-flambda0*(z0**q)**15.0*q*exp(-alpha*strain))/EFEPS

      FIP=FIP+fk*(flambda0*(z0**q)**15.0+(1-flambda0*(z0**q)**15.0)*
     &exp(-alpha*strain))**fn*(z0**fm)**15.0*fm/EFEPS-fk*(z0**fm)**
     &15.0*fm*exp(-beta*strain)/EFEPS

C     write (*,*)  " FIP=", FIP
      RETURN
      END
C*********************************************************************

      SUBROUTINE UFLOW2(YS,YPS,FIP,TEPS,EFEPS,TEMP)

C*********************************************************************

      IMPLICIT REAL*8 (A-H,O-Z), INTEGER*4 (I-N)
```

```
C
C*********************************************************************
C
C   Lambda model with just one formula (used together without user variable) for IN718
C
C*********************************************************************
C
C ****    USER DEFINED VARIABLES ****

      REAL*8 z,z0,lambda,strain,strain1
      CHARACTER*80 IUSRVL
      COMMON /IUSR/ IUSRVL(10)
      COMMON /SSTU/ DTMAXC
      COMMON /USRCTL/ KOBJ,ISTATUS,KSTEP,KSSTEP
      COMMON /ELMCOM/ RZE(2,4),URZE(2,4),STSE(4),EPSE(4),EFEPSE,EFSTSE,
     +            TEPSE,RDTYE,TEMPE(4),DTMPE(4),DAMAGE,
     +            USRE1(1500),USRE2(1500),
     +            USRNE(1500,4),NODEE(4),KELE,KELEL,KGROUP


      EFEPSE=EFEPSE+0.0001
      EFEPS=EFEPSE

      strain=USRE1(1)

      fk=5.369*1e-3
      flambda0=7.576
      fn=2.877
```

```
      fm=0.2522
      q=-5.4354*1e-2
      alpha=2.487
      beta=18.78
      qor=59407.0


C     write(*,*) "USRE2(1)=",USRE2(1)
C     write(*,*) "USRE1(1)=",USRE1(1)

C     write(*,*) "strain1=",strain1

C     write(*,*) "strain=",strain

      z=EFEPS*exp(qor/(TEMP+273.16))
C       write (*,*) "z=",z
      z0=z**(1.0/15.0)
C       write (*,*)  "z0= ",z0

      lambda=flambda0*((z0**q)**15.0)

      lambda=lambda+(1-flambda0*((z0**q)**15.0))*exp(-alpha*strain)
C       write (*,*)  "lambda= ", lambda

      YS=fk*((z0**fm)**15.0)*(lambda**fn-exp(-beta*strain))

      IF (YS.GT.1000.0) YS=1000.0
      IF (YS.LT.0.0001) YS=0.0001
```

```
      YPS=fk*(z0**fm)**15.0*(fn*lambda**(fn-1.0)*alpha*(flambda0*(z0**
     &q)**15.0-1.0)*exp(-alpha*strain)+beta*exp(-beta*strain))
C     write (*,*)  " YPS=", YPS


      FIP=fk*fn*(flambda0*(z0**q)**15.0+(1.-flambda0*(z0**q)**15.0)*
     &exp(-alpha*strain))**(fn-1.0)*(z0**fm)**15.0*(flambda0*(z0**q)
     &**15.0*q-flambda0*(z0**q)**15.0*q*exp(-alpha*strain))/EFEPS

      FIP=FIP+fk*(flambda0*(z0**q)**15.0+(1-flambda0*(z0**q)**15.0)*
     &exp(-alpha*strain))**fn*(z0**fm)**15.0*fm/EFEPS-fk*(z0**fm)**
     &15.0*fm*exp(-beta*strain)/EFEPS

C     write (*,*)  " FIP=", FIP

      RETURN
      END
C*************************************************************
```

2.2 USRUPD.f--- Updating user variables

```
C*************************************************************************

      SUBROUTINE USRUPD(NPTRTN)

C*************************************************************************
C
C     User routine to update user defined nodal and elemental
```

```
C    variables
C
C    NPTRTN is the flow stress routine number and matches the
C         number passed to the UFLOW routines. If you are not
C         using user defined flow stress routines ignore this
C         value.
C
C*****************************************************************

     IMPLICIT INTEGER*4 (I,J,K,L,M,N), REAL*8 (A-H,O-Z)

C
C    COMMON /USRCTL/
C
C      KOBJ     : Object number
C      KSTEP    : Step number (N)
C      ISTATUS  : 0 - the beginning of the step
C                 1 - the end of the step
C
C    WHEN (ISTATUS.EQ. 1)  --> USRE2/USRN2 should be updated here
C    KELE  > 0          --> Element data is active
C    INODE > 0          --> Node Data is active
C
     COMMON /USRCTL/ KOBJ,ISTATUS,KSTEP,KSSTEP

C
```

```
C     CURTIM: CURRENT TIME
C
      COMMON /CLOK/ CURTIM
C
C     DTMAXC: CURRENT TIME STEP SIZE
C
      COMMON /SSTU/ DTMAXC


C
C     COMMON /ELMCOM/
C
C        RZE     : Four corner coordinates
C        URZE    : Velocity
C        STSE    : Stress
C        EPSE    : Strain rate
C        EFEPSE  : effective strain rate
C        EFSTSE  : Effective stress
C        TEPSE   : Total effective strain
C        RDTYE   : Density
C        TEMPE   : Temperature
C        DAMAGE  : Damage value
C        DTMPE   : Temperature rate
C        USRE1   : Element user state variable 1
C        USRE2   : Element user state variable 2
C        USRNE   : Nodal user state variables 1,2 at 4 nodes
C        NODEE   : Connectivity
```

```
C       KELE    : Global element number
C       KELEL   : Local element number
C       KGROUP  : Material group number
C
      COMMON /ELMCOM/ RZE(2,4),URZE(2,4),STSE(4),EPSE(4),EFEPSE,EFSTSE,
     +            TEPSE,RDTYE,TEMPE(4),DTMPE(4),DAMAGE,
     +            USRE1(1500),USRE2(1500),
     +            USRNE(1500,4),NODEE(4),KELE,KELEL,KGROUP
C
C       STRNE     : Strain Components
C       INTNALE =0:  Edge exposed to outside world
C               1:  Internal
C       NBCDE     : Boundary Condition of four corners
C
C
      COMMON /ELMCOM2/ STRNE(4),NBCDE(2,4),INTNALE(4)
C
C       TEPS_NE  : Nodal eff. strain
C       EFEPS_NE : Nodal eff. strain rate
C       DAMG_NE  : Nodal damage factor
C       STS_NE   : Nodal stress components (elastoplastic object)
C
      COMMON /ELMCOM3/ TEPS_NE(4),EFEPS_NE(4),DAMG_NE(4),STS_NE(4,4)
C
C         Please note that the common blocks ELMCOM, ELMCOM2, ELMCOM3
C         are one set of element data for the element KELE of the object
```

```
C         KOBJ. For this element KELE, having the nodal connectivity
C      indicated in the array NODEE, nodal strain and strain rate
C         values of each node (for the element KELE) are available
C         in the array TEPS_NE and EFEPS_NE provided nodal option
C         of these variables is turned on in the Pre Processor >
C         Simulation Controls > Advanced > Output control.
C
C    COMMON /NODCOM/
C
C       RZN     : Nodal point coordinates
C       URZN    : Nodal point velocities
C       DRZN    : Nodal point displacement
C       TEMPN   : Nodal point temperature
C       USRN1   : User defined state variables (Input : At the beginning of Step N)
C       USRN2   : User defined state variables (Output: At the end of Step N)
C       KNODE   : Node number
C
     COMMON /NODCOM/ RZN(2),URZN(2),DRZN(2),TEMPN,DTMPN,USRN1(1500),
    +              USRN2(1500),KNODE
C
C       AREAN   : Nodal area
C       TMPNEB  : The corresponding temperature at contacting surface
C       SLDVEL  : Sliding velocity
C       PRESR(2) : Traction in tangential (friction) and normal (pressure)
C       INTNAL  : 0 - External surface node, 1 - Internal node
C
```

```
      COMMON /NODCOM2/ AREAN, TMPNEB, SLDVEL, PRESR(2), INTNAL
C
C       EFEPS_NN       : Nodal effective strain rate
C       TEPS_NN        : Nodal effective strain
C       DAMG_NN        : Nodal damage factor
C       STS_NN         : Nodal stress components (elastoplastic object)
C       IELMNOD(K)  = 0: Element definition
C                   > 0: Node+element definition
C
C        K = 1,2,3   -- REFERRING TO DAMAGE, EFF. STRAIN AND STRESS
C                       COMPONENTS, RESPECTIVELY
C
      COMMON /NODCOM3/ EFEPS_NN,TEPS_NN,DAMG_NN,STS_NN(4),IELMNOD(3)
C
C         Please note that the common blocks NODCOM, NODCOM2, NODCOM3
C         are one set of nodal data for the node KNODE of the object
C         KOBJ. For this node KNODE, nodal strain and strain rate
C         values of (for the node KNODE) are available
C         in the variable TEPS_NN and EFEPS_NN provided nodal option
C         of these variables is turned on in the Pre Processor >
C         Simulation Controls > Advanced > Output control.
C
      COMMON /DEFGRA/ DFDX(3,3,2)

C     Last digit if 1 is for dx/dX at x=n, and X=0
C     Last digit if 2 is for dx/dX at x=n+1, and X=0
```

```
C       Gradient computed is with respect to the original
C       configuration (X=0)
C       This True for every meshed 2D object, computed at the end of the step.


C     See USRSV1 for an example
C
      GO TO (510,520,530,540,550,560,570,580,590,600),NPTRTN
C
  510 CALL USRSV1
      RETURN
C
  520 CALL USRSV2
      RETURN
C
  530 CALL USRSV3
      RETURN
C
  540 CALL USRSV4
      RETURN
C
  550 CALL USRSV5
      RETURN
C
  560 CALL USRSV6
      RETURN
C
```

```
  570 CALL USRSV7
      RETURN
C
  580 CALL USRSV8
      RETURN
C
  590 CALL USRSV9
      RETURN
C
  600 CALL USRSV10
      RETURN
C
C  TO BE CONTINUED BY USER
C
      END
C**********************************************************************

      SUBROUTINE USRSV2

C**********************************************************************
C
C     User defined state variable calculations
C
C
C     DTMAXC : CURRENT TIME STEP
C     CURTIM: CURRENT TIME
```

```
C
C    COMMON /USRCTL/
C    KOBJ   : OBJECT NUMBER
C    ISTATUS: 0 - the begain of the step
C             1 - the end of the step
C    KSTEP  : Step Number (N)
C
C    COMMON /ELMCOM/
C    RZE    : NODAL POINT COORDINATES (four corner nodes)
C    URZE   : NODAL POINT VELOCITY    (four corner nodes)
C    STSE   : STRESS TENSOR
C    EPSE   : STRAIN RATE TENSOR
C    EFEPSE : EFFECTIVE STRAIN RATE
C    EFSTSE : EFFECTIVE STRESS
C    TEPSE  : TOTAL EFFECTIVE STRAIN
C    TEMPE  : FOUR NODAL TEMPERATURE
C    DTMPE  : TEMPERATURE CHANGE
C    DAMAGE : DAMAGE FACTOR

C    USRD2  : USER DEFINED STATE VARIABLES (OUTPUT: At the End of the STEP N)
C    NODEE  : CONNECTIVITY OF THE ELEMENT
C    KELE   : ELEMENT NUMBER
C    KELEL  : LOCAL ELEMENT NUMBER (CURRENT OBJECT)
C    KGROUP : ELEMENT MATERIAL GROUP NUMBER

C    COMMON /NODCOM/
```

```
C     RZN    : Nodal Point Coordinates
C     URZN   : Nodal Point Velocities
C     DRZN   : Nodal Point Displacement
C     TEMPN  : Nodal Point Temperature
C     USRN1  : User Defined State Variables (Input: At the beginning of Step N)
C     USRN2  : User Defined State Variables (Output: At the end of Step N)
C     KNODE  : Nonde Number
C
C     WHEN (ISTATUS.EQ. 1) --> USRE2/USRN2 should be updated here
C     KELE  > 0          --> Element data is active
C     INODE > 0           --> Node Data is active
C
C
C     Example
C
C     Examples :
C
C     USRE(1)   Strain is stored which is used in the flow stress routine
C     USRE(2)   the maximum principal stress is stored
C
C     USRN?(1) : unused in thie subroutine
C     USRN?(2) : unused in thie subroutine
C
C*****************************************************************

      IMPLICIT INTEGER*4 (I,J,K,L,M,N), REAL*8 (A-H,O-Z)
```

```
      COMMON /SSTU/ DTMAXC
      COMMON /CLOK/ CURTIM
      COMMON /USRCTL/ KOBJ,ISTATUS,KSTEP,KSSTEP
C
      COMMON /ELMCOM/ RZE(2,4),URZE(2,4),STSE(4),EPSE(4),EFEPSE,EFSTSE,
     +            TEPSE,RDTYE,TEMPE(4),DTMPE(4),DAMAGE,
     +            USRE1(1500),USRE2(1500),
     +            USRNE(1500,4),NODEE(4),KELE,KELEL,KGROUP
C
      COMMON /ELMCOM3/ TEPS_NE(4),EFEPS_NE(4)
C
      COMMON /NODCOM/ RZN(2),URZN(2),DRZN(2),TEMPN,DTMPN,USRN1(1500),
     +            USRN2(1500),KNODE
C
      COMMON /NODCOM3/ EFEPS_NN,TEPS_NN,IELMNOD2
C
      IF (ISTATUS.EQ.1.AND.KELE.GT.0) THEN
C
C     Strain = time increment * strain rate
C
        USRE2(1)=USRE1(1) + DTMAXC * EFEPSE
C
C     Calculate max principal stress and if greater than current value
C     store in the user element value
C
```

```
      USRE2(2)=USRE1(2)
      CALL USR_MAXPRN(STSE,PRNSTS)
      IF (USRE2(2).LT.PRNSTS) USRE2(2) = PRNSTS
C
C    additional variable test
C
      USRE2(3)= EFEPSE
      USRE2(4)= EFSTSE
      DO I=5, 1500
        USRE2(I)=USRE1(I)
      ENDDO

      RETURN
    ENDIF
C
    IF (ISTATUS.EQ.1.AND.KNODE.GT.0) THEN
      DO I=1, 1500
        USRN2(I)=USRN1(I)
      ENDDO
      RETURN
    ENDIF
C
    RETURN
    END
C*****************************************************************
```

```
      SUBROUTINE USRSV1

C*********************************************************************
C
C     User defined state variable calculations
C
C*********************************************************************

      IMPLICIT INTEGER*4 (I,J,K,L,M,N), REAL*8 (A-H,O-Z)
C
       REAL*8 z1,z2,lambda_1
      COMMON /USRCTL/ KOBJ,ISTATUS,KSTEP,KSSTEP
      COMMON /SSTU/ DTMAXC
C
      COMMON /ELMCOM/ RZE(2,4),URZE(2,4),STSE(4),EPSE(4),EFEPSE,EFSTSE,
     +            TEPSE,RDTYE,TEMPE(4),DTMPE(4),DAMAGE,
     +            USRE1(1500),USRE2(1500),
     +            USRNE(1500,4),NODEE(4),KELE,KELEL,KGROUP
C
      COMMON /ELMCOM3/ TEPS_NE(4),EFEPS_NE(4)
C
      COMMON /NODCOM/ RZN(2),URZN(2),DRZN(2),TEMPN,DTMPN,USRN1(1500),
     +            USRN2(1500),KNODE
C
      COMMON /NODCOM3/ EFEPS_NN,TEPS_NN,IELMNOD2
C
```

```
      qor=59407.0
      q=-5.4354*1e-2
      flambda0=7.576
      alpha=2.487


     IF (ISTATUS.EQ.1.AND.KELE.GT.0) THEN
     IF (KOBJ.EQ.1.OR.KOBJ.EQ.4) THEN
      TEMP=(TEMPE(1)+TEMPE(2)+TEMPE(3)+TEMPE(4))/4

      USRE2(1)=USRE1(1) + DTMAXC * EFEPSE

C       write(*,*) "USRE2(1)_upd",USRE2(1)
      z1=EFEPSE*exp(qor/(TEMP+273.16))
      z2=z1**(1.0/15.0)
      USRE2(2)=z2
      lambda_1=flambda0*((z2**q)**15.0)+(1-flambda0
     &*((z2**q)**15.0))*exp(-alpha*USRE2(1))
      USRE2(3)= lambda_1
C      write(*,*) "lambda_1",lambda_1
       DO I=4, 1500
         USRE2(I)=USRE1(I)
       ENDDO
       RETURN
     ENDIF
```

```
      ENDIF
C
      IF (ISTATUS.EQ.1.AND.KNODE.GT.0) THEN
        DO I=1, 1500
          USRN2(I)=USRN1(I)
        ENDDO
        RETURN
      ENDIF

      RETURN
      END
C*********************************************************************
```